

**MICRO/NANO-ENGINEERED TECHNIQUES FOR ENHANCED POOL
BOILING HEAT TRANSFER**

By

Abdolali Khalili Sadaghiani

Submitted to the Graduate School of Engineering and Natural Sciences
in partial fulfillment of the requirements for the degree of
Doctor of Philosophy

Sabanci University

June 2019

© Abdolali Khalili Sadaghiani

All rights reserved

We choose to go to the moon in this decade and do the other things, not because they are easy, but because they are hard, because that goal will serve to organize and measure the best of our energies and skills, because that challenge is one that we are willing to accept, one we are unwilling to postpone, and one which we intend to win, and the others, too.

John F. Kennedy

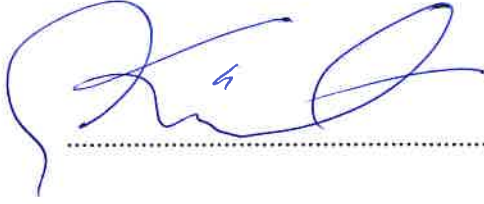
MICRO/NANO-ENGINEERED TECHNIQUES FOR ENHANCED POOL
BOILING HEAT TRANSFER

APPROVED BY:

Prof. Dr. Ali Koşar
(Thesis Supervisor)



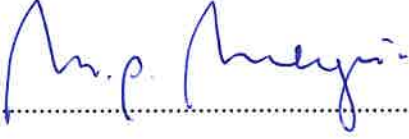
Prof. Dr. Kürşat Şendur



Assoc. Prof. Dr. Burç Mısırlıoğlu



Prof. Dr. Pınar Mengüç



Prof. Dr. Hyun Sun Park



DATE OF APPROVAL: 17/06/2019

MICRO/NANO-ENGINEERED TECHNIQUES FOR ENHANCED POOL
BOILING HEAT TRANSFER

Abdolali Khalili Sadaghiani

Mechatronics Engineering, PhD Dissertation, June 2019

Advisor: Professor Dr. Ali Koşar

Key words: Surface modification, Fundamental and application, MEMS techniques, Biocoating, Graphene, Biphilic surfaces, pHEMA coating, Surface wettability, Artificial cavities, Boiling heat transfer, Critical heat flux

ABSTRACT

Environmental aspects such as water treatment as well as military applications and thermal management emphasize on the need for next generation cooling technologies based on boiling heat transfer. Micro/nano enhanced surfaces have shown a great potential for the performance enhancement in the systems involving boiling phenomena. The lack of fully understanding the mechanisms responsible for the enhancement on these surfaces and scalability of these technologies for large and complex geometries over the wide range of materials are two main issues.

The goals of this dissertation are to provide an understanding about the fundamentals of pool boiling heat transfer (BHT) and critical heat flux (CHF) mechanisms on engineered surfaces, to develop new techniques for surface alteration for BHT and CHF enhancement, and to propose novel, facile and scalable surfaces modification techniques for related industries. Surfaces with artificial cavities, surfaces with different wettability, and surfaces with different porosities were fabricated and tested to shed light into the fundamentals of surface/boiling interaction. In addition, 3-D foam-like graphene and crenarchaeon *Sulfolobus solfataricus* P2 bio-coating surface modification techniques were proposed for BHT and CHF enhancement.

For artificial cavities it was shown that CHF occurrence on the hydrophilic surfaces is mainly due to hydrodynamic instability, while dry-out is the dominant CHF mechanism on the hydrophobic surfaces. The obtained results imply that although the increase in hole diameter enhances CHF for all the fabricated samples, the effect of pitch size depends on surface wettability such that CHF increases and decreases with pitch size on the hydrophobic and hydrophilic surfaces, respectively.

For biphilic surfaces, a novel and facile process flow for the fabrication of biphilic surfaces was proposed. It was shown that boiling heat transfer coefficient and CHF increased with $A^* = A_{\text{Hydrophobic}}/A_{\text{Total}}$ up to 38.46%. Surfaces with $A^* > 38.46\%$ demonstrated a decreasing trend in CHF and heat transfer coefficient enhancement, which is caused by earlier interaction of nucleated bubbles, thereby triggering the generation of vapor blanket at lower wall superheat temperatures. This ratio could serve as a valuable design guideline in the design and development of new generation thermal systems.

Pool boiling on pHEMA coated surfaces with thicknesses of 50, 100 and 200 nm were used to study the effect of surface porosity and inclination angle on heat transfer and bubble departure process. According to obtained results, combination of the effects of the interaction between active nucleation sites, the increase in bubble generation frequency, and the increase in bubble interactions were presented as the reasons behind the enhancement in heat transfer on coated surfaces. It was observed that under an optimum condition for the inclination angle, the porous coating provides a suitable escape path for vapor phase, which results in space to be filled by the liquid phase thereby enabling liquid replenishment.

Pool boiling experiments conducted on 3D foam-like graphene coated surfaces to show the effect of graphene coating thickness on the pool boiling heat transfer performance. According to the obtained results, 3D structure of the coating has a significant effect on pool boiling heat transfer mechanism. Factors such as pore shape and mechanical resonance of the 3D structure could be possible reasons for bubbling behavior in developed nucleate boiling. Furthermore it was found that there exists an optimum thickness of 3D graphene coatings, where the maximum heat transfer coefficient were achieved. This is mainly due to the trapped bubbles inside the porous medium, which affects the bubble dynamics involving bubble departure diameter and frequency.

A novel coating, crenarchaeon *Sulfolobus solfataricus* P2 biocoatings, were proposed for the performance enhancement of heating and cooling devices, thermofluidic systems, batteries, and micro- and nanofluidic devices. These biocoatings have the potential for addressing high heat removal requirements in many applications involving heat and fluid flows. Pool boiling experiments were performed on biocoated surfaces with thicknesses of 1 and 2 μm . The obtained results indicated that biocoated surfaces enhance boiling heat transfer by providing numerous nucleation site densities and by increasing bubble interaction on the superheated surface. Interconnected channels inside the porous coating, and capillary pumping enhance liquid transportation and reduce the liquid-vapor counter flow resistance, thereby delaying CHF condition.

There is a strong potential economic value of research performed in the framework of this thesis. Refrigeration, automotive/aerospace engineering, thermal management companies will benefit from the commercial development of the performed research.

ISITILMIŐ HAVUZ KAYNAKLI ISI TRANSFERİ İÇİN MİKRO / NANO MÜHENDİSLİ TEKNİKLERİ

Abdolali Khalili Sadaghiani

Mekatronik Mühendisliđi, Doktora Tezi, Haziran 2019

Tez DanıŐmanı; Professor Dr. Ali KoŐar

Anahtar kelimeler: Yüzey modifikasyonu, Temel ve uygulama, MEMS teknikleri, Biyo kaplama, Grafen, Biphilik yüzeyler, pHEMA kaplama, Yüzey ıslanabilirliđi, Yapay boşluklar, Kaynama ısı transferi, Kritik ısı akıŐı

ÖZET

Su arıtma, askeri uygulamalar ve termal yönetim gibi uygulamalar, kaynatma ısı transferine dayalı yeni nesil sođutma teknolojilerine duyulan ihtiyacı vurgulamaktadır. Mikro / nano yapılarla güçlendirilmiş yüzeyler, kaynama ısı transferi içeren sistemlerde performans artıŐı için büyük bir potansiyel olduđunu göstermektedir. Bu yüzeylerde kaynama ısı transferinden sorumlu mekanizmaları tam olarak anlamak ve bu teknolojilerin geniş bir malzeme yelpazesinde geniş ve karmaŐık geometriler için ölçeklenebilirliđini sađlamak araŐtırma konusudur.

Bu tezin amacı, mikro ve nano yüzeylerde havuz kaynatma ısı transferinin (BHT) ve kritik ısı akıŐı (CHF) mekanizmalarının temelleri hakkında bir anlayıŐ sađlamak, BHT ve CHF geliŐtirme için yüzey deđiŐikliđi için yeni teknikler geliŐtirmek ve yeni öneriler sunmaktır. İlgili uygulamalar için kolay ve ölçeklenebilir yüzey modifikasyon tekniklerine göre hazırlanmış yapay oyuklar, farklı ıslanabilirliđe sahip yüzeyler ve farklı gözeneklere sahip yüzeyler, yüzey / kaynama etkileŐiminin temellerine ışık tutmak için üretilmiş ve test edilmiştir. Ek olarak, BHT ve CHF artırımını için 3-D köpük benzeri grafen ve crenarchaeon Sulfolobus solfataricus P2 biyo-kaplama yüzey modifikasyon teknikleri de önerilmiştir.

Yapay oyuklar için, hidrofilik yüzeylerde CHF oluşumunun esasen hidrodinamik kararsızlıktan kaynaklandıđı, ancak kurumanın hidrofobik yüzeylerdeki baskın CHF

mekanizması olduğu gösterilmiştir. Elde edilen sonuçlar, oyuklardaki delik çapındaki artışın, üretilen tüm numuneler için CHF'yi arttırmasına rağmen, oyuk arasının büyüklüğünün etkisinin yüzey ıslanabilirliğine bağlı olduğu belirtilmiştir. Buna göre CHF sırasıyla hidrofobik ve hidrofilik yüzeylerdeki oranın artmasıyla artar ve azalır.

Bifilik yüzeyler için, bifilik yüzeylerin üretimi için yeni ve kolay bir proses akışı önerilmiştir. Kaynama ısı transfer katsayısı ve CHF'nin, $A^* = A_{\text{Hydrofobik}} / A_{\text{Total}}$ ile % 38,46'ya kadar arttığı gösterilmiştir. $A^* > \% 38.46$ olan yüzeyler, CHF ve ısı transfer katsayısı artışında düşüş eğilimi göstermiştir, Bunun sebebi de çekirdekli kabarcıkların daha erken etkileşime girmesi sonucu oluşması, böylece daha düşük duvar aşırı ısınma sıcaklıklarında buhar örtüsü oluşumunu tetiklemesidir. Bu oran, yeni nesil termal sistemlerin tasarımında ve geliştirilmesinde değerli bir tasarım rehberi olm potansiyeline sahiptir.

Yüzey porozitesi ve eğim açısının ısı transferi ve kabarcıklı ayrılma süreci üzerindeki etkisini incelemek için 50, 100 ve 200 nm kalınlıktaki pHEMA kaplı yüzeylerde havuz kaynatma çalışmaları yapılmıştır. Elde edilen sonuçlara göre, aktif çekirdeklenme bölgeleri arasındaki etkileşimin etkilerinin kombinasyonu, kabarcık oluşum sıklığındaki artış ve kabarcık etkileşimlerindeki artış, kaplanmış yüzeylerde ısı transferindeki artışın arkasındaki nedenler olarak sunulmuştur. Eğim açısı için optimum bir koşul altında, gözenekli kaplamanın buhar fazı için uygun bir kaçış yolu sağladığı ve bunun sonucunda sıvı faz tarafından doldurularak sıvı takviyesine olanak sağladığı görülmüştür.

Grafen kaplama kalınlığının havuzun kaynama ısı transfer performansı üzerine etkisini göstermek için 3D köpük benzeri grafen kaplı yüzeyler üzerinde havuz kaynatma deneyleri icra edilmiştir. Elde edilen sonuçlara göre, kaplamanın 3D yapısı, havuz kaynama ısı transfer mekanizması üzerinde önemli bir etkiye sahiptir. Gözenek şekli ve 3B yapının mekanik rezonansı gibi faktörler, gelişmiş çekirdek kaynamada kabarcıklanma davranışının olası nedenlerindedir. Ayrıca, maksimum ısı transfer katsayısının elde edildiği, optimum bir 3D grafen kaplama kalınlığı olduğu tespit edildi. Bu, esas olarak, kabarcık ayrılma çapını ve sıklığını içeren kabarcık dinamiklerini etkileyen gözenekli ortam içindeki sıkışmış kabarcıklardan kaynaklanmaktadır.

Isıtma ve soğutma cihazları, termoakışkan sistemler, bataryalar ve mikro ve nanoakışkan cihazların performansının arttırılması için yeni bir kaplama, crenarchaeon Sulfolobus solfataricus P2 bio kaplamaları önerilmiştir. Bu biyo kaplamalar, ısı ve sıvı

akışlarını içeren birçok uygulamada yüksek ısı atma gereksinimlerini ele alma potansiyeline sahiptir. Havuz kaynama deneyleri, 1 ve 2 µm kalınlığındaki kaplamalı yüzeylerde gerçekleştirilmiştir. Elde edilen sonuçlar, biyokaplamalı kaplanmış yüzeylerin, çok sayıda çekirdeklenme bölgesi yoğunluğu sağlayarak ve aşırı ısıtılmış yüzey üzerinde kabarcık etkileşimini artırarak, kaynama ısı transferini arttırdığını göstermiştir. Gözenekli kaplama içerisindeki birbirine bağlı kanallar ve kılcal pompalama, sıvı taşınımını arttırmış ve sıvı-buhar sayacı akış direncini azaltmıştır. Böylelikle kritik ısı akısı durumu gerçekleştirilmiştir.

Bu tez çerçevesinde yapılan araştırmanın derin bilimselliğinin yanında güçlü bir potansiyel ekonomik değeri vardır. Soğutma, otomotiv / havacılık mühendisliği, termal yönetim şirketleri yapılan araştırmaların ticari gelişiminden faydalanacaktır.

Acknowledgement

I would like to gratefully and sincerely thank Prof. Ali Koşar for his guidance, understanding, patience, and friendship during my graduate studies at Sabanci University. His mentorship was paramount in providing a well-rounded experience consistent my long-term career goals. He encouraged me to grow as an instructor and an independent thinker. I am not sure many graduate students are given the opportunity to develop their own individuality and self-sufficiency by being allowed to work with such independence. Additionally, I am very grateful for the friendship of all of the members of the Micro-Nano Scale Heat Transfer & Microfluidics Research Group, especially Ahmad Reza Motezakker.

I would like to thank the Faculty of Engineering and Natural Sciences, especially those members of my Ph.D. committee, namely Professor Burç Mısırlıoğlu, and Professor Kürşat Şendur, and honorable jury members Professor Hyun Sun Park from POSTECH, and Professor Pınar Mengüç from Özyeğin University for their input, valuable discussions and accessibility. I would like to specially thank Mr. İlker Mükerrerem Sevgen for all his support and above all for his friendship.

I thank my parents, Mohammad and Mahin, for their faith in me and allowing me to be as ambitious as I wanted. It was under their watchful eye that I gained so much drive and an ability to tackle challenges head on.

Table of Contents

Acknowledgement	ix
Table of Contents	x
List of Figures	xiii
List of Tables	xvii
Nomenclature	xviii
Introduction.....	21
Part 1: Motivation and background	24
1. Motivation and objectives.....	25
1.1 Motivations	25
1.1.1 Fundamentals of BHT and CHF on engineered surfaces	25
1.1.2 Developing new techniques for surface alteration.....	26
1.2 Objectives and Contributions	26
1.2.1 Proposing engineered surfaces for fundamental numerical and experimental studies	27
1.2.2 Main characteristic of engineered surfaces affecting BHT and CHF	27
1.2.3 Development of new MEMS based techniques for surface modification	27
1.2.4 Design and Engineering of High Performance Surfaces	27
2. Literature review.....	28
2.1 Boiling heat transfer (BHT)	28
2.1.1 Transient conduction model.....	29
2.1.2 Microlayer evaporation.....	29
2.1.3 Contact line heat transfer model	30
2.2 Critical heat flux (CHF)	30
2.2.1 Zuber's hydrodynamic instability	31
2.2.2 Microlayer dry-out.....	32
2.2.3 Hot/dry spots.....	32
2.3 Structured surfaces	33
2.4 Coated surfaces	35
Part 2: Fundamental studies on pool boiling	39
3. Artificial cavities.....	40
3.1 Introduction	40
3.2 Sample preparation and characterization	40

3.3	Results and discussion.....	43
3.3.1	Bubble nucleation and growth.....	44
3.3.2	Boiling heat transfer.....	46
3.3.3	Critical heat flux (CHF).....	52
3.4	Conclusions.....	57
4.	Biphilic surfaces.....	59
4.1	Introduction.....	59
4.2	Sample preparation and characterization.....	59
4.3	Results and Discussions.....	65
4.3.1	Bubble nucleation and growth.....	65
4.3.2	Boiling heat transfer.....	68
4.3.3	Critical heat flux (CHF).....	73
4.4	Conclusion.....	76
5.	Polymer coating.....	78
5.1	Introduction.....	78
5.2	Sample preparation and characterization.....	78
5.3	Results and discussion.....	82
5.3.1	Bubble nucleation and growth.....	82
5.3.2	Boiling heat transfer.....	83
5.4	Conclusion.....	93
Part 3: Application.....		95
6.	3-D Graphene coating.....	96
6.1	Introduction.....	96
6.2	Sample preparation and characterization.....	97
6.3	Discussion.....	101
6.4	Conclusion.....	112
7.	Bio-coating.....	113
7.1	Introduction.....	113
7.2	Sample preparation and characterization.....	113
7.3	Discussion.....	118
7.4	Conclusion.....	123
Part 4: Conclusion remarks and outputs.....		125
8.	Conclusion, contribution and future works.....	126
8.1	Introduction.....	126
8.2	Main objectives and findings.....	126

8.3 Recommendations for future work.....	128
Bibliography	130
APENDIX 1 – Experimental setup and procedure	147
A1.1 Experimental setup	147
A1.2 Procedure.....	150
A1.3 Validation	150
APENDIX 2 - Data reduction and uncertainty analyses.....	152
A2.1 Data reduction	152
A2.2 Uncertainty analysis	154
A2.3 Bubble departure process	156
APENDIX 3 - Publications.....	158
A3.1 Peer-reviewed articles	158
A3.2 Conference proceedings and presentations	160
A3.3 Patents	160

List of Figures

Figure 1.1 Typical pool boiling curve	22
Figure 3.1 Transient conduction model [26]	29
Figure 3.2 Schematic of the bubble base depicting the microlayer and its three regions	29
Figure 3.3 Scheme of the different nucleate boiling regimes, contact line (left) and microlayer (right), in terms of interface shape at the bubble foot (up) and wall heat flux profile (down)	30
Figure 3.4 schematic of the Zuber hydrodynamic instability model. (a) Vapor jet formation prior to CHF. (b) Unit cell containing a single jet and surrounding liquid. (c) Vapor mushroom formation due to Helmholtz instability	32
Figure 3.5 Schematic of dryout model.....	32
Figure 3.6 Schematic of hot/dry-spot model	33
Figure 4.1 Fabrication process flow of the prepared samples	41
Figure 4.2 SEM images of three test specimens: a) 50-500-phil, b) 100-2000-phil, c) 200-1000-phil.....	42
Figure 4.3 Static contact angles of substrates a) without Teflon coating, b) with Teflon coating.....	42
Figure 4.4 Bubble nucleation and growth on a) hydrophilic structured b) hydrophobic structured surfaces	44
Figure 4.5 Bubble departure frequency for a) hydrophilic samples and b) hydrophobic samples.....	46
Figure 4.6 Obtained heat transfer coefficients for hydrophobic and hydrophilic surfaces a) at different pitch sizes with hole diameter of 50 μm b) at different pitch sizes with hole diameter of 200 μm	48
Figure 4.7 Different types of bubble coalescence on structured surfaces a) horizontal b) vertical c) horizontal-vertical.....	49
Figure 4.8 Individual bubbles and vapor columns shapes on hydrophilic and hydrophobic structured surfaces – effect of hole diameter and pitch size.....	50
Figure 4.9 Bubble/vapor blanket motion on hydrophobic structured surface NO #8 (D50 – P500 – phob).....	51

Figure 4.10 CHF mechanism according to the Zuber’s hydrodynamic instability theory and the Haramura and Katto’s macrolayer dry-out model. Adapted version from Liang and Mudawar [27].....	54
Figure 4.11 a) CHF enhancement on the tested surfaces relative to the bare silicon surface b) visual results under the CHF condition and their schematic.....	56
Figure 5.1 Configuration of biphilic samples	60
Figure 5.2 Fabrication of biphilic surfaces. a) 1 μm deep anisotropic silicon etch using photoresist as etch mask. b) Thermal growth of 1 μm silicon dioxide. c) Photolithography – oxide etching mask. d) Dry etching of silicon dioxide. e) Photolithography – silicon etching mask. f) Formation of nano grass using deep reactive ion etching.....	61
Figure 5.3 SEM images related to top view of recipe (a) N-G #2 (b) N-G #3 (c) N-G #5 and lateral view of (d) N-G #2 (e) N-G #3 (f) N-G #5. The etching time for all the recipe is 3 minutes. b) and e) show the top and lateral view of N-G #3 which is used in the biphilic samples.	63
Figure 5.4 SEM images of fabricated samples with hydrophobic circular areas with a) 50 μm diameter b) 300 μm diameter c) 800 μm diameter d) 1000 μm diameter	64
Figure 5.5 Surface characterization of biphilic samples. Samples were characterized using Atomic Force Microscopy (AFM) and contact angle measurement techniques. a) 2-D b) 3-D AFM results showing the size and shape of hydrophobic structures. c) Contact angle measurement on both hydrophilic (20°) and hydrophobic (165°) areas ..	65
Figure 5.6 a) vapor/gas trapping in surface cavities according to Wang and Dhir model b) vapor/gas trapping in surface cavities according to Bankoff model c) Bubble nucleation on superhydrophobic islands.....	67
Figure 5.7 Bubble size during the nucleation and coalescence process on a) sample NO#1 (D=50 μm and S=950 μm) and b) and sample NO#8 (D=900 μm and S=100 μm)	68
Figure 5.8 Bubble merging on the sample NO#6	68
Figure 5.9 Obtained HTC’s as a function of applied wall heat flux on a) samples NO#1 to NO#6 b) samples NO#6 to NO#10 c) data of samples NO#6 to NO#10 up to $q'' < 50 \text{ W/cm}^2$ d) data of samples NO#6 to NO#10 from $q'' > 50 \text{ W/cm}^2$	71
Figure 5.10 The boiling curves for tested samples	74
Figure 5.11 a) Unit cell containing vapor jets with diameter D and surrounding liquid b) dry spots on samples with high D/S ratios.....	75

Figure 5.12 Vapor column behavior just before CHF condition (176 W/cm ²) on biphilic SAMPLE #6.....	76
Figure 6.1 Raman spectrum taken from the pHEMA films having the thickness of 200 nm a) before the boiling experiments b) after the boiling experiments.....	80
Figure 6.2 (a) Three-dimensional image and (b) depth histogram of an area of 10 μm square of the pHEMA film with the thickness of 200 nm	81
Figure 6.3 Bubbles and active nucleation sites on a) pHEMA coated surfaces with thicknesses of 100 nm for heat flux of 20 kW/m ² b) silicon surface for heat flux 20 kW/m ² c) pHEMA coated surfaces with thicknesses of 100 nm for heat flux of 30 kW/m ² d) silicon surface for heat flux 30 kW/m ²	82
Figure 6.4 Effect of heat flux on active nucleation sites on a) pHEMA coated surface at 35 kw/cm ² heat flux b) silicon surface at 35 kw/cm ² heat flux c) pHEMA coated surface at 50 kw/cm ² heat flux d) silicon surface at 50 kw/cm ² heat flux	83
Figure 6.5 Heat transfer coefficients for pHEMA coated surfaces with thicknesses of a) 50, b) 100 c) 200nm d) heat transfer enhancement.....	86
Figure 6.6. Bubble movement on pHEMA coated surfaces b) schematic of moving bubble in the growth stage	87
Figure 6.7 Bubble growth on a) bare silicon plate and b) pHEMA coated surface c-d) Bubble coalescence and interaction upon the departure on coated surfaces e) schematic of bubble departure on coated surface f) schematic of bubble coalescence on the coated surface.....	88
Figure 6.8 Effect of surface orientation on active nucleation sites on the surface with coating thickness of 100 nm	89
Figure 6.9 Bubble movement and collision on inclined surface.....	90
Figure 6.10 Schematic of heat transfer enhancement mechanism on the inclined pHEMA coated surface.....	91
Figure 6.11 Effect of inclination angle on pool boiling curve for a) 100 nm coated surface b) 200nm coated surface c) percent of heat transfer coefficient enhancement ..	93
Figure 7.1 Transferring of graphene foam on substrate.....	98
Figure 7.2 Adhesion tests between graphene foam and substrate	98
Figure 7.3 Obtained SEM images for (a) nickel foam, (b) GF/nickel foam (c) GF (sample#4) d) contact angle goniometer image (sample#3).....	100
Figure 7.4 a) XRD spectrum of 3D-graphene foam (samle#4) b) Raman spectrum of 3D-graphene foam (sample#4)	101

Figure 7.5 Bubble nucleation from surfaces with a) discrete cavity structure b) pore network. The porous medium directly affects the nucleation process by providing interconnected paths for vapor and liquid transport.	102
Figure 7.6 Obtained wall superheats (a) and calculated heat transfer coefficients (b) as a function of applied heat flux for bare silicon and graphene coated surfaces.....	105
Figure 7.7 a) Bubble nucleation on graphene coated porous surface and forces acting on a bubble upon departure from a porous surface b) bubble nucleation and growth inside the porous medium.....	107
Figure 7.8 a) experimental bubble departure diameters b) experimental bubble departure frequencies for surfaces with different coating thicknesses	108
Figure 7.9 a) Schematic of the nucleate boiling on porous structure b) bubble departure initiation upon a pore	110
Figure 7.10 Generated bubbles for different coatings and bare silicon surfaces at the heat flux of 90 kW/m ²	111
Figure 8.1 preparation and the coating process of crenarchaeon <i>S. solfataricus</i> P2....	115
Figure 8.2 (a) 2D surface profile (b) Cavity size distribution (c) 3D surface profile of a cavity of ~2 μm thick coating. (d) Water contact angle measurement (e) Fluorescence micrograph of cellular structures from crenarchaeon. DNA stained by DAPI (blue). (f) SEM images of the coated surface showing surface porosity.	117
Figure 8.3 SEM images of biocoated surfaces	118
Figure 8.4 a) departed bubble with non-spherical shape form biocoated surface at wall heat flux of 50W/cm ² b) bubble departure diameter on tested samples at low and moderate heat fluxes	120
Figure 8.5 a) Boiling curves b) obtained heat transfer coefficients on tested samples.	121
Figure 8.6 a) inclined departed bubble b) isolated bubble in nucleate boiling region.	123
Figure 8.7 a) Formed vapor columns on silicon (right) and biocoated (left) surfaces prior to dryout condition b) CHF values on tested samples	123

List of Tables

Table 4-1 Characteristics of fabricated samples	42
Table 5-1 Physical properties of fabricated samples	60
Table 5-2 Nano-grass etching parameters. 5 different etch recipes were tested. The gas flows of SF ₆ and C ₄ H ₈ were fixed at 300 sccm and 150 sccm, respectively. The SF ₆ pulse time was either 3 or 4 seconds and the C ₄ H ₈ pulse time was fixed at 2 seconds. The chuck temperature varied between 0°C and 30°C. The etch time was 3 min in all the cases	62
Table 5-3 Obtained HTC enhancement at wall superheats of 10K, 15K, and 20K for samples No#1, No#6, No#7, No#10	72
Table 7-1 Growth parameters for prepared graphene foams using the chemical vapor deposition (CVD) method.....	97
Table 7-2 Sample characterization. Specific surface area (SSA), graphene thicknesses, and water contact angles measurement of each sample.....	99

Nomenclature

A	Surface area (m^2)
a	Characteristics length (m), acceleration (m/s^2)
Bo	Bond number (-)
Ca	Capillary number (-)
C_p	Specific heat (J/K)
C_D	Drag coefficient (-)
C_{sf}	Surface factor (equation A1.1)
D	Diameter/hydraulic diameter (m)
\dot{D}	Bubble diameter growth rate (m/s)
D_d	Bubble departure diameter (m)
D_b	Base diameter (m)
f	Bubble departure frequency (Hz)
F	Force (N)
g	Gravitational acceleration (m/s^2)
h	Heat transfer coefficient ($\text{W/m}^2\cdot\text{K}$)
h_{fg}	Latent heat of vaporization (kJ/kg)
I	Current (Amper)
k	Thermal conductivity ($\text{W/m}\cdot\text{K}$)
l	Distance (m)
M	Molar concentration
N_a	Active nucleation site density ($1/\text{m}^2$)
P	Pressure (bar)
p	Pitch size (m)
Pr	Prandtl number (-)

Q	Heat (W)
q''	Heat flux (W/cm ²)
R	Gas constant (J/mol.K), thermal resistance (K/W)
R_a	Average roughness (m)
S	Edge to edge spacing between islands (m)
S_m	Spacing between roughness peaks (m)
T	Temperature (K)
u	Velocity (m/s)
V	Voltage (V)
u	Velocity (m/s)
U	Uncertainty (variable units)
x	Horizontal location (m)
X	Experimental parameter (variable unit)
y	Vertical location (m)
\dot{y}	Vertical rising velocity (m/s)
Greek	
α	Inclination angle (degree)
δ	Microlayer thickness (m)
η	Dynamic viscosity (Pa.s)
κ	Medium permeability (m ²)
λ	Wavelength (m)
λ_D	Dangerous wavelength (m)
λ_H	Taylor wavelength (m)
μ	Kinematic viscosity (m ² /s)
ν	Specific volume (m ³ /kg)
π	Pi number (3.14159)
θ	Contact angle (degree), inclination angle (degree), diffraction angle (degree)
ρ	Density (kg/m ³)
σ	Surface tension force (N/m)
ν	

Subscription

<i>ave</i>	Average
<i>C</i>	Center
<i>f</i>	Fluid
<i>g</i>	Gas
<i>l</i>	Liquid
<i>sat</i>	Saturation
<i>sup</i>	Superheat
<i>v</i>	Vapor

Abbreviations

AFM	Atomic Force Microscopy
BET	Brunauer-Emmet-Teller
BHT	Boiling heat transfer
CA	Contact angle
CHF	Critical heat flux
CVD	Chemical vapor deposition
fps	Frames per second
HTC	Heat transfer coefficient
iCVD	Initiated Chemical Vapor Deposition
MLG	Multilayer graphene
NSD	Nucleation site density
ONB	Onset of nucleate boiling
Phil	Hydrophilic
Phob	hydrophobic
PR	Photoresist
SEM	Scanning Electron Microscope
SLG	Single layer graphene
SSA	Specific surface area
WCA	Water contact angle
XRD	X-ray crystallography

Introduction

Owing to a large amount of heat dissipation and achievable high heat-transfer coefficients, boiling is one of the most effective heat transfer mechanisms for cooling [1]. As a result, many studies have been conducted to enhance boiling heat transfer and reach ultra-high heat flux cooling during recent years. With advances in nanotechnology and our understanding in multiphase flows, new techniques and materials have been developed and proposed to enhance the boiling heat transfer.

A typical boiling phenomenon (shown in Figure 1.1) starts with single-phase natural convection. As the wall heat flux increases, bubbles start to form. They grow and eventually depart from the heated surface. The process of bubble formation and departure is associated with partial nucleate boiling. The nucleation process in partial nucleate boiling strongly depends on the surface morphology. In this region, the number of active nucleation sites is highly dependent on the thermal boundary conditions (wall superheat—the temperature difference between wall and saturated temperature—, wall heat flux, surface morphology). As the rate of bubble nucleation increases with the applied heat flux, more bubbles coalesce, forming vapor columns. In this boiling region, the rate of bubble generation rapidly increases, resulting in interactions between adjacent bubbles and generation of vapor columns on the surface. In the so-called developed nucleate boiling region, heat transfer from the heated surface is enhanced up to a point, where the formation of vapor columns and blankets eventually reduces the heat transfer by acting as an isolating layer between the heated surface and the liquid. A larger lateral coalescence of vapor columns contributes to the formation of dry spots on the superheated surface. This point is called critical heat flux (CHF), which is the limit for systems involving boiling phenomena. Beyond CHF, a permanent vapor blanket appears on the heated surface, and the surface temperature dramatically increases, leading to the device burnout.

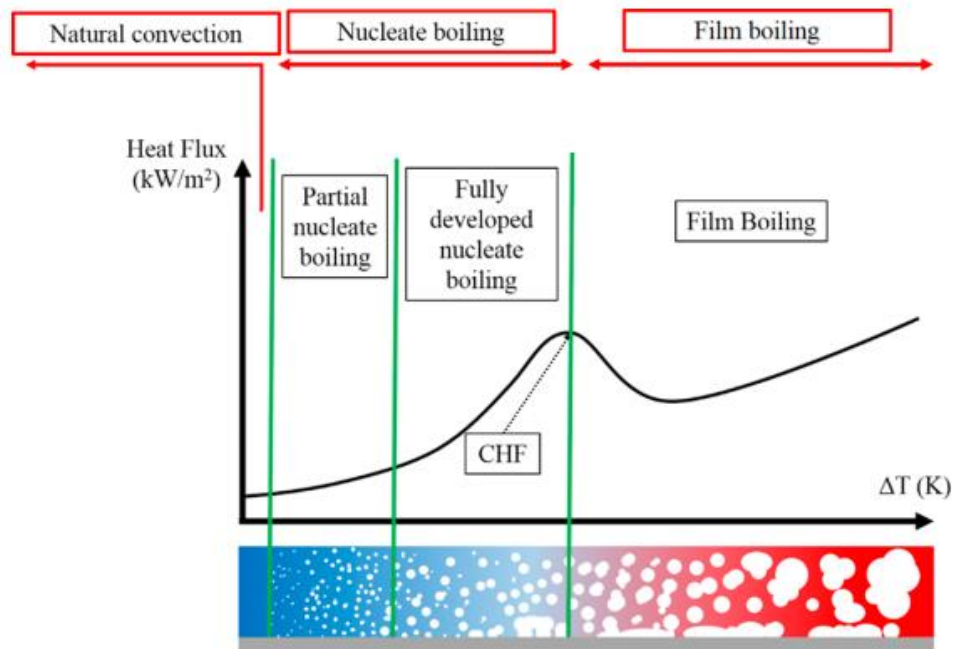


Figure 0.1 Typical pool boiling curve

An enhancement in pool boiling heat transfer and critical heat flux can be achieved by changing the surface characteristics such as wettability, wickability, roughness, nucleation site density, and providing separate liquid and vapor pathways. The goals of this dissertation are to understand the fundamentals of pool boiling heat transfer (BHT) and critical heat flux (CHF) mechanisms on engineered surfaces, to develop techniques for surface modification for BHT and CHF enhancement, and to proposed new modified surfaces for related industries.

The organization of the present thesis is as follows:

Part 1 – Motivation and background: This part consists of two chapters. Chapter 1 covers the motivations, objectives, and contributions to the field of the research. Chapter 2 summarizes a detailed literature review on pool boiling heat transfer on engineered surfaces. This chapter presents different pool boiling heat transfer enhancement approaches including micro/nanostructured surfaces, macro-machined surfaces, and mixed wettability surface boiling. In addition pool boiling models with enhanced surface designs are also presented in this Chapter.

Part 2 – Fundamental: Consisting of three chapters, in the second part of this thesis, effect of surface characteristics including nucleation site characteristics (Chapter 3), surface wettability (Chapter 4), and surface coating (Chapter 5) is investigated. Each of

these chapters is based on either published journal papers or manuscripts under preparation. Surface modification techniques are presented in sample preparation and characteristics sections of each chapter. Heat transfer enhancement mechanisms, bubble departure characteristics, and critical heat flux models are presented and discussed for three different surface conditions.

Part 3 – Application: In the second part of this thesis two kinds of novel coatings are proposed for thermal management in electronics and refrigeration industries. Each of these chapters (Chapter 6, and Chapter 7) is based on published journal articles. Surface modification techniques related to these engineered surfaces are different from the previous section, where MEMS based techniques were used.

Part 4 – Conclusion remarks and outputs: Finally this dissertation wraps up with a summary and contributions of the research works accomplished in this work, and few recommendations for further advancement in Chapter 8.

Part 1: Motivation and background

**Motivation of the present thesis and literature review of the
available state-of-the-art**

1. Motivation and objectives

1.1 Motivations

Environmental aspects such as water treatment as well as thermal management in high power energy applications make the next generation technologies for boiling heat transfer augmentation an emerging topic. Micro/nano enhanced surfaces have shown a great potential for performance enhancements in systems working with boiling phase change. Lack of fully understanding the responsible enhancement mechanisms on these surfaces as well as scalability of these technologies for large and complex geometries over the wide range of materials are vital issues in the literature. The goals of this dissertation are to understand the fundamentals of pool boiling heat transfer (BHT) and critical heat flux (CHF) mechanisms on engineered surfaces, to develop new techniques for surface alteration for BHT and CHF enhancement, and to proposed novel, facile and scalable surfaces modification techniques for related industries.

1.1.1 Fundamentals of BHT and CHF on engineered surfaces

Boiling is naturally a phase change phenomenon, which not only depends on thermo-hydrodynamics of the liquid phase but also on many complex interfacial processes. Although engineered surfaces have significantly enhanced BHT and CHF, the fundamental mechanisms of boiling on these surfaces are still not fully understood. Lack of precise hydrothermal measurements during bubble nucleation and growth as well as limited visual observations of vapor phase behavior at high heat fluxes make the understanding of major mechanisms behind BHT and CHF difficult. Although different CHF and BHT mechanisms have been proposed to extend the available mechanistic models for different conditions, these models are limited to specific liquid/surface conditions and are valid for specific operation circumstances. As a result, systematic investigations on parameters such as surface wettability, nucleation site density (NSD),

and surface porosity are required to understand the individual effect of these factors on BHT and CHF.

1.1.2 Developing new techniques for surface alteration

The applicability of the proposed engineered surfaces is still a big barrier for a real life applications. Almost all of the micro/nanostructured surfaces are in the risk of fouling and destruction. Environmental contaminations, extermination of coatings at high temperatures, surface deposition as well as surface functionality for a large range of hydrothermal conditions, and their compatibility with different working fluids are among the factors deteriorating their performance and eventually reducing their functionality.

Furthermore, bio-compatibility and environmental issues are becoming more and stricter day after day. Most of the available techniques are chemical based techniques, which are toxic, and the by-product of the fabrication techniques are dramatically harmful for the nature. It should be noted that these techniques generally require high-tech and expensive devices such as cleanroom facilities. The scalability of the proposed techniques is also a big challenge. The surface modification technique depends on the available devices for cleanroom facilities, in addition the nature of modification techniques is not compatible for the some applications (i.e. PVD for inner surfaces of a curved tube). Consequently, development of robust, cheap, functional, and eco-friendly techniques are essential for improved efficiency in high heat flux and energy applications.

1.2 Objectives and Contributions

The aims of this dissertation are to understanding the boiling heat transfer and critical heat flux mechanisms on engineered surfaces, and to develop and propose novel and new engineered surfaces for related industries. Based on these goals the objectives of the current work are as follows.

1.2.1 Proposing engineered surfaces for fundamental numerical and experimental studies

The first objective of this thesis is to propose engineered surfaces with acceptable complexity to perform parametric and mechanistic studies on pool boiling. It is aimed that the characteristics of these surfaces and obtained results could serve for further numerical analysis and development of numerical codes for more specific investigations.

1.2.2 Main characteristic of engineered surfaces affecting BHT and CHF

The second objective of this thesis is to fundamentally investigate the effect of engineered surfaces on onset of nucleate boiling (ONB), bubble dynamics, boiling heat transfer and critical heat flux mechanisms. Surfaces with artificial cavities, mixed wettability, and nanocoatings were fabricated, and systematically tested to understand the separate effects of surface morphology on pool boiling performance.

1.2.3 Development of new MEMS based techniques for surface modification

The third objective of this study is to integrate the available, and develop new MEMS-base techniques for fabrication of engineered surfaces applicable for boiling heat transfer applications. iCVD and new facile nano-grass fabrication techniques were successfully developed and integrated for boiling experiments.

1.2.4 Design and Engineering of High Performance Surfaces

Finally, in this dissertation, it is aimed to propose two surface enhancement techniques for increasing the boiling heat transfer performance for electronic cooling and refrigeration applications. In this section, the focus was on developing scalable and functional techniques for these industries. The effects of these techniques on boiling heat transfer and CHF were revealed and analyzed in detail.

2. Literature review

There are many cooling methods such as spray cooling [2, 3] and passive cooling techniques [4-6] involving phase change phenomena. Among phase change (liquid-vapor) phenomena, boiling is a widely used phenomenon in the industry [7]. Owing to a large amount of heat dissipation and achievable high heat transfer coefficients, it is one of the most effective heat transfer mechanisms for cooling and have applications ranging from electronic cooling and refrigeration to power generation [1, 8, 9].

Boiling heat transfer (BHT) and critical heat flux (CHF) are significantly affected by surface characteristics [10-12], working fluid properties including thermal conductivity and latent heat of vaporization [13, 14], as well as liquid-solid interfacial properties such as wettability. Surface modification is considered as one of the promising methods to enhance the efficiency of systems involving boiling [6, 9, 15-22]. With the help of material science and nanotechnology, many types of micro structured, nanostructured, hybrid structured and porous coated surfaces become available [23-25].

2.1 Boiling heat transfer (BHT)

Liquid to vapor phase change and forced convection are considered as the main nucleate boiling heat transfer mechanisms. In forced convection analogy, bubble behavior such as growth and departure is the mechanism for single phase heat transfer, while in phase change analogy evaporation and latent heat of vaporization is the mechanism for heat removal from the superheated surface. The three main heat transfer mechanisms are i) Transient conduction model, ii) Microlayer evaporation, and iii) Contact line heat transfer models.

2.1.1 Transient conduction model

According to this model (as shown in Figure 2.1) the departure of a bubbles push away the surrounding hot liquid layer, allowing the cold bulk liquid to get in contact with the superheated surface. Since this model assumes only surface rewetting for the period of bubble waiting time, no heat transfer from the heated wall to the working is considered during the bubble growth process. This implies a transient conduction heat transfer with the semi-infinite liquid.

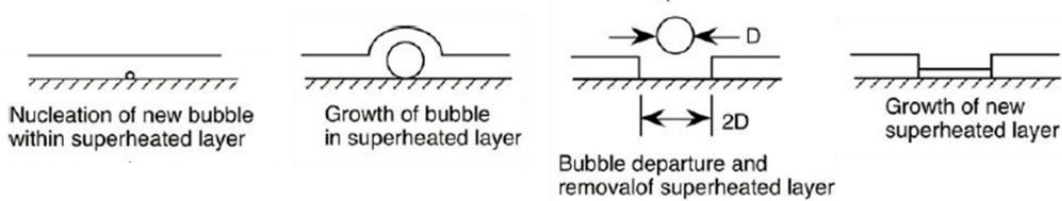


Figure 2.1 Transient conduction model [26]

2.1.2 Microlayer evaporation

Evaporation of a thin layer of liquid beneath the growing bubble is suggested by the microlayer evaporation model (also shown in Figure 2.2) as the heat transfer mechanism. As microlayer evaporates during the bubble growth period, resultant high liquid-to-vapor phase change heat transfer rate remarkably reduces the wall temperature. According to this model, the heat transfer during the bubble departure process should only be limited to the evaporation of the residual microlayer and there should be little heat transfer as the dry patch is rewet with liquid.

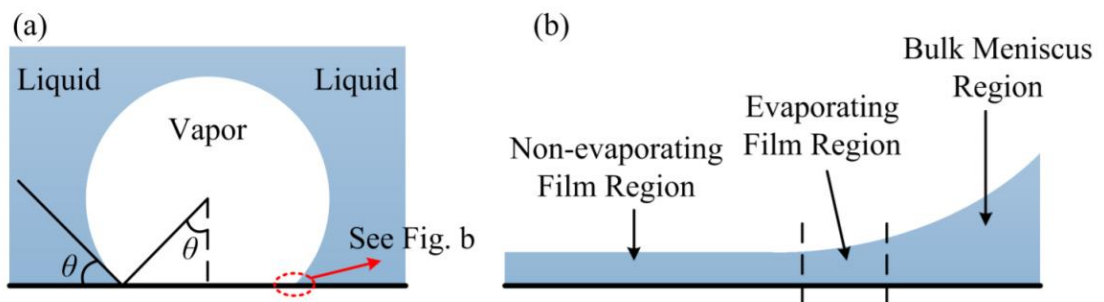


Figure 2.2 Schematic of the bubble base depicting the microlayer and its three regions

2.1.3 Contact line heat transfer model

Contact line heat transfer assumes that evaporation of a thin liquid meniscus at the three-phase contact line is the main heat transfer mechanism at nucleate boiling regime. The thickness of the mentioned liquid meniscus near the three phase contact line is very thin, which results in a high heat transfer rate in this region. Figure 2.3 compares the schematics of microlayer evaporation and contact line heat transfer mechanisms.

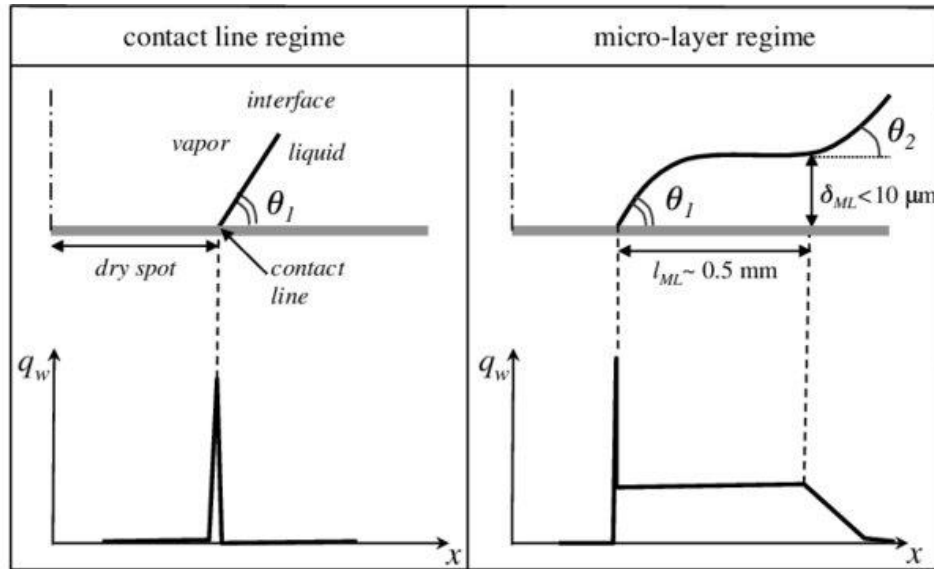


Figure 2.3 Scheme of the different nucleate boiling regimes, contact line (left) and microlayer (right), in terms of interface shape at the bubble foot (up) and wall heat flux profile (down)

2.2 Critical heat flux (CHF)

Critical heat flux is considered as the most important design parameter for any heat flux controlled boiling application. CHF is the upper thermal limit in such applications, and exceeding this flux triggers a rapid and unsteady transition from highly effective nucleate boiling to the inefficient film boiling region. This transition comes with a sharp increase in wall temperature leading to physical damage of the superheated surface. Three major pool boiling CHF mechanisms are reported in the literature; i) hydrodynamic instability, ii) macrolayer dryout, and iii) hot/dry spots [27]. Zuber's hydrodynamic instability has attracted much attention among these models, and many studies have improved the precision of the Zuber's theory by addition of several parameters in the original model.

2.2.1 Zuber's hydrodynamic instability

According to this model, prior to CHF vapor jets (downward and perpendicular to the superheated surface) are formed along the surface by the Taylor instability. As shown in Figure 2.4, the coalescence of Helmholtz instable - induced by velocity difference between downward water rewetting streams flowing through the upward vapor jets - vapor columns triggers the CHF occurrence. Zuber [28, 29] suggested the following model for prediction of hydrodynamic instability:

$$q_Z'' = \frac{\pi}{24} h_{fg} \left(\frac{\sigma g (\rho_f - \rho_g)}{\rho_g^2} \right) \quad 2.1$$

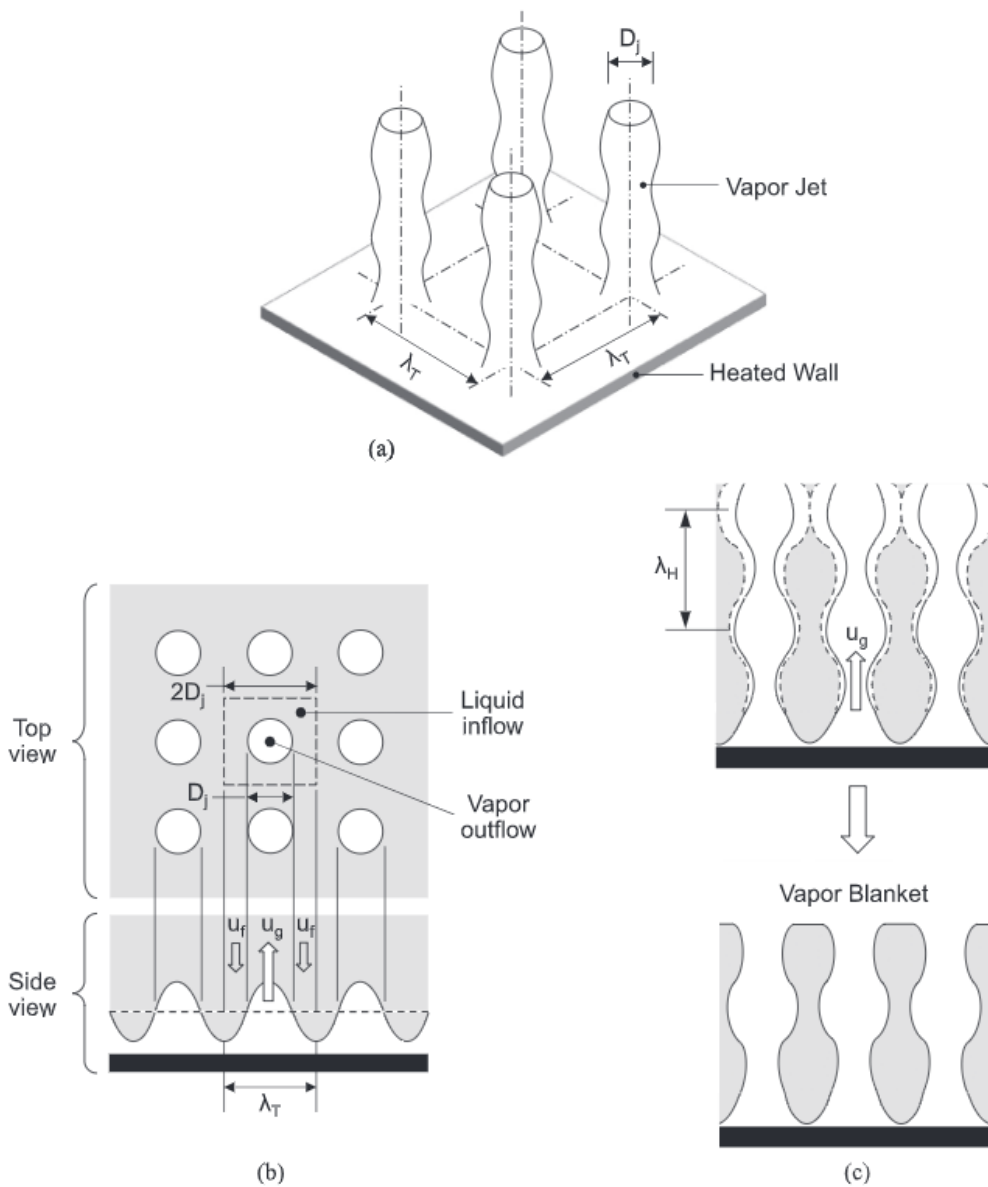


Figure 2.4 schematic of the Zuber hydrodynamic instability model. (a) Vapor jet formation prior to CHF. (b) Unit cell containing a single jet and surrounding liquid. (c) Vapor mushroom formation due to Helmholtz instability

2.2.2 Microlayer dry-out

Microlayer dry-out model, as shown in Figure 2.5, assumes that large numbers of vapor stems originating across the liquid macrolayers and cumulating in a large bubble as a result of the Helmholtz instability. Bang et al. [30], who experimentally confirmed the microlayer dry-out model as a possible mechanism for CHF, suggested that growth of the large bubble is the result of consumption of the macrolayer by evaporation, and that CHF is triggered when the liquid macrolayer dries out just before departure of the large bubble, which they expressed analytically as:

$$q''_{CHF} = \rho_f h_{fg} \delta (1 - A_g/A_w) f \quad 2.2$$

Here, δ and f are macrolayer thickness bubble departure frequency, respectively.

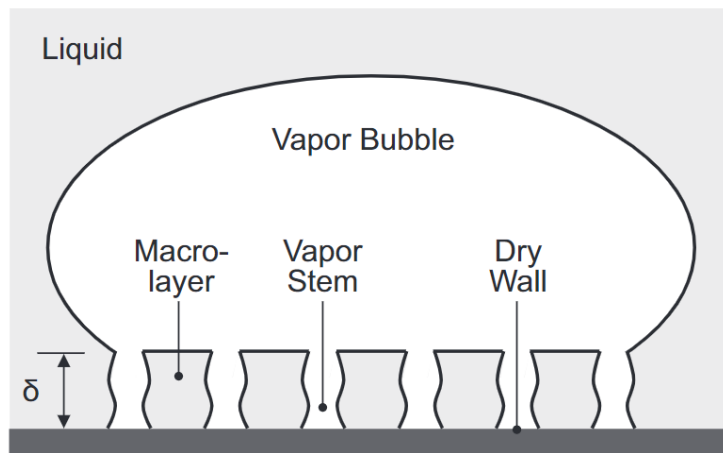


Figure 2.5 Schematic of dryout model

2.2.3 Hot/dry spots

According to this model, the presence of numerous dry spots on the boiling surface causes CHF occurrence. The irreversible growth of dry spots on the superheated surface triggers the CHF. Figure 2.6 shows the schematic of this model. Based on this model, Yagov [31] proposed different CHF correlations for low reduced pressures, $P/P_c < 0.001$, as:

$$q''_{CHF,l} = 0.5 \frac{h_{fg}^{81/55} \sigma^{9/11} \rho_g^{13/110} k_f^{7/110} g^{21/55}}{v_f^{1/25} c_{p,f}^{3/10} R_i^{79/110} T_{sat}^{21/22}} \left(\frac{\text{Pr}_f^{9/8}}{1 + 2 \text{Pr}_f^{1/4} + 0.6 \text{Pr}_f^{19/24}} \right)^{4/11} \quad 2.3$$

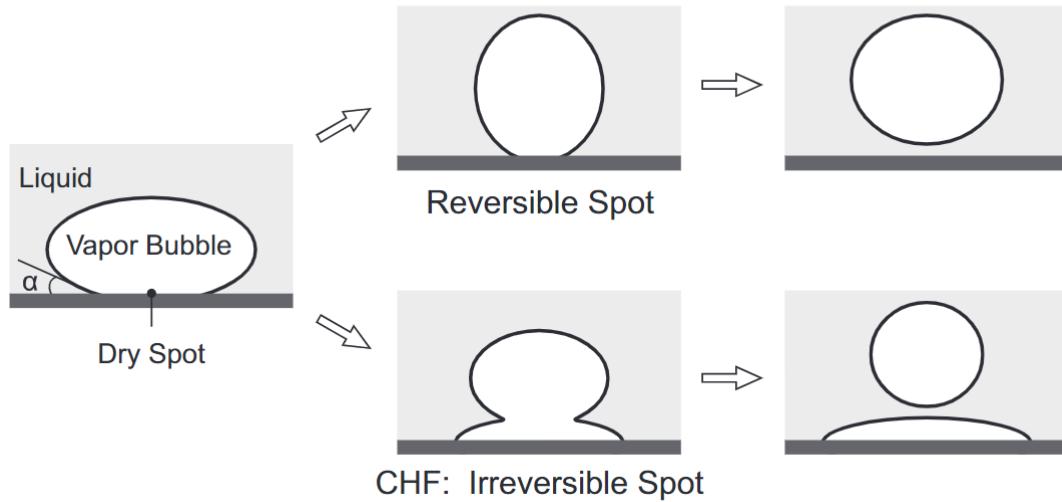


Figure 2.6 Schematic of hot/dry-spot model

2.3 Structured surfaces

Advances in Nano-electro-mechanical (NEMS) and Micro-electro-mechanical (MEMS) technologies have facilitated the fabrication of structures with sizes ranging from a few nanometers to hundreds of micrometers on silicon, metallic, polymer and ceramic surfaces. These fabrication techniques basically involve addition or subtraction of 2D layers on a substrate (usually silicon) based on photolithography or etching. Structured surfaces (micro or nano scale) and coating are among the methods that are implemented extensively for heat transfer and critical heat flux enhancement.

Micron sized square pin fin structures with diameters of $50 \times 50 \times 60 \mu\text{m}^3$ (width \times length \times height) and fin pitch size of $100 \mu\text{m}$ was fabricated and tested by Honda et al. [32]. Using wet etch techniques they modified the pin fin surfaces to form nanometer roughness with RMS of 32.4 nm. Accordingly they reported that both fin finned structured surfaces (with and without nano roughness) considerably enhanced nucleate boiling heat transfer (FC-72 as working fluid), while at low heat fluxes the chip with submicron size roughness performed better comparing to the pin finned chip without nano roughness. Wei and Honda [33] experimentally investigated the effect of height and

thickness of square micro pin fins on boiling heat transfer of FC-72 using six kinds of fin thickness as 30 and 50 μm and the fin height of 60–270 μm . Accordingly they found that the wall superheat in the developed nucleate boiling was lower for chips with larger surface roughness on fin wall sides. For fins with heights higher than 200 μm , a decrease in boiling curve was observed at high heat fluxes.

Pin fin shape elements with diameters and heights ranging from 1 to 25 μm and 10–100 μm , respectively, was fabricated and tested by Mitrovic and Hartmann [34, 35]. Using R141b as working fluid and copper as the substrate material. Using a patterned thin polycarbonate foil as mask, and electro-coating process (Electrophoretic deposition) they formed micro size copper structures on the copper substrate. The authors showed that the pin finned structure surfaces has much better performance in terms of boiling heat transfer. Utilizing the same method of electro-coating process with polycarbonate foil, Ustinov et al. [36] fabricated inclined pin fin structures on copper surfaces and performed boiling experiments on R134a and FC-3284. The authors reported that the micro structure efficiency is higher when the critical vapor diameter is comparable fin pitch size. Also due to larger lengths of three phase line, it was concluded that surfaces with larger number of fins had better cooling performance.

In an study conducted by Launay et al. [37] different types of surfaces with micro and combined micro/nano structured surfaces were tested in a pool of water and PF-5060. Seven types of surfaces as smooth silicon surface, rough silicon surface ($R_a=0.8\text{--}1.4\mu\text{m}$), CNT coated smooth silicon surface (CNT height = 40 μm), pin fin structured silicon surface ($W\times P\times H: 70\times 250\times 200\mu\text{m}$), CNT coated silicon surface ($W\times P\times H: 70\times 150\times 100\mu\text{m}$ with CNT height of 100 μm), and two 3D structure silicon surfaces were fabricated. The authors concluded that compared to smooth silicon surfaces, the CNT coatings (purely nano-structured surfaces) only enhances heat transfer at low wall superheats. Also it was shown that the micro structured silicon surface (using dry etching) outperforms the CNTs-based surfaces in all cases examined.

Using wet etching (KOH solution), Zhang and Lian [38] micro pin fins with width and height of 200 and 35 μm , respectively, and fin pitch sizes ranging from 200 to 1000 μm . Using DI water as working fluid, pool boiling experiments were performed by the authors and it was concluded that under experimental conditions surface with with pin-fin spacing of 200 μm had the best boiling heat transfer among the tested samples.

Microscale, nanoscale and combined micro-nanoscale surfaces were fabricated and tested by Kim et al. [39]. Microscale surfaces were fabricated using tetramethyl ammonium hydroxide etchant (wet etching) and nanoscale structures were fabricated by growing ZnO nanorods on silicon surfaces and sinking them into zinc nitrate hexahydrate and ammonium hydroxide solution. The authors showed that the micro-nanoscale surfaces (combined effects of micro and nanostructures) performed better in term of critical heat flux (CHF), while micro structured surfaces presented better nucleate boiling heat transfer coefficient.

Cooke and Kandlikar [40] fabricated five different microscale structures on silicon surfaces and conducted water boiling experiments. The shapes of the microstructured surfaces included various microchannel geometries (depth ranging from 180 to 270 μm and width ranging from 40 to 200 μm), notch structures at channel sidewalls, and offset strip fin structures. The authors concluded that the chip with the 200 μm width and 275 μm depth show the best performance in terms of boiling heat transfer. Nano structures

As an example, Chu et al. [15] conducted an experimental study to show the effect of structured surfaces on pool boiling heat transfer. They used microstructures with a wide range of roughnesses to enhance critical heat flux. Ahn et al. [41] developed a nano-structured surface using multi walled carbon nanotubes and reached a critical heat flux enhancement of 40% in pool boiling. These surfaces could play a role in enhancing nucleation bubble sites [42-46] or changing in wettability [47-49]. There are many studies, which analyze the bubble generation [50-52] and enhancement of pool boiling heat transfer via generating more active nucleation sites [53-56].

2.4 Coated surfaces

Recently, the effects of textured surfaces such as nanowire arrays [57, 58], porous media [18, 59] and graphene structures [60, 61] on boiling heat transfer and CHF were investigated in the literature. Wettability is one of the most important factors in two-phase heat transfer due to the control of dynamic triple contact lines, which are inter-connected lines for liquid, solid, and gas phases [62, 63]. On the other hand, miniaturization of heat transfer systems leads to the increase in the effect of interfacial forces, thereby emphasizing on the important role of wettability in boiling heat transfer [64]. The role of

high surface wettability on CHF enhancement was reported by Wang and Dhir [56]. Two years later, Vinogradova et al [65] reported that nucleation occurs more likely on hydrophobic surfaces due to higher concentrations of trapped air in sub-micron size cavities compared to hydrophilic surfaces. While hydrophilicity enhances CHF, hydrophobic surfaces promotes bubble nucleation; thereby making the effect of wettability on boiling complex.

In 2010, Betz et al [66] showed that mixed hydrophilic and hydrophobic surfaces enhanced both heat transfer coefficient and CHF. They conducted experiments on hydrophilic networks (hydrophilic surface with hydrophobic islands) and hydrophobic networks (hydrophobic surface with hydrophilic islands). They reported that hydrophilic networks had a better performance via preventing formation of an insulating vapor blanket compared to hydrophobic networks. Afterwards, superbiphilic surfaces were used to assess the effect of super hydrophilic surface with super hydrophobic islands [67]. In the related study, critical heat fluxes over 100 W/cm^2 and heat transfer coefficients more than $100 \text{ kW/m}^2\text{K}$ were obtained.

Many of investigators have used porous surfaces to show their effects on heat transfer [68-72]. Xu et al. reported a 120% enhancement in heat transfer using a composite copper porous surface relative to the plain surface [73]. Lee et al. [74] enhanced nucleate boiling heat transfer and also achieved lower wall superheat in pool boiling using nano-porous surfaces. Li et al. [75] investigated the effect of multiscale modulated porous structures on pool boiling, and three times larger heat transfer coefficients relative to the plain surface were reported. Tang et al. [76] utilized metallic nanoporous surfaces, and significant enhancement in cooling and heat transfer coefficient was observed. Deng et al. [77] developed a porous coating with reentrant cavities. This porous coating increased the number of bubble nucleation sites and prevented early condensation. Reentrant cavity made liquid replenishment and surface rewetting much easier. Reentrant cavities were able to trap vapor during bubble nucleation; as a result, stable bubble nucleation sites were provided leading to enhancement in pool boiling [78].

Storr [79] investigated the effect of heating surface orientation and revealed that the vertical surface has more heat dissipation rate compared to the horizontal surface. Githinji and Sabersky [80] compared pool boiling performance of heating surfaces with 0° (facing up) and 90° (vertical) angles. Heat transfer rate increased with the inclination angle.

Rainey and You [81] investigated the effect of heater size and orientation on pool boiling heat transfer on inclined microporous surfaces. Pool boiling heat transfer coefficient had an increasing trend from 0° to 45° and a decreasing trend from 90° to 180° orientation. Ho et al. [82] studied the effect of surface orientation on pool boiling using bare silicon and fully coated carbon nanotube surfaces. Experiments were conducted for inclination angles of 0° , 30° , 60° , 120° , 150° and 180° , and they observed that heat transfer coefficient increased from 0° to 90° .

Due to the porous structure of pHEMA (polyhydroxyethylmethacrylate) surfaces and swelling property upon contact with water, they started to be employed in boiling studies [83]. Sadaghiani et al. [84] investigated the effect of pHEMA coated surfaces on flow boiling in high aspect ratio rectangular microchannel, while Cikim et al. [85] presented an experimental study using pHEMA coatings in mini/microtubes on flow boiling and reported a 126% enhancement in boiling heat transfer.

Seo et al. [86] examined pool boiling heat transfer on nano-porous graphene layered-deposited surfaces, which were prepared by rapid thermal annealing (RTA) method. Enhancement in CHF was explained by high porosity and permeability of graphene coating and subsequent effects of these parameters on hydrodynamic and capillary pumping limits. Jaikumar et al. [87] investigated the effect of graphene and graphene oxide coatings on pool boiling enhancement. They transferred the mixture of graphene and graphene oxide (GO) to copper plain samples by the dip coating method. They reported enhancements of 42% and 47% for CHF and heat transfer coefficient, respectively. They also showed that the pool boiling performance was notably impeded by the increase in coating thickness of graphene and GO layer. Afterwards, Jaikumar et al. [88] presented the combined effect of graphene oxide and porous copper particles on pool boiling enhancement. Rapid nucleation activity, high wettability as a result of roughness augmentation, and wicking-enabled dendritic structures were mentioned as the contributing mechanisms for CHF and HTC enhancements.

Recently, several studies have been conducted on the methods for increasing NBHT on heater surfaces with porous structures. A porous surface generally has pores ranging from one to hundreds of micrometers, correlated with activated cavity size in the boiling surface. Chang and You [82], [83] and Hwang and Kaviany [85] observed NBHT with respect to the particle size of porous layer. Chang and You [82] recorded the highest

NBHT performance on 20 μm particles among 2–70 μm samples (Fig. 17a). Hwang and Kaviani [85] recorded relevantly higher NBHT on 40 μm particles among 40, 80, and 200 μm particles (Fig. 17b). Liang and Yang [75] reported that a copper composite porous surface with excellent thermal conductivity showed the highest NBHT among micro-graphite fiber, aluminum, and copper composite porous surfaces (Fig. 17c). Recently, Ahn et al. [102], [103] reported that 3D graphene foam with 5–10 μm pores demonstrated a significant increase in NBHT because of their excellent thermal conductivity.

The effect of graphene coatings on boiling heat transfer has been investigated in a number of studies. Most of them focused on the graphene layer coating and resulting deposition of graphene suspensions on a heated surface. For example, Kim et al. [89] investigated critical heat flux (CHF) enhancement in a graphene oxide (GO) colloidal suspension. In their experiments, nucleate boiling was performed on a surface coating, which formed as a resulted deposition of GO colloids. It was reported that the thickness of the deposited layer was approximately proportional to the observed increase in CHF. Using the graphene/graphene oxide suspensions in water, Park et al. [90] examined the effect of nano-sheet deposition on critical heat flux. They concluded that the nano-sheet porous structure formation (due to its own self-assembly characteristic) resulted in critical instability wavelength alteration, which eventually enhanced critical heat flux. 3D foam-like reduced graphene oxide (rGO) was used by Ahn et al. [91, 92] to prevent heater failure during boiling. They showed that due to the excellent thermal conductivity graphene coated layer prohibited preparation of hot spots, resulting in CHF enhancement.

Part 2: Fundamental studies on pool boiling

3. Artificial cavities

3.1 Introduction

In this chapter, pool boiling experiments on artificial cavities are presented. Here surfaces with different cavity (hole) geometry and wettabilities are fabricated to investigate the effect of surface morphology on BHT and CHF. Microelectromechanical systems (MEMS) technology was employed both for the fabrication of artificial cavities and modification of surface wettability. The effects of hole diameter, pitch distance, and surface wettability were examined during pool boiling experiments. The depth of the cavities was fixed to 32 μm , while diameters were 50, 100 and 200 μm , and the pitch sizes were 500, 1000 and 2000 μm . For assessing the wettability effects on pool boiling, a 50 nm thick Teflon film was coated on the surface. Boiling heat transfer, critical heat flux and bubble dynamics characteristics were observed by using a high-speed camera and parametric results, the effects of surface wettability on nucleation site interactions and critical heat flux were discussed in detail.

3.2 Sample preparation and characterization

The process flow of the fabricated samples is shown in Figure 3.1. The sample preparation procedures can be summarized as follows: A 500 μm thick silicon wafer was used as the substrate of the test specimens. The MEMS based fabrication methods were adopted to prepare micro-cavities. Several drops of a positive photoresist (PR) (GXR-601, AZ) were deposited on the top side of the Si wafer, and the wafer was rotated at 2,000 rpm for 30 s in a spin coater. Then, thin layer of PR was formed and was baked on a hot plate at 100 $^{\circ}\text{C}$ for 60 s to evaporate remaining solvents in the PR layer. A mask, which had arrays of micro-holes, was placed on the PR layer, and UV light was emitted on them. After developing in AZ 300 MIF solution, the arrays of micro-holes were

realized on the PR layer. During etching process, the masked region underneath the PR layer was protected, so that only unmasked holes were etched at a certain depth. The geometries of formed included in Table 3-1. Their depths were fixed to about 32 μm . Residual PR in the masked layer was completely removed in a acetone solution, and the cavity-structured-substrate was rinsed by ethanol and DI water in sequential manner and was dried by nitrogen gas. Then, the substrate was diced into pieces ($15 \times 15 \text{ mm}^2$) to be used in pool boiling experiments. Fabricated cavity structures could be verified by a scanning electron microscope (SEM). Figure 3.2 displays cavity structures without any tapering. For hydrophobic specimens, a thin Teflon layer ($\sim 50 \text{ nm}$) was coated on the hole-structured surface. A small drop of 0.6 % of Teflon solution (AF1600, Dupont) was placed on the substrate, and spin coating process (500 rpm, 30 s) was carried out followed by baking process ($120 \text{ }^\circ\text{C}$, 4 h). The Teflon coated surface is of hydrophobic nature with the static contact angle of 121 ° , while the original Si surface is hydrophilic with a contact angle of (70 °) as shown in Figure 3.3.

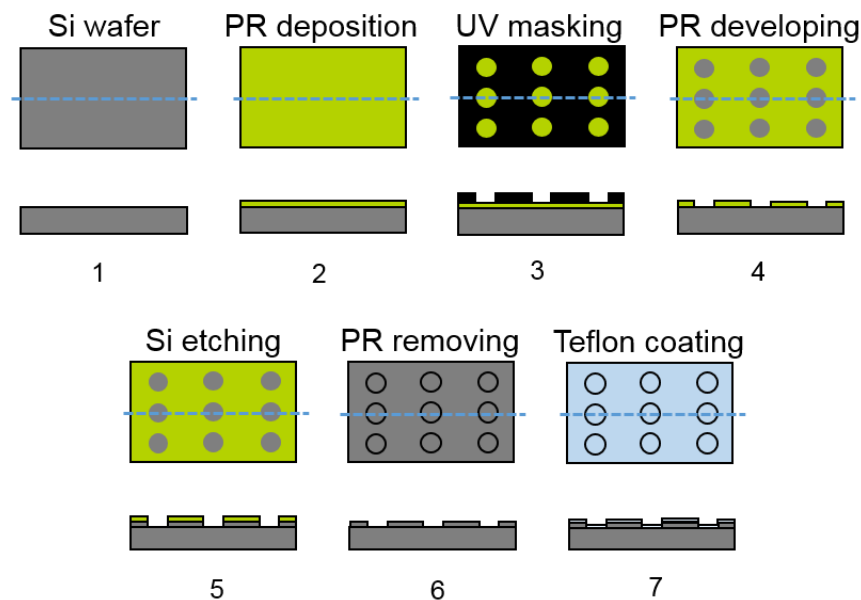


Figure 3.1 Fabrication process flow of the prepared samples

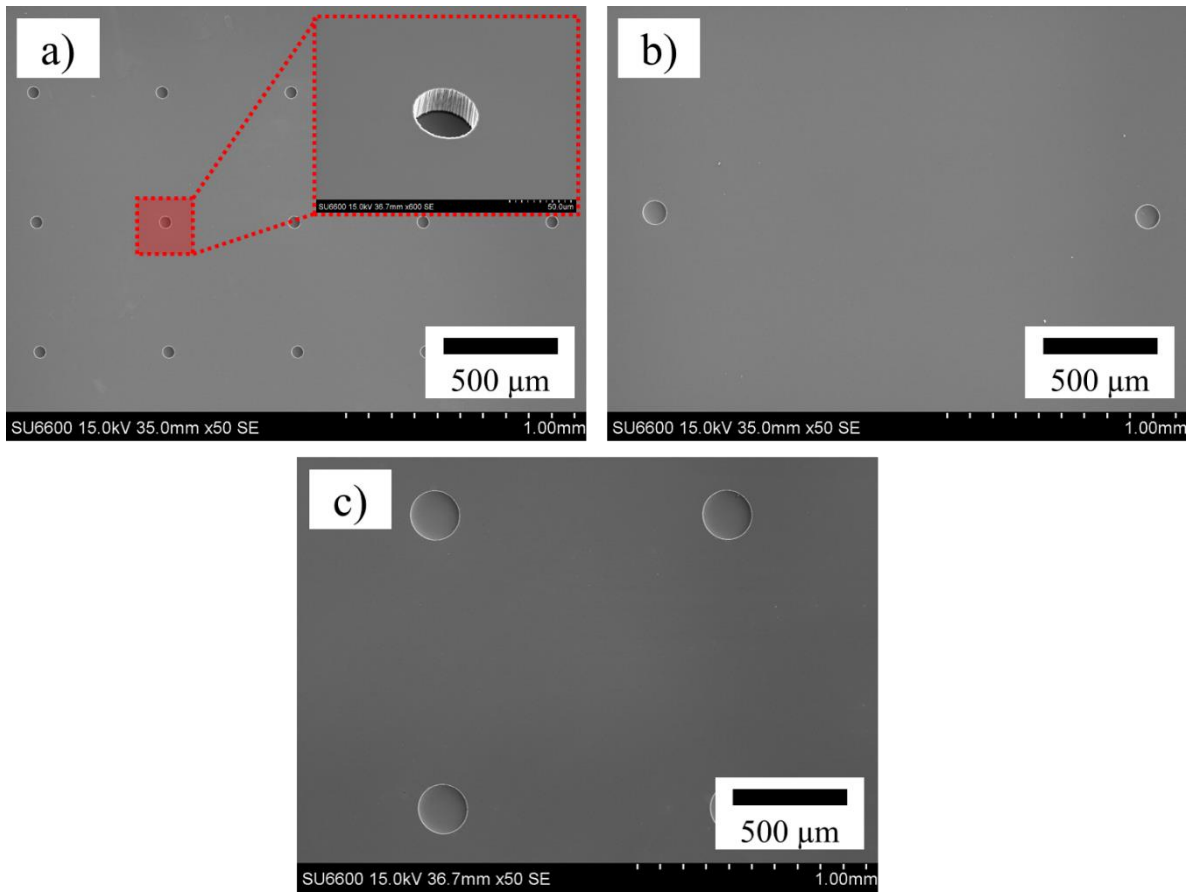


Figure 3.2 SEM images of three test specimens: a) 50-500-phil, b) 100-2000-phil, c) 200-1000-phil

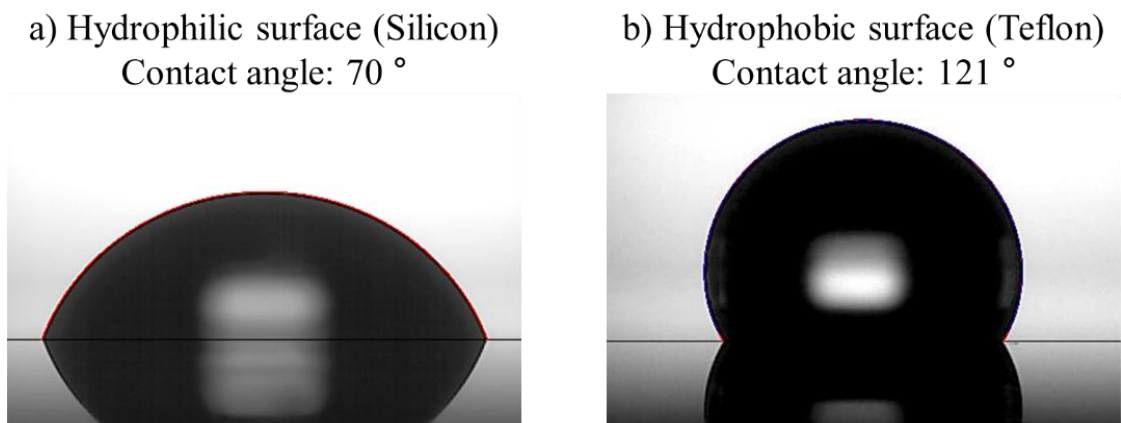


Figure 3.3 Static contact angles of substrates a) without Teflon coating, b) with Teflon coating

Table 3-1 Characteristics of fabricated samples

Sample No	Sample name	Hole diameter	Hole pitch size	Contact angle
No #1	50-500-phil	50 μm	500 μm	70°
No #2	50-2000-phil	50 μm	2000 μm	70°
No #3	100-500-phil	100 μm	500 μm	70°
No #4	100-2000-phil	100 μm	2000 μm	70°
No #5	200-500-phil	200 μm	500 μm	70°
No #6	200-1000-phil	200 μm	1000 μm	70°
No #7	200-2000-phil	200 μm	2000 μm	70°
No #8	50-500-phob	50 μm	500 μm	112°
No #9	50-2000-phob	50 μm	2000 μm	112°
No #10	100-500-phob	100 μm	500 μm	112°
No #11	100-2000-phob	100 μm	2000 μm	112°
No #12	200-500-phob	200 μm	500 μm	112°
No #13	200-1000-phob	200 μm	1000 μm	112°
No #14	200-2000-phob	200 μm	2000 μm	112°

3.3 Results and discussion

Pool boiling experiments were performed on 14 different surfaces with artificial cavities (holes) to investigate the effects of wettability, hole diameter and pitch size on BHT and CHF. The 32 μm deep circular cavities with the diameters of 50, 100, and 200 μm , the pitch sizes of 500, 1000, and 2000 μm were utilized. The 50nm thick Teflon thin films were coated on the samples to investigate the effect of surface wettability. Using a high speed camera, visualization study was performed to study bubble dynamics and related parameters such as the bubble departure diameter, the bubble departure frequency, the bubble coalescence as well as the critical heat flux mechanisms on fabricated samples. In the presented results “D” stands for the diameter of the hole, “P” represents the pitch size, and “phil” and “phob” are the indications of hydrophilic (uncoated) and hydrophobic (Teflon coated) surfaces, respectively. For example a sample denoted as D50-P2000-phil is the structured surface with the hole diameter of 50 μm , the pitch size of 2000 μm , and hydrophilic surface.

3.3.1 Bubble nucleation and growth

Single bubble nucleation, growth, and departure on hydrophilic and hydrophobic structured surfaces remarkably differ mainly due to the three-phase contact line behavior. Figure 3.4 shows the schematic of bubble nucleation and growth on the structured surfaces. Apart from the surface wettability, the onset of nucleate boiling occurs at the predefined cavities (holes) because artificial holes provide a suitable hydrothermal layer for bubble nucleation in addition to increasing the contact area overall. Hydrophobic surfaces have lower surface energy resulting in early nucleation at the lower wall superheats compared to hydrophilic surfaces. The shape and size of the bubbles during the nucleation and growth periods also change with surface wettability such that bubbles tend to grow within the allocated nucleation site (artificial cavities) on hydrophilic surfaces, while generated bubbles spread on the hydrophobic surfaces.

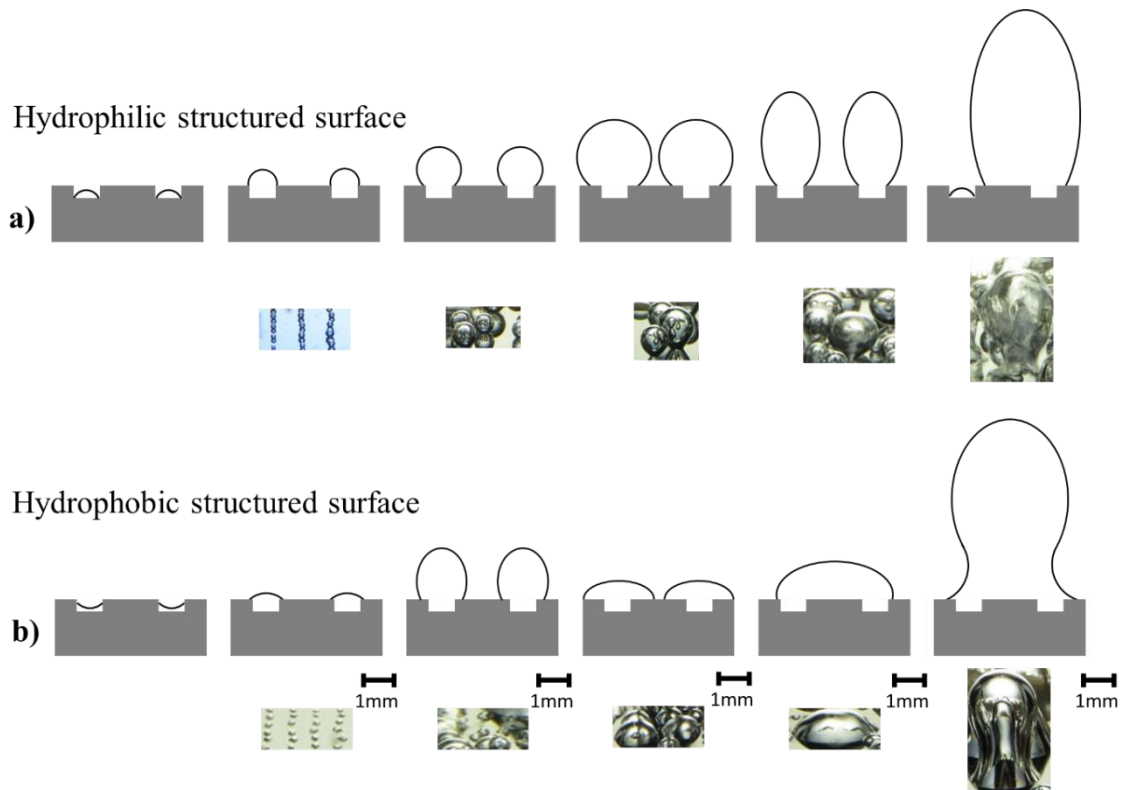
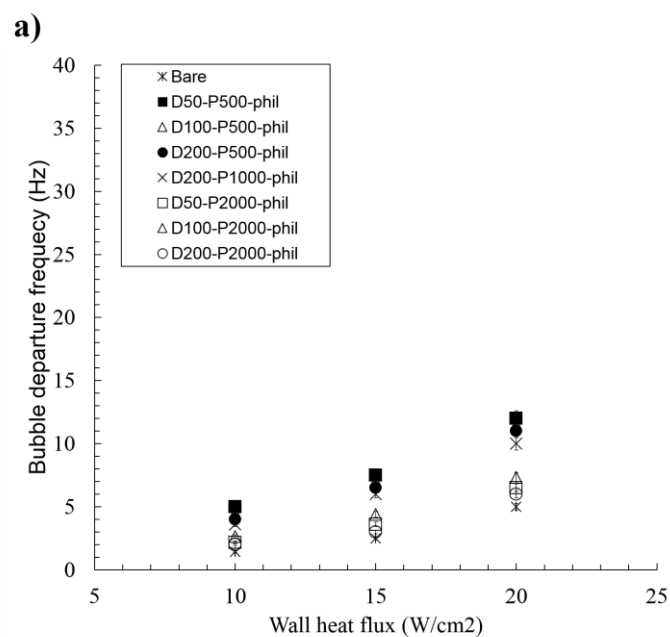


Figure 3.4 Bubble nucleation and growth on a) hydrophilic structured b) hydrophobic structured surfaces

Holes (cavities) geometries and configurations contribute to the increase in bubble departure frequency. Figure 3.5 shows bubble departure frequencies and departure

diameters of the tested samples in the nucleate boiling regime ($0K < \Delta T_{\text{sup}} < 15K$). Prior to bubble departure from a single cavity, bubble coalescence takes place on hydrophobic surfaces, especially for smaller pitch size samples. During the bubble departure on structured hydrophobic surfaces, while the whole bubble departs, a small amount of vapor remains on the surface, leading to continuous nucleation cycle with no waiting time and to higher nucleation frequencies relative to the hydrophilic samples [22, 93, 94]. Bubble departure frequency is calculated by averaging the obtained values for at least 10 nucleation sites per case, where 5 sequential bubbles in the images were tracked from growth initiation to the instance they reached to the middle of the image frame (the same method as previous studies [18, 95, 96]). Manual pixel-wise calculation was performed to determine the locations of diametrical points of bubbles. For each time interval, the bubble centroid location was obtained by averaging the diametrical x and y coordinates. When the bubble radial growth becomes constant, time history of vertical position of the bubble centroid approximates the bubble departure frequency. This approximation is in agreement with Rayleigh [97], Mikic, Rohsenow, and Griffith [98].



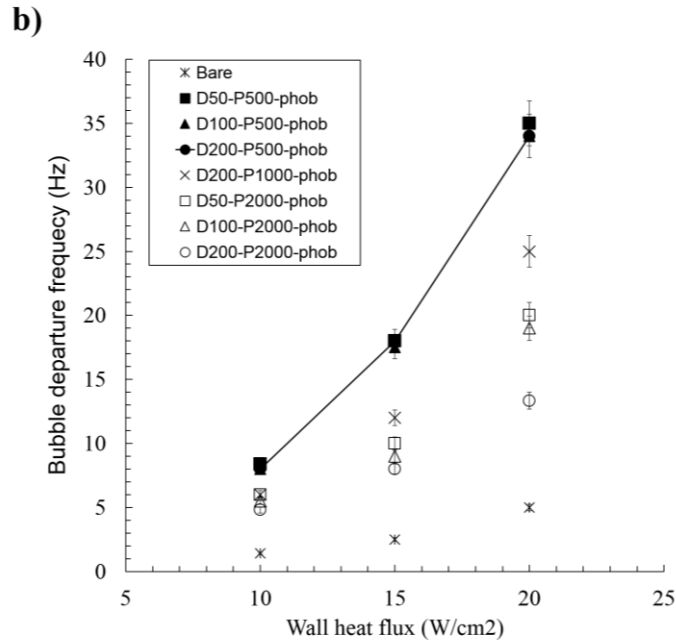


Figure 3.5 Bubble departure frequency for a) hydrophilic samples and b) hydrophobic samples

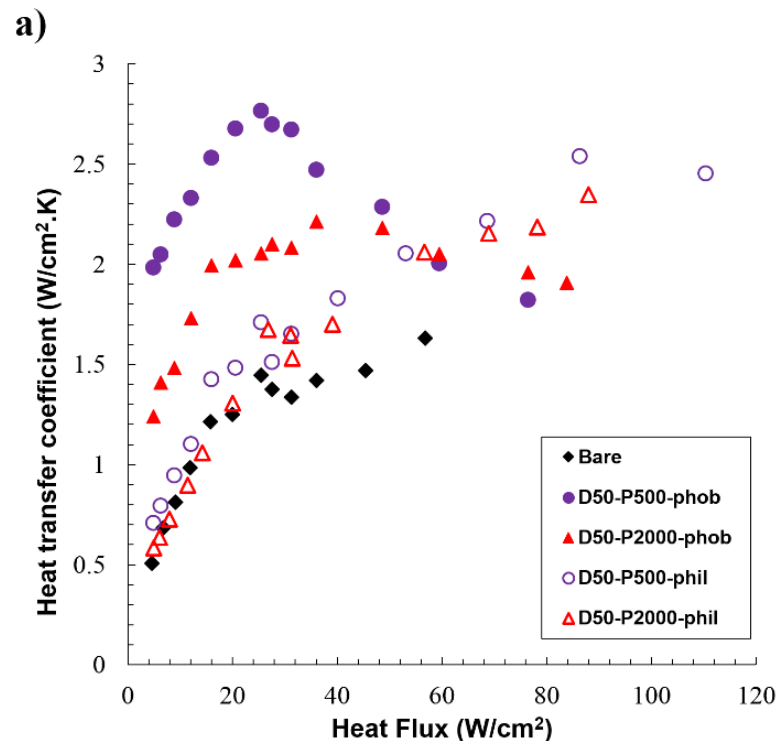
Mikic and Rohsenow [99] presented a theory on the relationship of boiling heat transfer with nucleation site density and bubble departure diameter. They showed that a higher number of active nucleation sites, leads to higher heat transfer coefficients likely due to the greater amount of heat removed through the latent heat of the evaporation via higher number of bubbles forming, which supporting our experimental results.

3.3.2 Boiling heat transfer

Figure 3.6a and Figure 3.6b show the obtained heat transfer coefficients as a function applied wall heat flux for structured surfaces with pitch sizes of 500 and 2000 μm , respectively. At a fixed pitch size, structured surfaces with a smaller hole diameter have lower wall superheats at a fixed heat flux resulting in a higher boiling heat transfer coefficient. The maximum boiling heat transfer coefficient on structured surfaces was obtained with the Sample D50-P500-phob leading to an average enhancement of 110% relative to the bare silicon surface. The effect of hole diameter on boiling heat transfer diminishes with pitch size. As an example, the samples with hole diameter of 50 μm and pitch sizes of 500 and 2000 μm (sample NO #1 and NO #2, respectively) show 25% and 35% average heat transfer enhancement, while the samples with hole diameter of 200 μm and pitch sizes of 500 and 2000 μm (sample NO #5 and NO #7, respectively) offer 10%

and 4% average heat transfer enhancement relative to the bare silicon surface for the entire range of wall heat fluxes. The results imply that the effect of pitch size is more dominant on hydrophilic surfaces with smaller hole diameter, which is mainly due to the difference in bubble growth phenomena on structured hydrophilic and hydrophobic surfaces. Nucleated bubbles on structured hydrophobic surfaces tend to coalesce at much lower wall temperatures and to enhance nucleate boiling heat transfer.

The obtained heat transfer coefficients for hydrophobic surfaces show a sharp decrease after maximum heat transfer rate around heat flux of $q'' \approx 40 \text{ W/cm}^2$. The sharp reduction in heat transfer coefficient, especially for the sample D50-P500-phob, is attributed to vapor blockage and vapor flow resistance near immediate cavities. Downward Liquid flow (rewetting flow) path decreases as the number, size, and departure frequency of generated bubbles increase. At a certain heat flux – critical heat flux - the vapor flow completely blocks the rewetting flow path. Temporal dry-out is in fact a consequence of this situation on superheated surfaces.



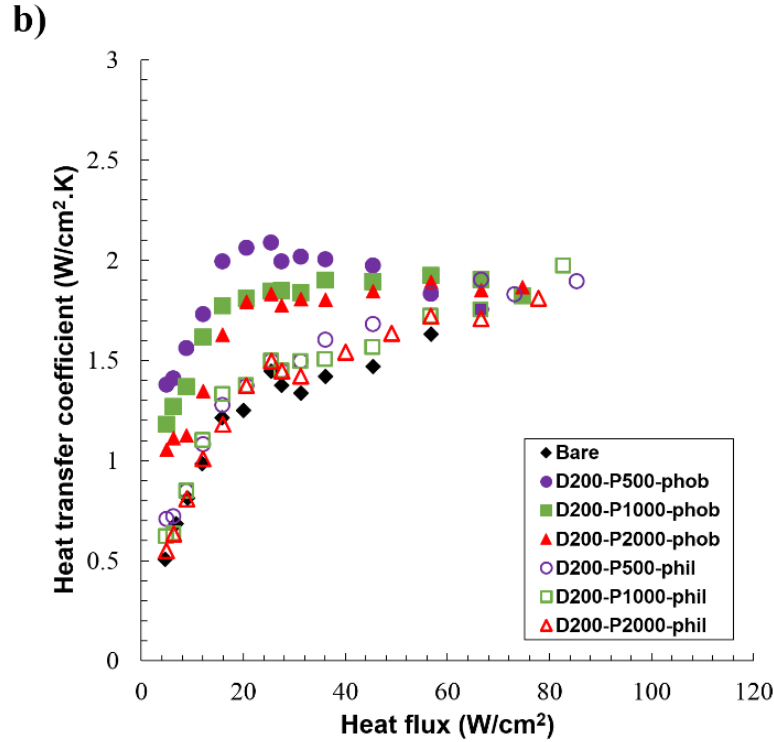


Figure 3.6 Obtained heat transfer coefficients for hydrophobic and hydrophilic surfaces a) at different pitch sizes with hole diameter of 50 μm b) at different pitch sizes with hole diameter of 200 μm

Although the number of nucleated bubbles changes depending on the aerial density of artificial cavities (holes) on the tested surfaces, at low wall superheats, generated bubbles on hydrophobic surfaces with comparable pitch/hole diameter ratios merge and form larger bubbles (pitch size/hole diameter = 2.5 and 5). On the other hand, hydrophilic structured surfaces with pitch size/diameter ratio larger than 10 (pitch size/ hole diameter = 10, 20, and 40) mostly experience bubble coalescence at moderate wall temperatures ($10 < \Delta T_{\text{sup}} < 20$). According to the visual results, vertical, horizontal, and vertical-horizontal types of bubble coalescence occur during bubble departure process (Figure 3.7). Vertical coalescence happens when generated bubbles are close to each other, a situation that occurs when the aerial density of artificial cavities, i.e. the nucleation site density, is relatively high. Depending on the surface wettability and morphology the merged larger bubble remains on the surface or depart from the surface. Compared to the hydrophobic samples, hydrophilic surfaces tend to keep the merged bubble on the superheated surface for longer period of time, with larger bubble size at the departure time. Furthermore, the effect of pitch size is more dominant on surfaces with smaller hole

diameter ($50\ \mu\text{m}$). Figure 3.7 shows the schematic of bubble coalescence types on hydrophilic structured surfaces.

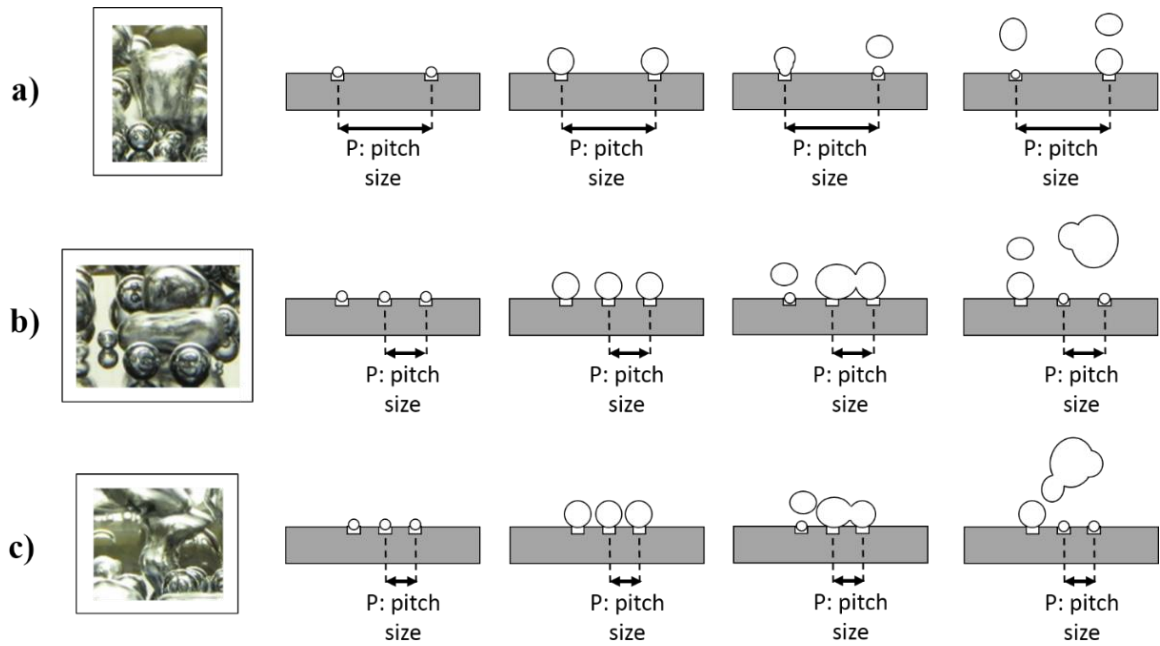


Figure 3.7 Different types of bubble coalescence on structured surfaces a) horizontal b) vertical c) horizontal-vertical

Figure 3.8 shows the comparison in visual results of bubble behavior between hydrophilic and hydrophobic (Teflon coated) surfaces with pitch size of $500\ \mu\text{m}$ at low ($0\text{K} < \Delta T_{\text{sup}} < 5\text{K}$) and high ($25\text{K} < \Delta T_{\text{sup}} < 35\text{K}$) wall superheats. At low wall superheats, structured surfaces with smaller hole diameter have higher bubble departure frequency and smaller bubble waiting time, a point mentioned in the text. At a fixed pitch size, smaller hole diameter implies more nucleation sites on the superheated surface, which further enhances the boiling heat transfer. As the wall heat flux increases, larger vapor blankets and columns start to appear on the heating surface.

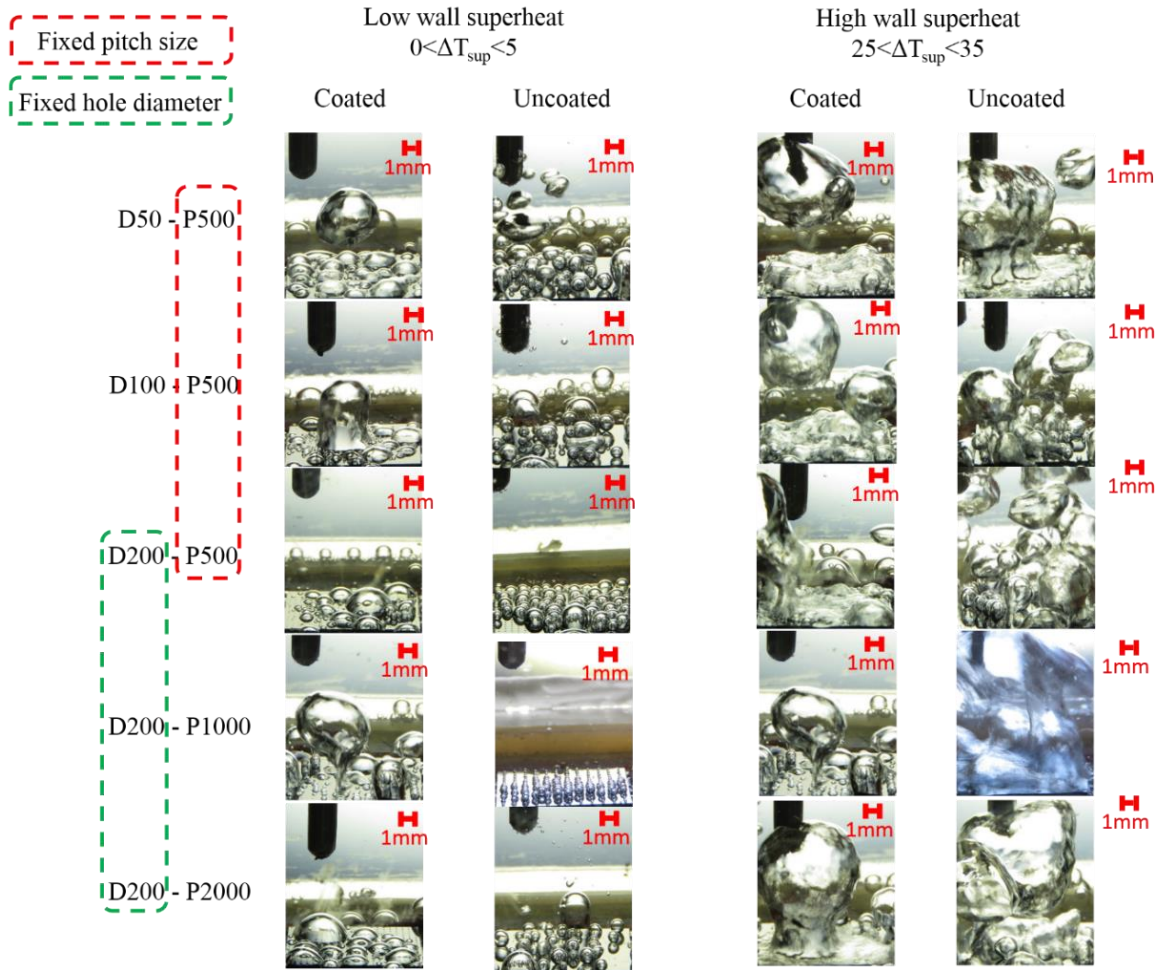


Figure 3.8 Individual bubbles and vapor columns shapes on hydrophilic and hydrophobic structured surfaces – effect of hole diameter and pitch size

Another reason for boiling heat transfer enhancement on hydrophobic surfaces is rapid bubble motion speed on the hot surface, which enhances surface wetting at moderate wall superheats. Figure 3.9 shows this motion for a time period of 52 ms on the sample NO #10 (D100-P500-phob).

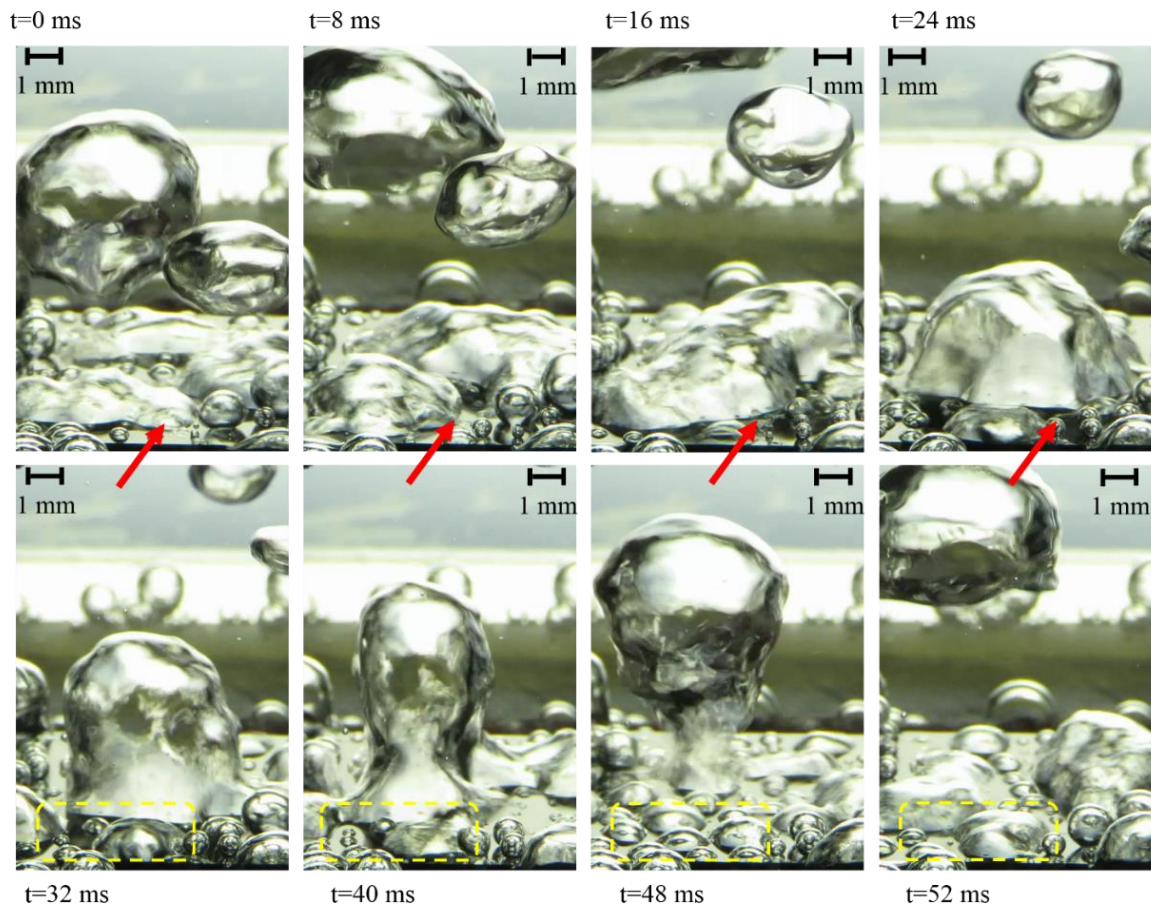


Figure 3.9 Bubble/vapor blanket motion on hydrophobic structured surface NO #8 (D50 – P500 – phob)

Table 3-2 shows the bubble coalescence types on tested samples at different wall superheats. In Table 3, “V” and “H” stand for “vertical” and “horizontal” coalescence types (as shown in Figure 8), respectively. To indicate the effect of hole diameter and pitch/diameter ratios, green and red colors are used, respectively. For example, sample No#1 (hydrophilic surface, $D=50\mu\text{m}$, $P=500\mu\text{m}$, and $P/D=10$) at $5\text{K} < \Delta T_{\text{sup}} < 10\text{K}$ experiences only vertical bubble coalescence, while at $10\text{K} < \Delta T_{\text{sup}} < 15\text{K}$ both vertical and horizontal bubble coalescences happen.

Accordingly, It was found that regardless of surfaces wettability, samples with $P/D \leq 10$ (pitch size/hole diameter) experience horizontal bubble coalescence at low wall temperatures ($0\text{K} < \Delta T_{\text{sup}} < 10\text{K}$). The obtained results also indicated that at low wall superheat, vertical coalescence occurs on surfaces with hole diameter of $50\mu\text{m}$, which is mainly due to high bubble departure frequencies at these samples (Figure 6). No bubble

coalescence was observed on hydrophilic surfaces (samples #1 to #7) at $0K < \Delta T_{sup} < 5K$, which is the main reason for their low heat transfer coefficients (Figure 3.6).

Table 3-2 Bubble coalescence type on tested samples at different wall superheat values

Sample characteristics					Bubble coalescence type	
Wet.	No	D (μm)	P(μm)	P/D	$0K < \Delta T_{sup} < 5K$	$5K < \Delta T_{sup} < 10K$
Hydrophilic	#1	50	500	<u>10</u>	-	Vertical
	#2	50	2000	40	-	Vertical
	#3	100	500	<u>5</u>	-	Horizontal
	#4	100	2000	20	-	-
	#5	200	500	<u>2.5</u>	-	Horizontal
	#6	200	1000	<u>5</u>	-	Horizontal
	#7	200	2000	<u>10</u>	-	-
Hydrophobic	#8	50	500	<u>10</u>	Vertical + Horizontal	Vertical + Horizontal
	#9	50	2000	40	Vertical	Vertical + Horizontal
	#10	100	500	<u>5</u>	Horizontal	Vertical + Horizontal
	#11	100	2000	20	-	Vertical
	#12	200	500	<u>2.5</u>	Horizontal	Horizontal
	#13	200	1000	<u>5</u>	Horizontal	Horizontal
	#14	200	2000	<u>10</u>	Horizontal	Horizontal

3.3.3 Critical heat flux (CHF)

Critical heat flux (CHF), the upper thermal limit in pool boiling, appears with a drastic increase in the wall temperature. Five different pool boiling CHF mechanisms were reported in the literature [27]. Among these mechanisms, hydrodynamic instability [28] and dry-out [100] have attracted much attention. Figure 3.10 shows the schematic of hydrodynamic instability and dry out model on a horizontal plate.

According to the hydrodynamic model (Figure 3.10a), the correlation for the CHF with some simplifications was developed as follows:

$$q''_{CHF,Z} = \left(\frac{2\pi\sigma}{\rho_v \lambda_H} \right)^{1/2} \rho_v h_{fg} \frac{A_{column}}{A_{surface}} \quad (3.1)$$

In this equation, λ_H is the Taylor wavelength – with a value, which lies between the critical wavelength (λ_c) and the most dangerous wavelength (λ_D), $u_c = \sqrt{2\pi\sigma/\rho_v\lambda_H}$ represents the critical velocity of the vapor column induced by the Helmholtz instability, $A_{\text{column}}/A_{\text{surface}} = \pi/16$ is the surface area ratio of the area occupied by vapor jets to the total surface area. The most dangerous wavelength, also referred as disturbance wavelength, is given as $\lambda_D = \sqrt{3}\lambda_c = 2\pi\sqrt{3\sigma/(\rho_l - \rho_v)g}$. The final expression of the Zuber's model is as follows

$$\frac{q''_{CHF,Z}}{\rho_g^{1/2} h_{fg} [\sigma g (\rho_f - \rho_g)]^{1/4}} = K = 0.131 \quad (3.2)$$

Many studies tried to improve the Zuber's CHF model by considering different parameters including surface wettability and surface roughness (effect of nucleation site). For a horizontal upward-facing orientation smooth plate, Lienhard and Dhir [101] proposed a correlation with $K = 0.149$. Kandlikar [102] proposed

$$K = \frac{1 + \cos \theta}{16} \sqrt{\frac{2}{\pi} + \frac{\pi}{4} (1 + \cos \theta) \cos \alpha}$$

for a surface with the contact angles $0 < \theta < 90$

and surface inclination angle α . The effect of surface roughness and nucleation site density is a subject of controversy in the literature [27]. Kim et al. [103] proposed

$$K = 0.811 \frac{1 + \cos \theta}{16} \sqrt{\frac{2}{\pi} + \frac{\pi}{4} (1 + \cos \theta) + \frac{351.2 \cos \theta}{1 + \cos \theta} \left(\frac{R_a}{S_m} \right)}$$

to consider the effect of surface roughness on CHF, where S_m is the mean spacing between roughness peaks.

There are studies in the literature, which report that thin walls can interfere with the CHF mechanism, resulting in CHF values smaller than those of thick walls. As the wall thickness increases, CHF values reach an asymptotic value above a threshold. Golobič, and Bergles [104] proposed the following correlation:

$$\frac{q''_{CHF}}{q''_{CHF,asy}} = 1 - \exp \left[- \left(\frac{S}{2.44} \right)^{0.8498} - \left(\frac{S}{2.44} \right)^{0.0581} \right] \quad (3.3)$$

where $q''_{CHF,asy}$ is the asymptotic CHF, and $S = H \sqrt{(\rho c_p k)_{\text{wall}}}$ is the “thermal conductivity” parameter. It should be noted that under the experimental conditions the

critical wavelength is equal to $\lambda_c \approx 1.5 \text{ cm}$, the most dangerous wavelength is equal to $\lambda_D \approx 2.7 \text{ cm}$, and the “thermal conductivity” parameter is $S \approx 0.17$.

Dry-out model: According to the dry out model (Figure 3.10b), the growth of large bubble is a result of macrolayer evaporation, and CHF occurs when the liquid macrolayer dries out just before the departure of large bubble[100]:

$$q''_{CHF} = \rho_f h_{fg} \delta (1 - A_g/A_w) f \quad (3.4)$$

Here, δ and f are macrolayer thickness and bubble departure frequency, respectively. There are several correlations for macrolayer thickness calculation. Rajvanshi et al. [105] recommended $\delta = 0.0107 \sigma \rho_g (\rho_g/\rho_f)^{2/5} (h_{fg}/q'')^2$ for density ratios of $\rho_g/\rho_f \ll 1$. Based on the lateral bubble coalescence mechanism, Kumada and Sakashita [106] developed a semi-empirical correlation of $\delta = 0.786 \left[v_g^8 \sigma^{11} / \rho_f^6 g^5 (\rho_f - \rho_g)^5 \right] (\rho_g h_{fg} / q'')^{5/6}$.

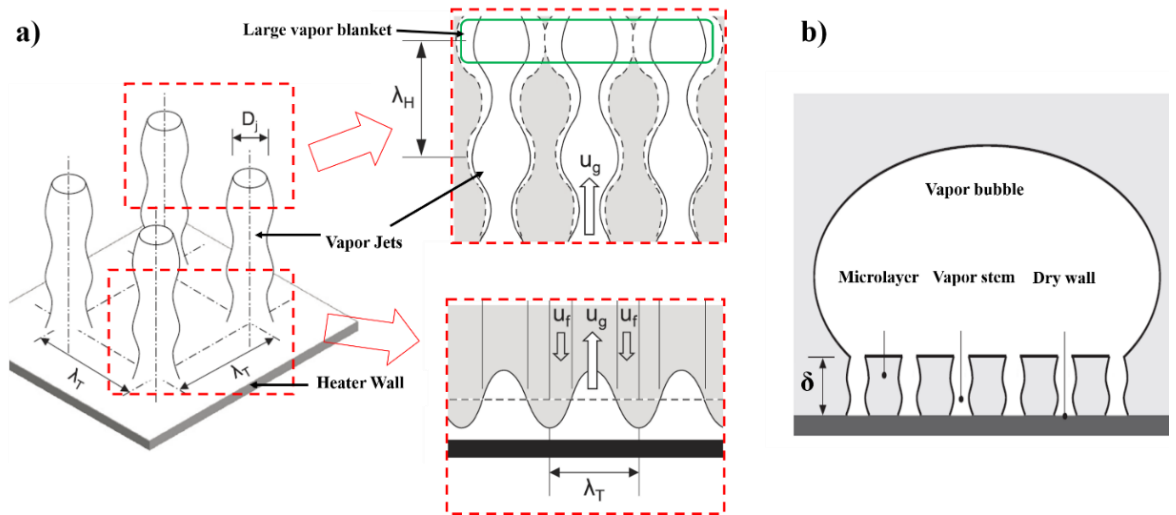


Figure 3.10 CHF mechanism according to the Zuber's hydrodynamic instability theory and the Haramura and Katto's macrolayer dry-out model. Adapted version from Liang and Mudawar [27]

Figure 3.11a shows the obtained CHF enhancements on the tested samples relative to untreated silicon surfaces. As can be seen, CHF enhancements are obtained for all of the fabricated samples. CHF values increase as the hole diameter decreases, and the effect of pitch size on CHF is dependent on the surface wettability. The increase in pitch size

enhances CHF on hydrophobic surfaces, while the opposite is valid for the hydrophilic surfaces. According to the visual results, hydrodynamic instability is the main reason for CHF on hydrophilic surfaces, while critical heat flux on hydrophobic surfaces is associated with the dry-out mechanism.

The effect of hole diameter and pitch size on CHF corresponding to hydrophilic surfaces can be explained by the hydrodynamic model based on Helmholtz instability. According to this model, at high wall heat fluxes, the velocity difference between liquid and vapor jets interface causes Helmholtz instability. With the growth of this instability, neighboring vapor jets form larger vapor columns (shown in Figure 3.10a). As can be seen in Figure 3.11b, the tested samples have the square geometry with length of 1.5 cm and diagonal of 2.12 cm. As a result, the CHF instabilities at the interface of large vapor blankets tend to happen in the diagonal direction of the samples. It appears that the shape of the large vapor bubbles before coalescence and departure depends on the hole pitch size. As the pitch size increases, the number of feeding jets beneath the large bubble increases. The feeding jets disturb the interface wavelength and delay the occurrence of CHF condition. This is indicated with red arrows in Figure 3.11b. Accordingly, the pitch size decreases CHF values on the hydrophilic structured surfaces. The hole pitch size can also be interpreted as the distance between roughness peaks, which is in parallel with the correlation proposed by Kim et al. [103] considering the distance between roughness peaks.

Unlike the hydrophilic samples, CHF condition on hydrophobic structured surfaces is due to dry-out beneath the vapor layer (macrolayer). As can be observed in Figure 3.11c, one large vapor bubble forms on top of the macrolayer fed by several vapor jets, which is shown with blue arrows. Hydrophobic nature of the surfaces reduces wetting at the solid/fluid interface. Lower surface energy enhances the bubble nucleation and departure on the superheated surface. As the number of generated vapor jets increases (as hole diameter decreases), surface re-wetting becomes difficult. As the hole pitch size increases, vapor jet coalescence beneath the macrolayer decreases, which enhances the rewetting of the superheated surface. In contrast to the hydrophilic surfaces, the pitch size enhances CHF on the hydrophobic samples. As indicated in Figure 3.4b, bubbles tend to spread on the hydrophobic surfaces. Larger pitch sizes force bubbles to coalesce in the vertical direction and to increase the macrolayer thickness, which enhances the

rewetting mechanism on the hydrophobic structured surfaces. This is also in agreement with the recommended correlation by Haramura and Katto [100].

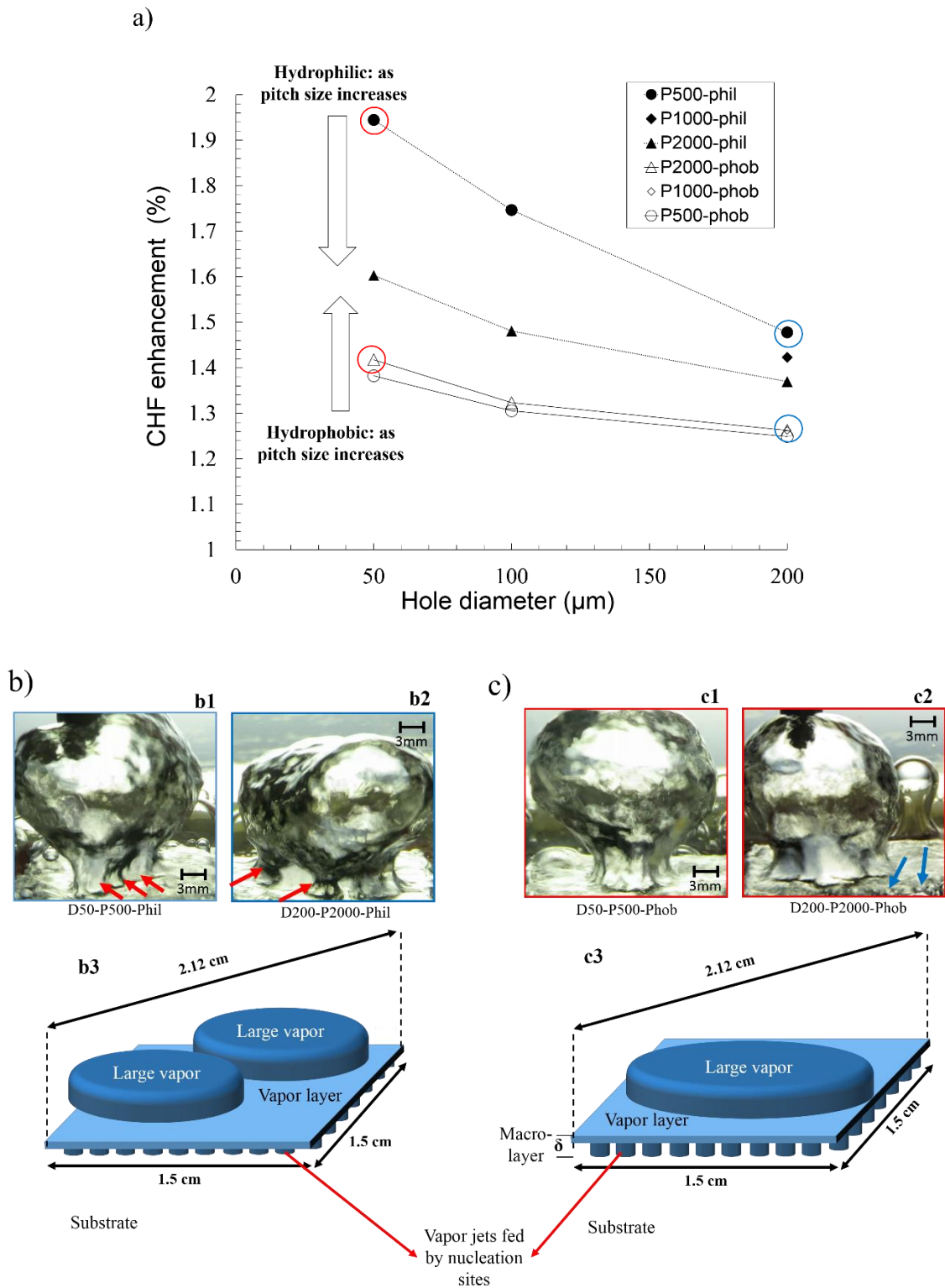


Figure 3.11 a) CHF enhancement on the tested surfaces relative to the bare silicon surface b) visual results under the CHF condition and their schematic

3.4 Conclusions

The effects of hole pitch size/diameter, as a critical parameter for bubble coalescence, on boiling heat transfer (BHT) and critical heat flux (CHF) of 14 different structured surfaces with different wettability were investigated. A parametric study was performed to study bubble departure diameter, bubble departure frequency, bubble coalescence, and critical heat flux mechanism on the fabricated samples. Circular cavities with depth of 32 μm , diameters of 50, 100 and 200 μm , and pitch sizes of 500, 1000, and 2000 μm were formed on silicon surfaces. Furthermore, the effect of surface wettability on the performance of the structured surfaces was also examined. The major conclusions are as follows:

1. Relative to bare silicon surfaces, the structured surfaces enhance heat transfer and critical heat flux. Maximum heat transfer enhancements of 100% (from hydrophobic structured surfaces at the wall heat flux of 30 W/cm²) and 30% (from hydrophilic structured surface at the wall heat flux of 50 W/cm²) were achieved. Maximum increases in CHF is 100% and 48% for the hydrophilic and hydrophobic tested surfaces, respectively. Such a striking difference between flat and structured surfaces is likely due to the nucleation and growth energetics and kinetics of the liquid-to-vapor transition and the associated critical bubble radius. Coalescence of bubbles on or above the surface is another factor influencing the mode of heat transfer from the hot walls.

2. Different bubble coalescence types were observed on tested samples. Vertical bubble coalescence was majorly observed on hydrophilic surfaces, while horizontal bubble merging was the main type of coalescence on generated bubbles on hydrophobic surfaces. It was found that there exists a critical hole pitch size/hole diameter ratio that initiates the horizontal bubble coalescence on tested samples. Three types of bubble coalescence were observed on the hydrophilic surfaces: vertical, horizontal and vertical-horizontal, while major coalescence occurs in the horizontal direction on the hydrophobic surface.

3. The obtained results imply that although the increase in hole diameter enhances CHF for all the fabricated samples, the effect of pitch size depends on surface wettability such that CHF increases and decreases with pitch size on the hydrophobic

and hydrophilic surfaces, respectively. The results showed that CHF occurrence on the hydrophilic surfaces is mainly due to hydrodynamic instability, while dry-out is the dominant CHF mechanism on the hydrophobic surfaces.

4. Biphilic surfaces

4.1 Introduction

The effect of surface biphilicity on boiling heat transfer and critical heat flux is presented in this chapter. Surfaces with mixed wettability (biphilic) were fabricated using MEMS technology for assessing the effect of biphilic surfaces on bubble dynamics and boiling heat transfer as well as for the determination of an optimum hydrophobic area to the total surface area ($A^* = A_{\text{Hydrophobic}}/A_{\text{Hydrophilic}}$) to achieve the best heat transfer performance. Superhydrophobic surfaces with diameters ranging from 50 to 1100 μm and constant pitch size of 1 mm were fabricated on hydrophilic silicon surfaces with contact angle of 20° . The superhydrophobic surfaces were fabricated by etching the silicon surfaces to form nano-grasses with contact angle of 165° . Pool boiling experiments were conducted on biphilic surfaces with A^* ranging from 0.0019 to 13. Boiling heat transfer, critical heat flux and bubble dynamics characteristics were observed by using a high-speed camera and parametric results, the effects of surface wettability on nucleation site interactions and critical heat flux were discussed in detail.

4.2 Sample preparation and characterization

Biphilic surfaces were fabricated by patterning the superhydrophobic circular islands surrounded by silicon dioxide hydrophilic areas. Each sample contains 100 superhydrophobic circular dots. The distance between centers of these circles (pitch size) was kept constant for all fabricated samples as 1mm. The diameter of the superhydrophobic areas was increased step-wise from 50 μm to 1100 μm , where eventually form a totally superhydrophobic surface. Figure 4.1 shows the configuration of biphilic surfaces with superhydrophobic circles of diameter D , pitch sizes of 1mm, and edge-to-edge spacing of S .

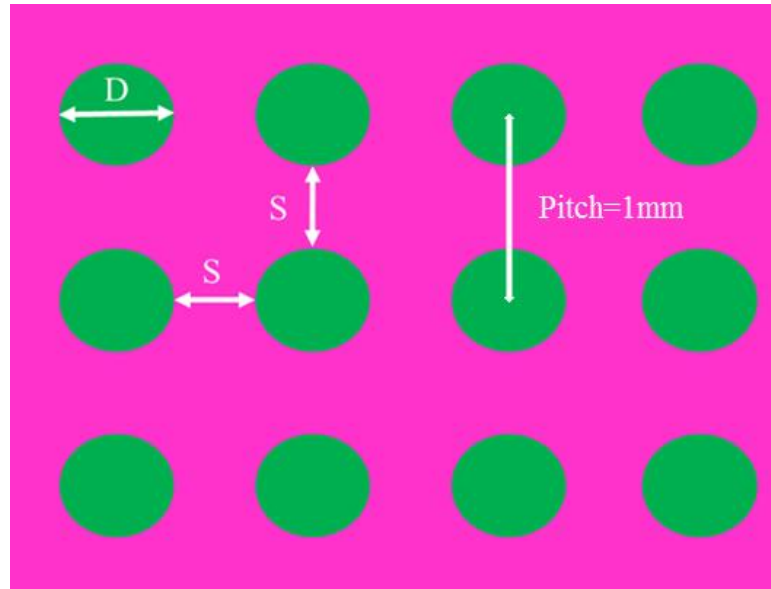


Figure 4.1 Configuration of biphilic samples

To fabricate biphilic surfaces, deep reactive ion etching (DRIE) and silicon oxide thin films have been used for hydrophobic and hydrophilic areas, respectively. One hundred hydrophobic islands (10×10) were surrounded by silicon oxide on 1.3×1.3 cm² silicon samples. Hydrophobic islands were enlarged step by step to a wholly hydrophobic surface. Boiling curves were obtained for all the biphilic surfaces. To analyze bubble dynamics, a high-speed camera system was used to record bubble nucleation and bubble motion during pool boiling. Table 4-1 summarizes the samples properties.

Table 4-1 Physical properties of fabricated samples

Sample No	Hydrophobic Diameter (D) (μm)	Edge to edge spacing (S) (μm)	$A_{\text{Hydrophobic}}/A_{\text{Hydrophilic}} (A^*)$
#1	50	950	0.0019
#2	150	850	0.0179
#3	300	700	0.0759
#4	400	600	0.1436
#5	500	500	0.2441
#6	700	300	0.6249
#7	800	200	1.0096
#8	900	100	1.7457
#9	1000	-	3.6511
#10	1100	-	13

SiO ₂ Coated Sample	Totally Hydrophilic
Nano-grass Sample	Totally Hydrophobic

All the samples were fabricated on 100mm silicon wafers. A schematic of microfabrication process can be seen in Figure 4.2.

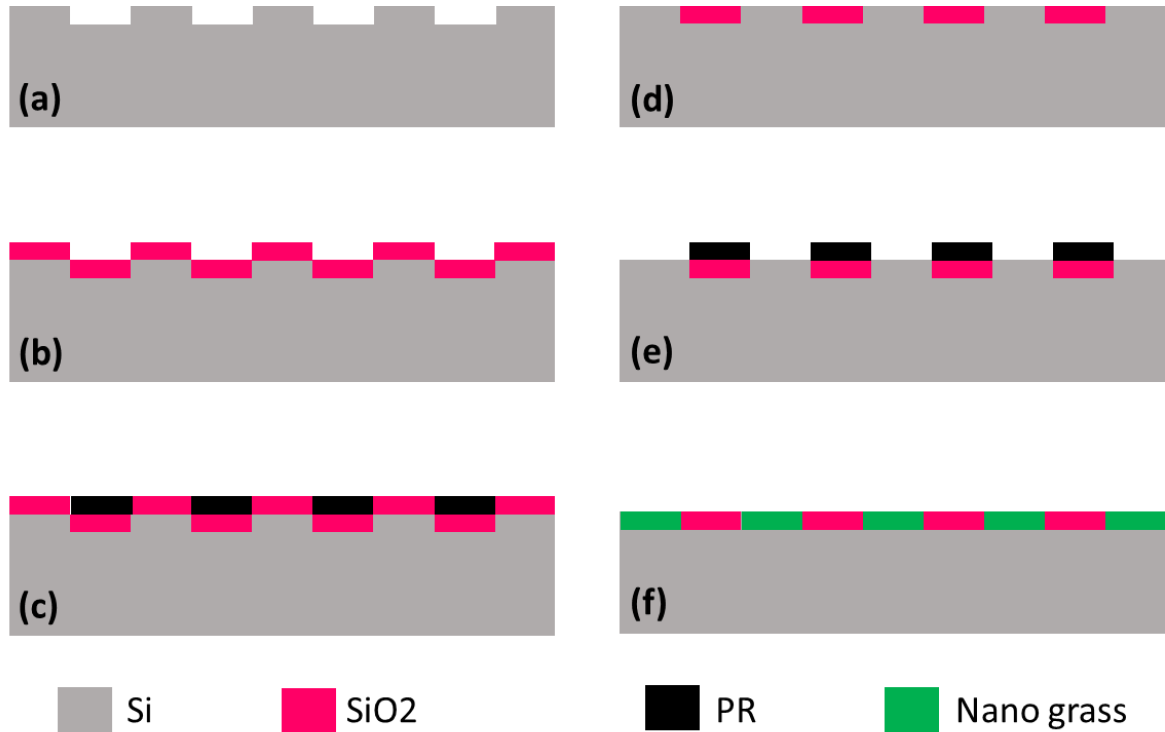


Figure 4.2 Fabrication of biphilic surfaces. a) 1 μm deep anisotropic silicon etch using photoresist as etch mask. b) Thermal growth of 1 μm silicon dioxide. c) Photolithography – oxide etching mask. d) Dry etching of silicon dioxide. e) Photolithography – silicon etching mask. f) Formation of nano grass using deep reactive ion etching

Firstly, to prevent any height difference between hydrophilic and hydrophobic areas, the substrate of hydrophilic network was etched for 1 μm . A patterned 2 μm thick photoresist (AZ-ECI) was used as an etch mask to protect the areas, which would become hydrophobic islands. A 1 μm -thick layer of SiO₂ (hydrophilic material) was grown on the Si substrate using wet thermal oxidation (Figure 4.2b). Afterwards, a patterned 2 μm thick layer of photoresist was used to protect SiO₂ hydrophilic network during silicon dioxide dry etching (Figure 4.2c).

After etching SiO₂ and removing photoresist (Figure 4.2d), the third patterned layer of photoresist was used as an etch mask to protect hydrophilic areas during the fabrication

of hydrophobic spots via deep reactive ion etching (Figure 4.2e). In the last step, the black silicon method [107] was used to fabricate nano-grass on the silicon substrate. Although there are several studies on the fabrication of needle-shaped structure in the literature [108, 109], the given information and recipe for a specific process cannot be directly used in other laboratories. This issue results from the difference of the etcher configuration, chamber geometry, and flow handling of various etching equipment [107]. The formation of nano-grass structures is sharply dependent on etching parameters such as gas flows and chuck temperature [110]. Here, our idea is to use SF₆ and C₄H₈ gas flows with manipulating pulse time of SF₆ to affect the etching process. The pulse time of SF₆ varies from 3 to 4 seconds with various chuck temperatures ranging from 30°C to 0°C. The process parameters of the 5 tested different recipes can be seen in Table 4-2.

Table 4-2 Nano-grass etching parameters. 5 different etch recipes were tested. The gas flows of SF₆ and C₄H₈ were fixed at 300 sccm and 150 sccm, respectively. The SF₆ pulse time was either 3 or 4 seconds and the C₄H₈ pulse time was fixed at 2 seconds. The chuck temperature varied between 0°C and 30°C. The etch time was 3 min in all the cases

Recipe name	SF ₆ (sccm)	Pulse time (s)	C ₄ H ₈ (sccm)	Pulse time (s)	Chuck temperature (°C)	Etch time (min)
N-G #1	300	3	150	2	30	3
N-G #2	300	4	150	2	30	3
N-G #3	300	3	150	2	10	3
N-G #4	300	4	150	2	10	3
N-G #5	300	3	150	2	0	3

After the etching process, to check the quality of samples, all were inspected by eye. Recipes N-G #1 and N-G #4 were eliminated due to the low quality of etching. Figure 6 shows Scanning Electron Microscope (SEM) images of the fabricated samples using N-G#2, N-G#3 and N-G#5. The formation of nano grass was poor when N-G#2 recipe was used.

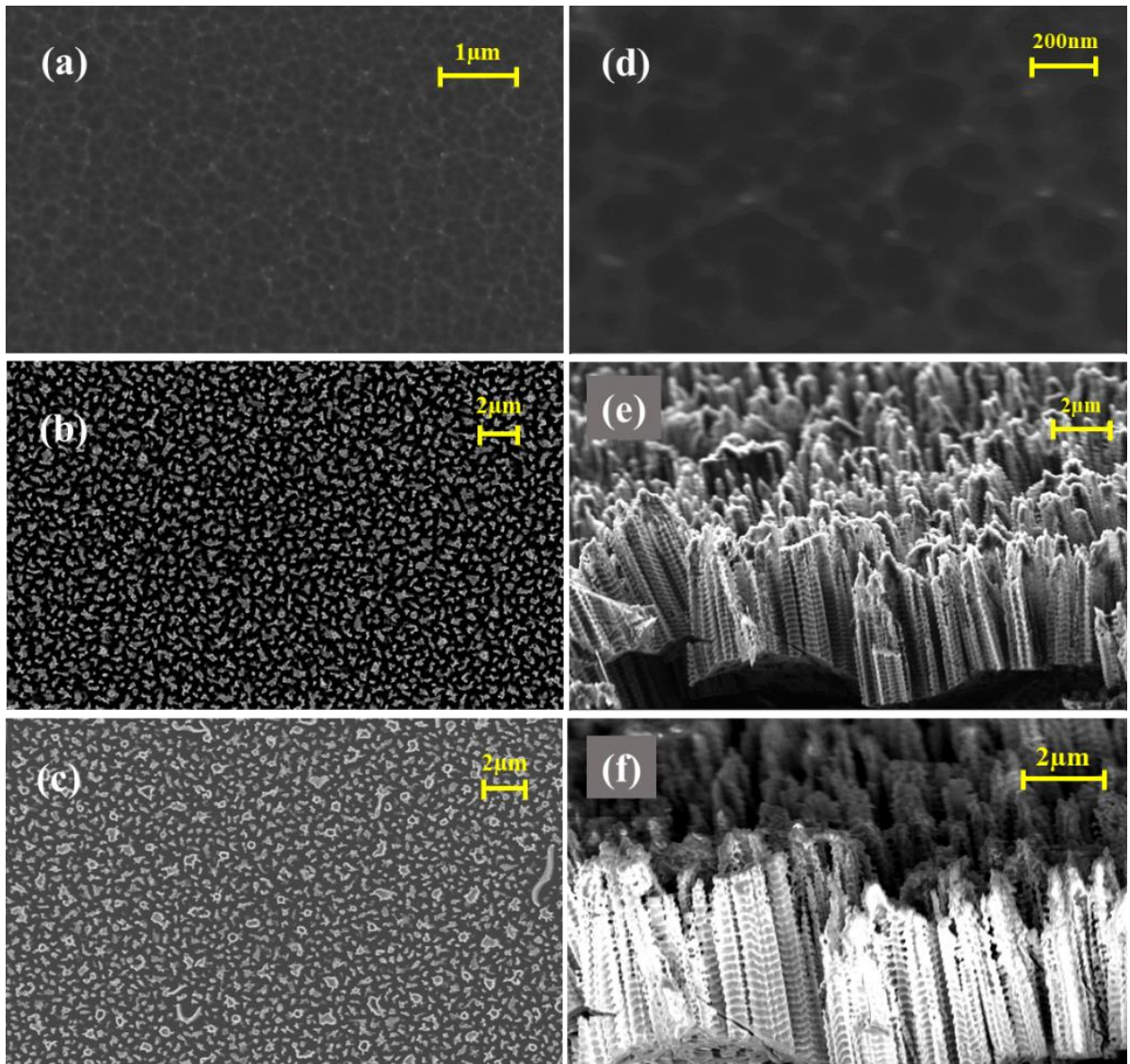


Figure 4.3 SEM images related to top view of recipe (a) N-G #2 (b) N-G #3 (c) N-G #5 and lateral view of (d) N-G #2 (e) N-G #3 (f) N-G #5. The etching time for all the recipe is 3 minutes. b) and e) show the top and lateral view of N-G #3 which is used in the biphilic samples.

The SEM images of fabricated samples are shown in Figure 7. As can be seen, hydrophobic islands gradually enlarge step by step so that it becomes possible to offer an optimum morphology for boiling heat transfer.

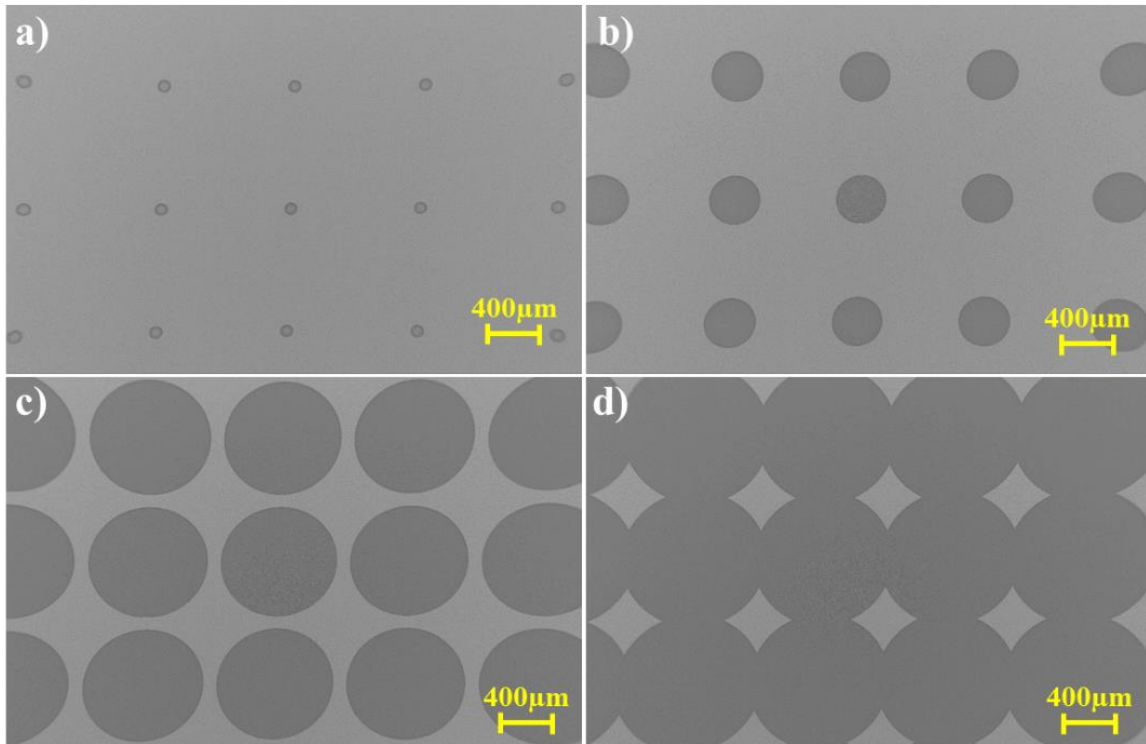


Figure 4.4 SEM images of fabricated samples with hydrophobic circular areas with a) 50 μm diameter b) 300 μm diameter c) 800 μm diameter d) 1000 μm diameter

The surface morphology of nano-grass and mixed hydrophilic and hydrophobic samples was obtained via Scanning Electron Microscopy (SEM, Z15-Zeiss-Merlin). With the use of scanning probe microscopy (SPM) methods, the topographical imaging of surfaces is extensively available. The characterization of surface structures such as topographical shape and characteristics can be analyzed with the SPM method. The enhanced surfaces were characterized by Atomic Force Microscopy (AFM) in dynamic mode (ezAFM, Nanomagnetics Instruments). 2-D and 3-D AFM results are presented in Figures 8 (a) and (b). The wettability of enhanced surfaces was tested by the WCA (Water Contact Angle) method by ThetaLite Tensiometer (Dyne Technology). The Sessile drop method was used to measure the CA (contact angle) by dispensing a 5 μL water drop. Contact angles of 20° and 165° were measured for hydrophilic and hydrophobic parts, respectively.

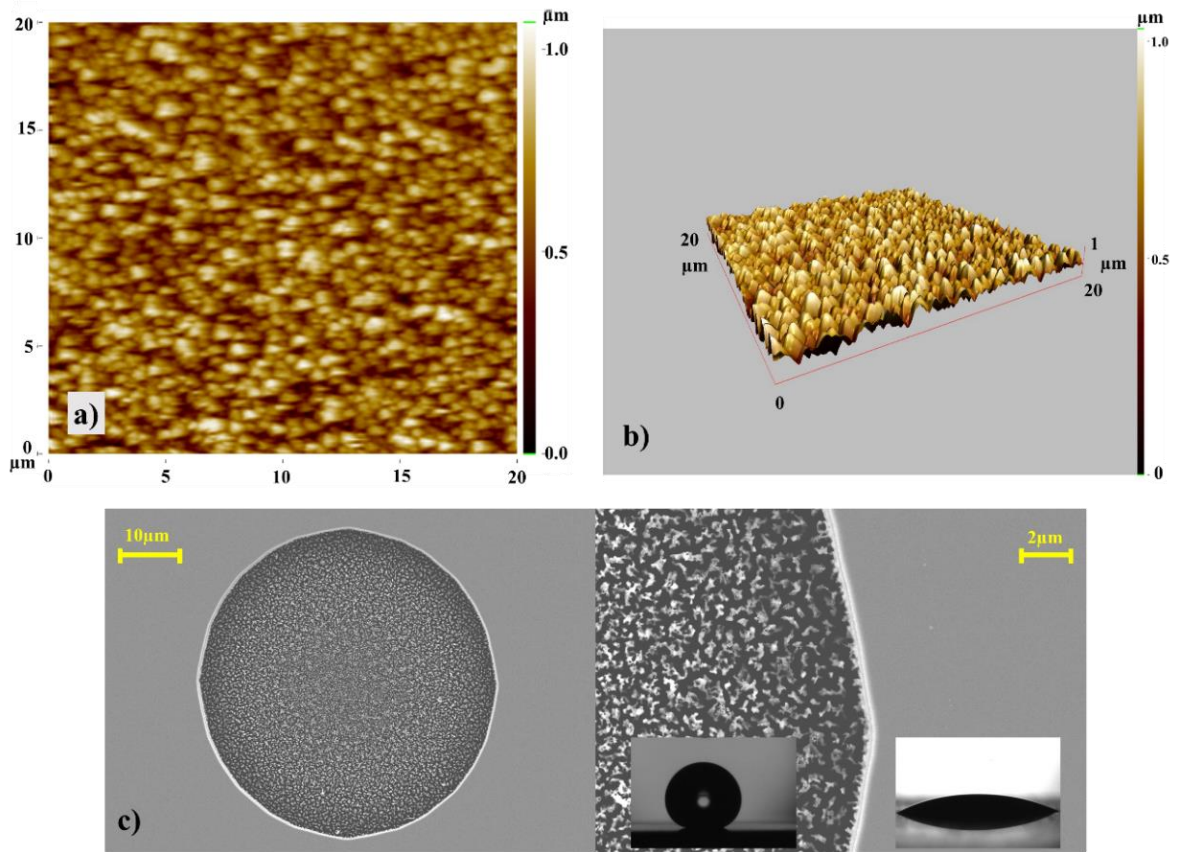


Figure 4.5 Surface characterization of biphilic samples. Samples were characterized using Atomic Force Microscopy (AFM) and contact angle measurement techniques. a) 2-D b) 3-D AFM results showing the size and shape of hydrophobic structures. c) Contact angle measurement on both hydrophilic (20°) and hydrophobic (165°) areas

4.3 Results and Discussions

4.3.1 Bubble nucleation and growth

Bubble nucleation and growth on biphilic surfaces dramatically depends on the size, and edge-to-edge spacing of the superhydrophobic islands. Surfaces with mixed wettabilities were examined to find the optimum ratio of surface areas in term of heat transfer performance. Surfaces with total hydrophilic and total superhydrophobic areas were tested prior to examining the biphilic surfaces as the reference studies. Boiling hysteresis in nucleate boiling strongly depends on the experimental conditions and surface-working fluid combination. In this study the boiling experiments were conducted by stepwise increasing the applied heat flux. According to the obtained results no hysteresis was observed. The absence of significant boiling inception hysteresis and

temperature shoot during the performed experiments is mainly due to the surface temperature measurement procedure. As stated in the data reduction section (APPENDIX 2), the surface temperature was calculated by averaging the temperatures at three locations beneath the tested samples. It should be noted that in this study, the experiments were performed under steady state conditions, which further reduces the temperature overshoot in the nucleate boiling regime. Furthermore, the experiments were performed in a clean environment to prevent any contamination on the heating surface.

Surfaces with low surface energy are not easily wetted by boiling liquid. Lower surface energy of superhydrophobic spots facilitates bubble nucleation. As a result boiling inception takes place at lower wall superheats on superhydrophobic dots compared to hydrophilic areas, as shown in Figure 4.6. According to heterogeneous nucleation model, there exists two theories describing the mechanism of vapor bubbles generation from trapped vapor/gas in the surface cavities. From thermodynamic point of view, by assuming that the filled gas in the cavity achieves minimum Helmholtz free energy at the liquid-gas interface, Wang and Dhir [56] suggested a vapor/gas trapping criteria. In this model it is suggested that gas/vapor phase will be confined if the $\theta > \Psi_{\min}$ condition satisfies. Here, θ and Ψ_{\min} are surface contact angle and minimum cavity side angle as shown in Figure 4.6a. Bankoff [111] proposed a model for vapor trapping by considering the liquid displacement in the cavity. Accordingly this model stated that the vapor will be trapped when $\theta > 2\beta$, where θ and β are contact angle and half cone angle as shown in Figure 4.6b.

Since superhydrophobic spots satisfy the abovementioned criteria's, the trapped vapor/gas in the cavities initiate boiling inception on the islands. The visualization results indicated that bubbles tend to nucleate and grow at the contact line separating surfaces with different wettabilities. The surface tension gradient on this contact line exerts a non-uniform force on nucleated bubble, and small pinning force acting on the superhydrophobic area stimulates the bubble departure processes.

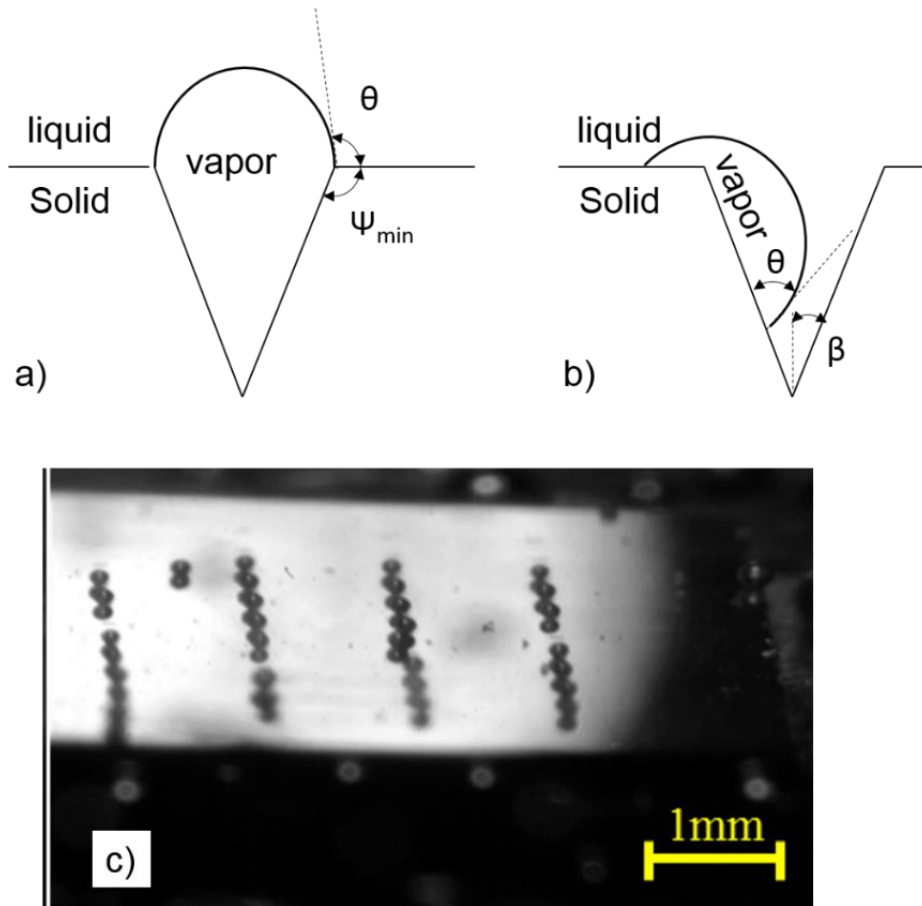


Figure 4.6 a) vapor/gas trapping in surface cavities according to Wang and Dhir model b) vapor/gas trapping in surface cavities according to Bankoff model c) Bubble nucleation on superhydrophobic islands

All of the biphilic surfaces enhance boiling heat transfer by promoting onset of nucleate boiling (ONB). The effect of low surface energy spots on boiling heat transfer is more pronounced at moderate wall superheats regimes where isolated bubbles exist. The major difference between tested biphilic surfaces is the ratio between superhydrophobic to hydrophilic areas. The distance and size of the islands change bubble dynamics, and bubble coalescence process. The obtained results indicated that the size of the generated bubbles at isolated nucleate boiling regime changes with diameter of superhydrophobic islands, such that size of the nucleated bubble increases with diameter up to a certain island diameter. After this diameter although the bubble diameter (D_b) does not change with the island diameter (D), the reduced edge-to-edge spacings (S) contribute to bubble coalescence and departure process. Figure 4.7 compares the nucleated bubbles on samples NO#1 ($D=50\mu\text{m}$ and $S=950\mu\text{m}$) and NO#8 ($D=900\mu\text{m}$ and $S=100\mu\text{m}$). As can be seen, while the generated bubbles on sample NO#1 are smaller than those nucleated from

sample No#8, the number of merged bubbles on sample NO#8 are much more than the other sample.

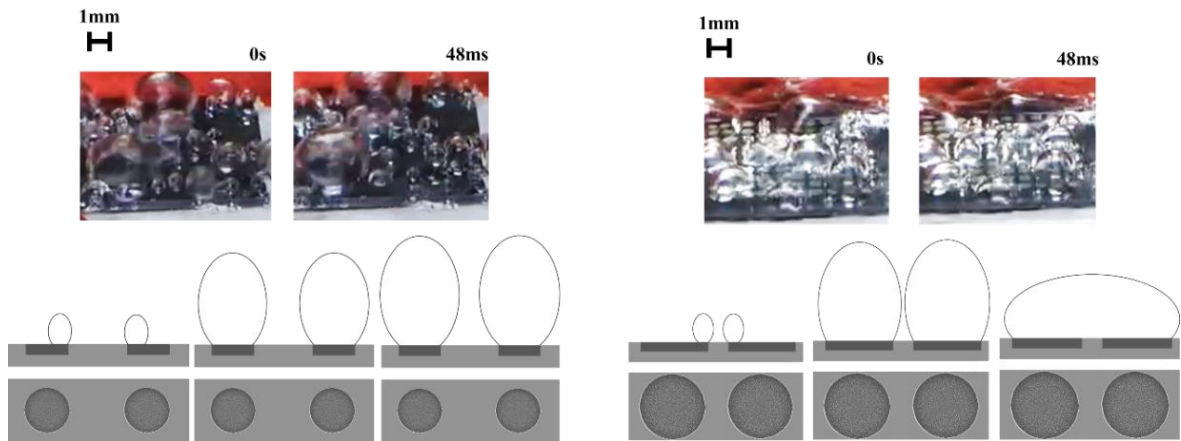


Figure 4.7 Bubble size during the nucleation and coalescence process on a) sample NO#1 ($D=50\mu\text{m}$ and $S=950\mu\text{m}$) and b) and sample NO#8 ($D=900\mu\text{m}$ and $S=100\mu\text{m}$)

At a fixed thermal boundary condition, surface tension and buoyancy forces are major forces acting on the bubble during growth and departure periods. Compared to untreated surface (totally hydrophilic), generated bubbles on superhydrophobic areas of biphilic surfaces exert much smaller surface tension force on growing bubble, and facilitate departure process by reducing the growing time. Furthermore, bubble coalescence on superhydrophobic islands not only increase the size of the growing bubble (larger buoyancy force), the remaining vapor residual on nucleation site decrease the waiting time and shorten the bubble nucleation, growth and departure process (Figure 4.8).



Figure 4.8 Bubble merging on the sample NO#6

4.3.2 Boiling heat transfer

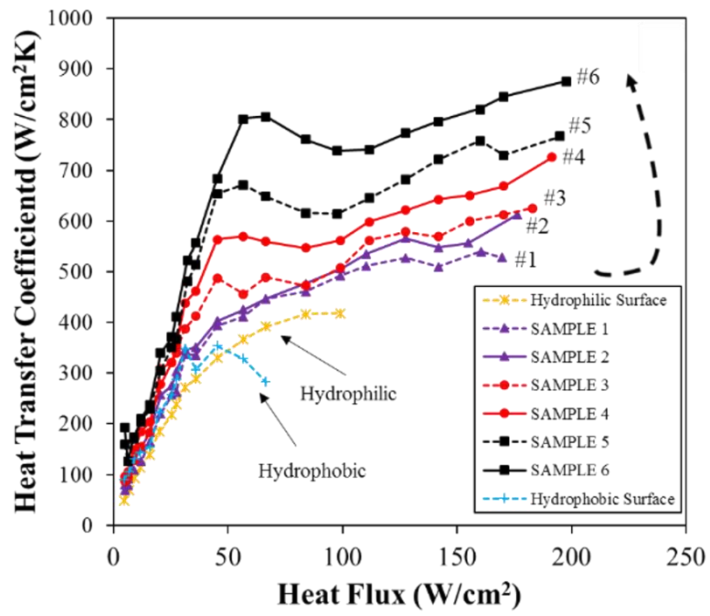
Aside from the A^* ($A_{\text{hydrophobic}}/A_{\text{hydrophilic}}$) ratio, all of the biphilic samples enhance boiling heat transfer compared to the wholly hydrophilic and totally superhydrophobic

surfaces. According to the obtained results shown in Figure 4.9, heat transfer coefficient trends increase with superhydrophobic area up to $A^* \approx 0.62$. Beyond this ratio, a decreasing trend can be witnessed for HTC. For the samples with ratios higher than optimum ratio ($A^* \approx 0.62$), an increasing ($q'' < 50 \text{ W/cm}^2$) and decreasing ($q'' > 50 \text{ W/cm}^2$) trends can be observed. The main reason for this behavior can be discussed based on bubble dynamics and surface temperature on these surfaces.

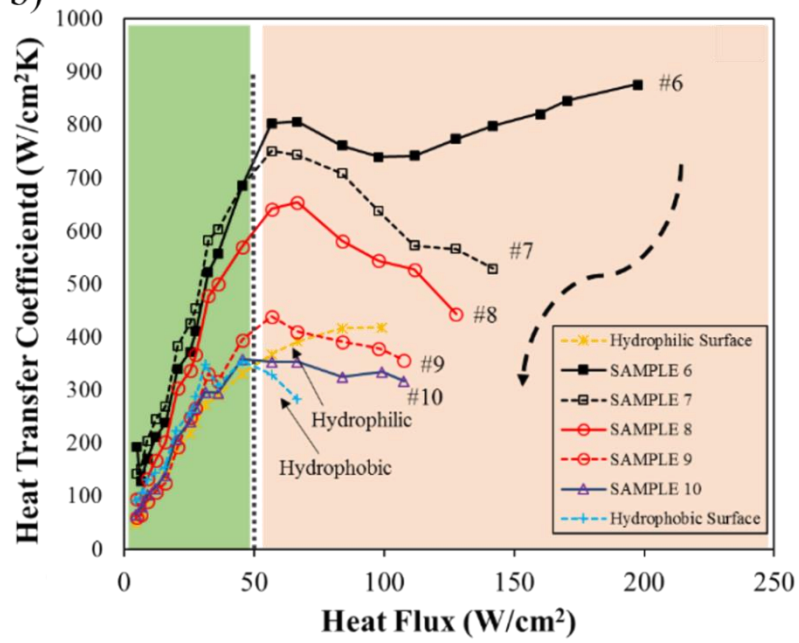
In addition to the presented data in the previous section (4.3.1), bubble dynamics during the coalescence process also contribute to the heat transfer mechanism beneath the growing bubble. It is believed that the microlayer evaporation and transient conduction are main mechanisms responsible for boiling heat transfer at low wall superheats. As the generated bubble move away from the nucleation site, it pushes away the surrounding hot liquid layer and increase the conduction heat transfer near the activated nucleation site. During the bubble coalescence, the liquid film between two bubbles can be evaporated or transported to the nearest nucleation site and contribute to the boiling heat transfer.

If a very fast coalescence process – following by an immediate nucleation – takes place during the bubble merging, the liquid layer between merging bubbles could be pushed away. Very rapid bubble merging takes place on samples with large D/S ratios such as NO#7 and NO#8. The high velocity of approached bubbles disturbs the liquid layer and prevents liquid layer formation and evaporation between the bubbles. This means that there exists a ratio for mixed wettability on biphilic surfaces for optimum evaporation heat transfer. Furthermore, liquid flow path shrinkage by large amount of vapor columns flowing upward from the superheated surface could be another reason of heat transfer deterioration on these surfaces.

a)



b)



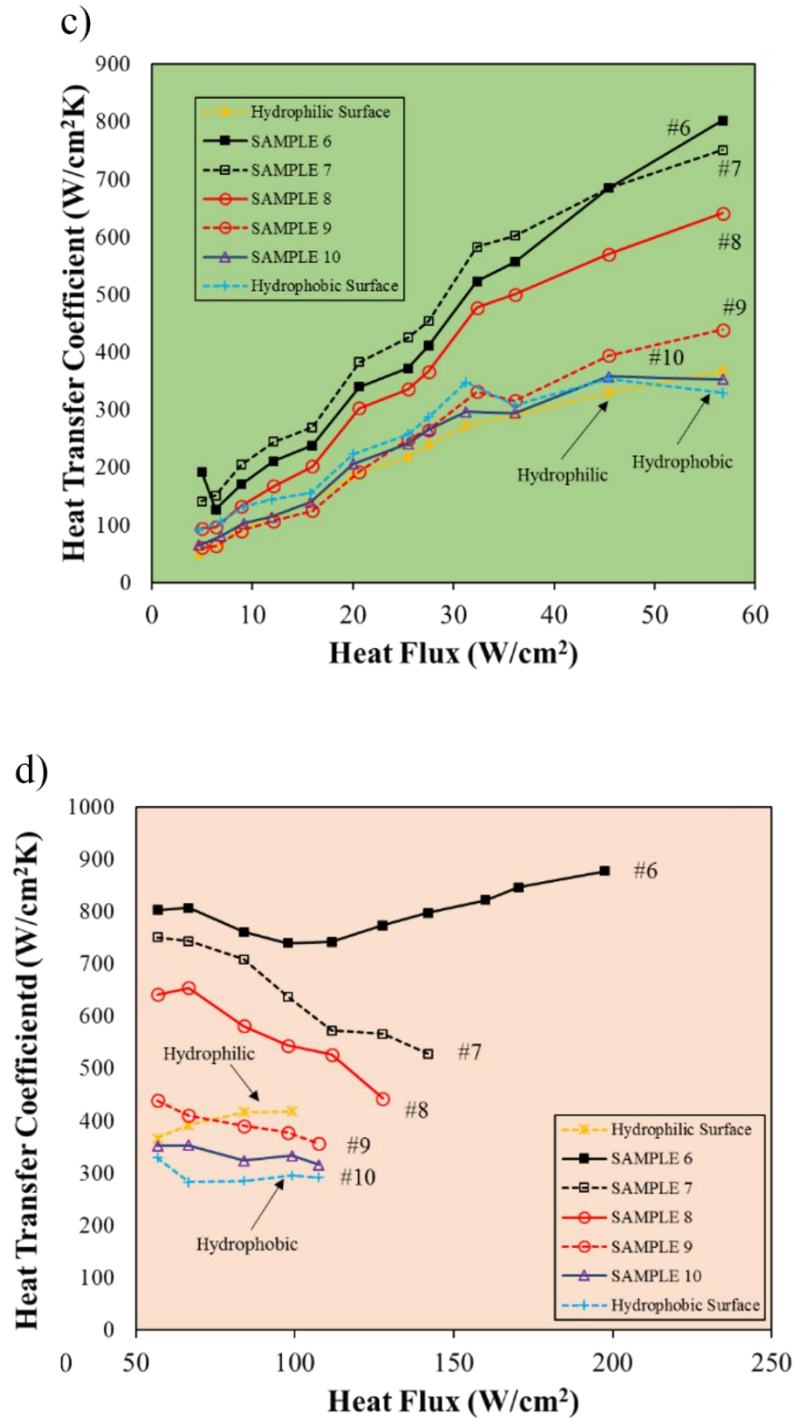


Figure 4.9 Obtained HTCs as a function of applied wall heat flux on a) samples No#1 to No#6 b) samples No#6 to No#10 c) data of samples No#6 to No#10 up to $q'' < 50$ W/cm² d) data of samples No#6 to No#10 from $q'' > 50$ W/cm²

Due to early ONB occurrence and more bubble coalescence, biphilic surfaces have promising heat transfer performance comparing to wholly hydrophilic surface at low wall heat fluxes. On the other hand, the complexity of bubble dynamics, i.e. bubble

coalescence and vapor jets at higher heat fluxes, biphilic surfaces demonstrate different heat transfer mechanisms, and eventually different cooling performance depending on the surface configuration. The observations are in parallel with the available results in the literature [93, 94].

The bubble departure diameter on biphilic surfaces are much smaller than those on the wholly hydrophilic and superhydrophobic surfaces. Smaller departure bubble size shortens the bubble departure period. Based on obtained visual results, bubble departure frequencies (bubble departure diameter) at moderate wall heat flux of 30 W/cm^2 on untreated and superhydrophobic surfaces were $\sim 6 \text{ Hz}$ ($\sim 4.1 \text{ mm}$) and $\sim 9 \text{ Hz}$ ($\sim 3 \text{ mm}$), respectively, while surfaces with $A^*=0.0179$ (No#2), $A^*=0.6249$ (No#6), $A^*=13$ (No#10) had frequencies of $\sim 19 \text{ Hz}$ ($\sim 2.9 \text{ mm}$), $\sim 56 \text{ Hz}$ (~ 0.9), and $\sim 25 \text{ Hz}$ ($\sim 2.5 \text{ mm}$), respectively. As stated before, the vapor residual on superhydrophobic islands leads to continuous nucleation, growth, and departure process with no waiting time, which enhances the bubble departure process by eliminating the bubble waiting time.

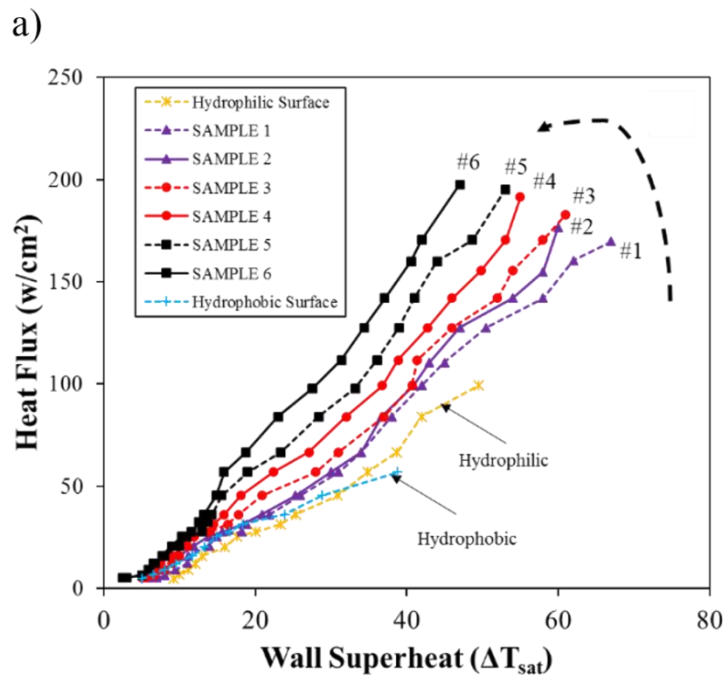
Accordingly to the results obtained from tested samples, it was found that the optimum ratio for hydrophobic/hydrophilic surface areas for maximum heat transfer enhancement is $A^* \approx 0.62$. Heat transfer coefficient enhancements on some of the tested samples at moderate wall superheats are shown in Table 4-3. As seen, promising heat transfer enhancements were achieved using the mixed wettability method.

Table 4-3 Obtained HTC enhancement at wall superheats of 10K, 15K, and 20K for samples No#1, No#6, No#7, No#10

Sample	A-star	HTC enhancement (%) $\Delta T=10\text{K}$	HTC enhancement (%) $\Delta T=15\text{K}$	HTC enhancement (%) $\Delta T=20\text{K}$
No#1	0.0019	58.7	58.6	40.6
No #6	0.6249	420.2	322	229.6
No#7	1.0096	558.6	326	210
No#10	13	48.4	42	19.3
Hydrophobic	0	110	55.1	33.5

4.3.3 Critical heat flux (CHF)

Figure 4.10 shows the boiling curves for the tested samples. The last point in the curves is considered as the thermal limit of the boiling, and the corresponding heat flux is called critical heat flux. The CHF point can be identified by severe temperature rise in wall temperature as well as vapor blockage on the superheated surface. Visualization studies confirmed the presence of a large vapor blanket on the boiling surface. CHF values of 98 W/cm^2 and 56 W/cm^2 were obtained on the wholly hydrophilic and superhydrophobic surfaces, respectively.



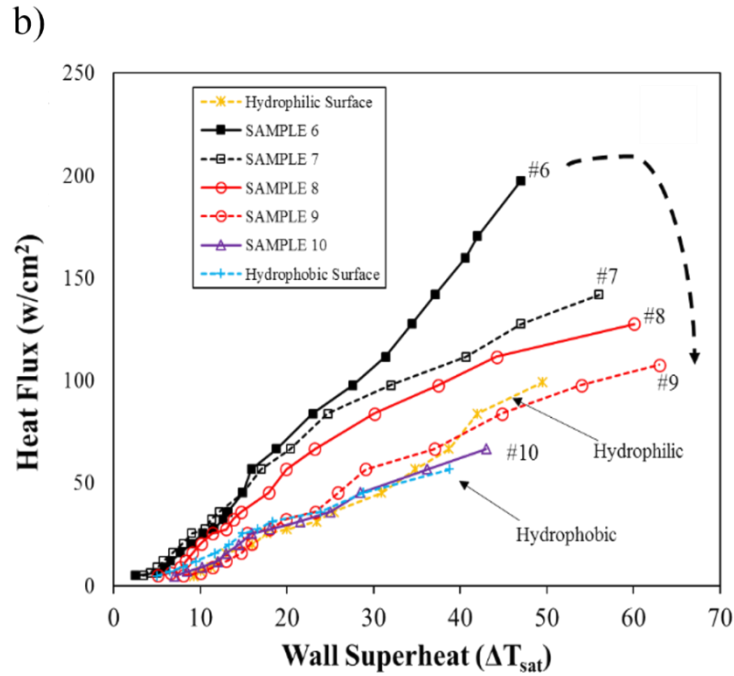


Figure 4.10 The boiling curves for tested samples

We found that the CHF values on tested samples demonstrate different augmentation/deterioration trends with surface area ratio. CHF values increase with surface area ratio up to sample NO#6 with $A^*=0.62$. As can be seen in Figure 4.11, the liquid path size (blue areas) decreases as the diameter of superhydrophobic islands increases (grey circles with diameter of D). The Helmholtz unstable jets (dashed area with area of D^2) completely block the liquid flow path and trigger the CHF condition. Accordingly, the obtained CHF values for samples NO#1, NO#2, NO#3, NO#4, NO#5, and NO#6 are 170 W/cm^2 , 176 W/cm^2 , 183 W/cm^2 , 191 W/cm^2 , 194 W/cm^2 , and 197 W/cm^2 , respectively. For samples with $A^*>0.62$, the liquid path is completely blocked by the vapor jet even before Helmholtz instability occurs at the liquid/vapor interface. In the absence of liquid replenishment flow, the CHF mechanism on these surfaces is due to irreversible dry spots on superheated surfaces. Choi et al. [112] proposed thermal and hydrodynamic conditions for this model. It was stated that this condition occurs when the number of spots is higher than a critical number, for which they start to reach to each other. On samples with $A^*>0.62$, as the distance between superhydrophobic islands decreases the grown dry-spots could merge. Furthermore, based on thermal criteria proposed by Choi et al., dry spots trigger CHF once the surface temperature reaches Leidenfrost temperature (134°C for water). According to the obtained results, the CHF

values on samples NO#7 to NO#9 correspond to much higher wall superheats. Consequently, it is probable that the dry-spot is the mechanism responsible for CHF occurrence on samples with $A^* > 0.62$. The CHF values for samples NO#7, NO#8, NO#9, and NO#10 are 142 W/cm^2 , 127 W/cm^2 , 107 W/cm^2 , and 66 W/cm^2 , respectively.

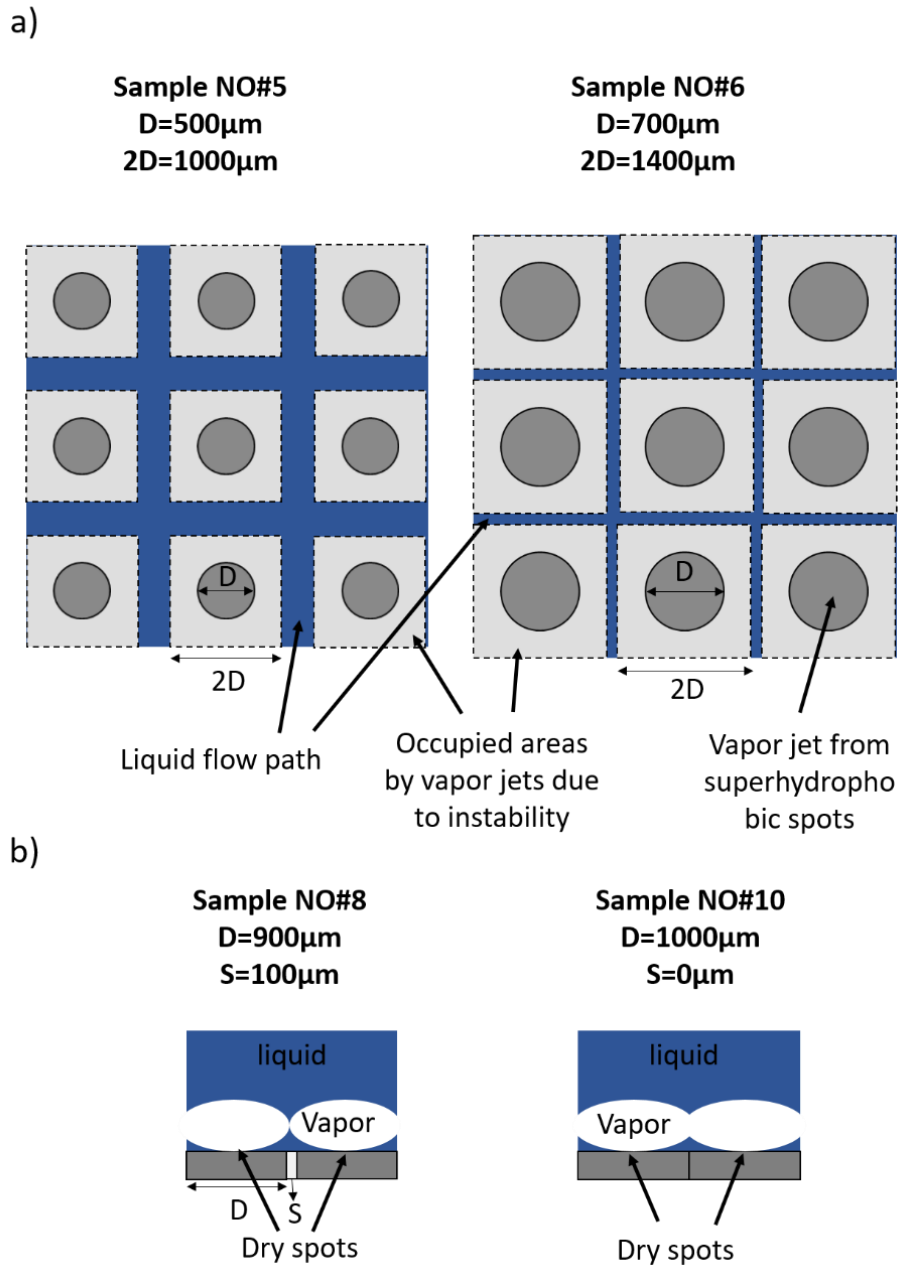


Figure 4.11 a) Unit cell containing vapor jets with diameter D and surrounding liquid b) dry spots on samples with high D/S ratios

This was also verified by the experimental results. The visualization studies not only revealed the presence of vapor residual on superhydrophobic surfaces after bubble departure (Figure 4.8), They also indicate that unlike superhydrophobic structured

surfaces, where bubbles tend to move on superhydrophobic surface areas, the hydrophilic boundaries among superhydrophobic areas prevent spreading the vapor phase along the superheated surface (Figure 4.12). The combination of superhydrophobic and hydrophilic surfaces enhances CHF. Superhydrophobic surfaces control the vapor spreading on the superheated surface and delay the Helmholtz instability in upward flowing vapor jets, while hydrophilic regions enhance surface rewetting and contribute to surface replenishment. These results are in parallel with the reported data in the literature [48, 94, 113]

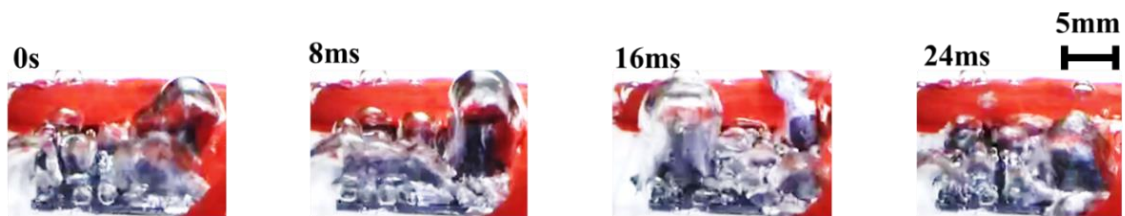


Figure 4.12 Vapor column behavior just before CHF condition (176 W/cm²) on biphilic SAMPLE #6

4.4 Conclusion

In this study, a novel and facile process flow for the fabrication of biphilic surfaces was proposed, and a parametric study was performed to find an optimum ratio of hydrophobic/total areas (A^*), for maximum pool boiling heat transfer and CHF enhancement. Ten biphilic surfaces with $A^* = A_{\text{Hydrophobic}}/A_{\text{Total}}$ ranging from 0.0019 to 13 were tested to assess the effect of heterogeneous wettability on boiling heat transfer. With the help of visualization studies, the enhancement mechanisms of biphilic surfaces were revealed. According to the experimental results, heat transfer coefficient and CHF increased with A^* up to 0.62. Surfaces with $A^* > 0.62$ demonstrated a decreasing trend in CHF and heat transfer coefficient enhancement, which is caused by earlier interaction of nucleated bubbles, thereby triggering the generation of vapor blanket at lower wall superheat temperatures. This ratio could serve as a valuable design guideline in the design and development of new generation thermal systems. The major conclusions are as follows:

1. Onset of nucleate boiling occurs at much lower wall superheats ($\Delta T_{\text{sup}} < 1$) on biphilic surfaces comparing to hydrophilic surfaces ($\Delta T_{\text{sup}} < 3$). Lower surface energy of

the superhydrophobic islands exert lower surface tension force on generated bubbles, thus smaller and movable bubbles form on the superhydrophobic areas. It was found that the size of nucleated bubble increases with island size up to a certain diameter.

2. The diameters and edge-to-edge distance between superhydrophobic islands affect bubble dynamics, and make major differences from those on wholly hydrophilic and superhydrophobic surfaces. It was found that $A^*=0.62$ is the optimum surface area ratio for maximum boiling heat transfer. One possible reason of heat transfer deterioration for surfaces with $A^*>0.62$ is rapid bubble merging during bubble coalescence, which pushing away liquid film between nucleated bubbles.

3. Biphilic surfaces also greatly enhanced CHF values comparing to wholly hydrophilic and superhydrophobic samples. Surface area ratio also changes CHF mechanism of biphilic surfaces. It was found that hydrodynamic instability is the main CHF mechanism on biphilic surfaces with $A^*\leq 0.62$, while formation of dry-spots is the surface dryout mechanism responsible for samples with larger superhydrophilic surface areas.

5. Polymer coating

5.1 Introduction

This chapter summarizes the pool boiling experiments conducted on thermo-responsive polyhydroxyethylmethacrylate (pHEMA) coated surfaces, to investigate the effect of coated surfaces on bubble nucleation and dynamics. pHEMA coated silicon surfaces with different thicknesses and surface orientations were tested in pool boiling experiments. Coatings with thicknesses of 50, 100, and 200 nm were deposited using the initiated chemical deposition (iCVD) method. Experiments were performed on horizontal and inclined surfaces (inclination angles of 10°, 30°, 50°, and 70°) under the constant heat flux (ranging from 10 to 80 kW/m²) boundary condition. Obtained results were compared to their plain surface counterparts. Boiling heat transfer and bubble dynamics characteristics were observed by using a high-speed camera and parametric results, the effects of coated surface orientation on nucleation site interactions and boiling heat transfer were discussed in detail.

5.2 Sample preparation and characterization

Initiated vapor deposition (iCVD) method was used for poly-2-hydroxyethyl methacrylate (pHEMA) deposition on silicon substrates. iCVD is a solventless technique used for depositing chain growth polymers on surfaces. This solvent free polymerization method increases homogeneity of the coatings and provides good thickness control [114]. Thin polymer films of pHEMA have poor mechanical properties. In order to improve the mechanical strength in this study, the cross-linker agent Ethylene glycol dimethylacrylate (EGDMA) is used, which is crucial for the films to withstand the environmental conditions (e.g. high heat fluxes). However, cross-linker ratio affects the swelling of the

pHEMA films, therefore, cross-linker ratio of the films needs to be optimized in order to achieve a balance between mechanical strength and swelling properties.

The monomer (HEMA) and cross-linker agent (EGDMA) are heated to 70°C and 85 °C, respectively in metal jars, outside the vacuum system. The vapors are then delivered into the system through ports. The temperature of the initiator, on the other hand is kept at room temperature. During deposition the pressure of the reactor is kept constant at 200 mTorr. The substrate temperature is controlled by water lines attached below the sample stage and kept at 30°C. The polymerization takes place in three steps; initiation, propagation and termination. For the initiation process; tert-Butyl peroxide (TBPO) molecules are thermally decomposed to form initiator radicals by the help of heated filaments 2 cm above the sample surface. The temperature of the filaments is maintained at 270°C throughout the experiment. The initiator radicals then react with the monomer and cross-linker molecules adsorbed on the substrate surface initiating the propagation process. The thickness of the deposited film is monitored real-time using an interferometer attached to the system. For the study presented here, the thickness of the films were 50, 100, and 200 nm, respectively. Once the desired thickness is reached, the monomer and cross-linker flow to the system is stopped. The last step is the termination step, where the monomer radicals are deactivated by recombination of chains or by capping of the active sites by the initiator radicals. For this study flow rates of HEMA, EGDMA and TBPO were 0.74, 0.065 and 0.76 scms, respectively. Samples were characterized using Ellipsometry, Raman, and AFM techniques.

In the Ellipsometry analysis, measurements of the film thickness were performed using a spectroscopic ellipsometer (M2000 Spectroscopic Ellipsometer J.A.Wollam Co., Inc. [108]). All the thickness measurements were made for wavelengths ranging from 315 to 718 nm at 65, 70, and 75 incident angles, which were determined with the Cauchy fitting mode. In the Raman spectroscopy, Raman spectral analysis was conducted at the Renishaw inVia Raman Microscope attached with a 532-nm green laser and 2400 lines/mm grating [109] (Figure 5.1). The thickness-normalized and baseline-corrected Raman spectra of the pHEMA thin films correspond to the cross-linker ratio of 22%. The cross-linker ratio of the thin film was calculated using the spectra of the coated silicon wafer. The ratio of the peak area of the C=O stretching region (1730–1740 cm^{-1}) to the O-H region (3000–3400 cm^{-1}) is defined as r for the pHEMA thin film. The cross-linker

ratio is given as $\frac{EGDMA}{HEMA} = \frac{(A_{C=O} - rA_{O-H})/2}{rA_{O-H}}$. Here, $A_{C=O}$ is the area under the carbonyl stretching peak and A_{O-H} is the area under the hydroxyl peak [85].

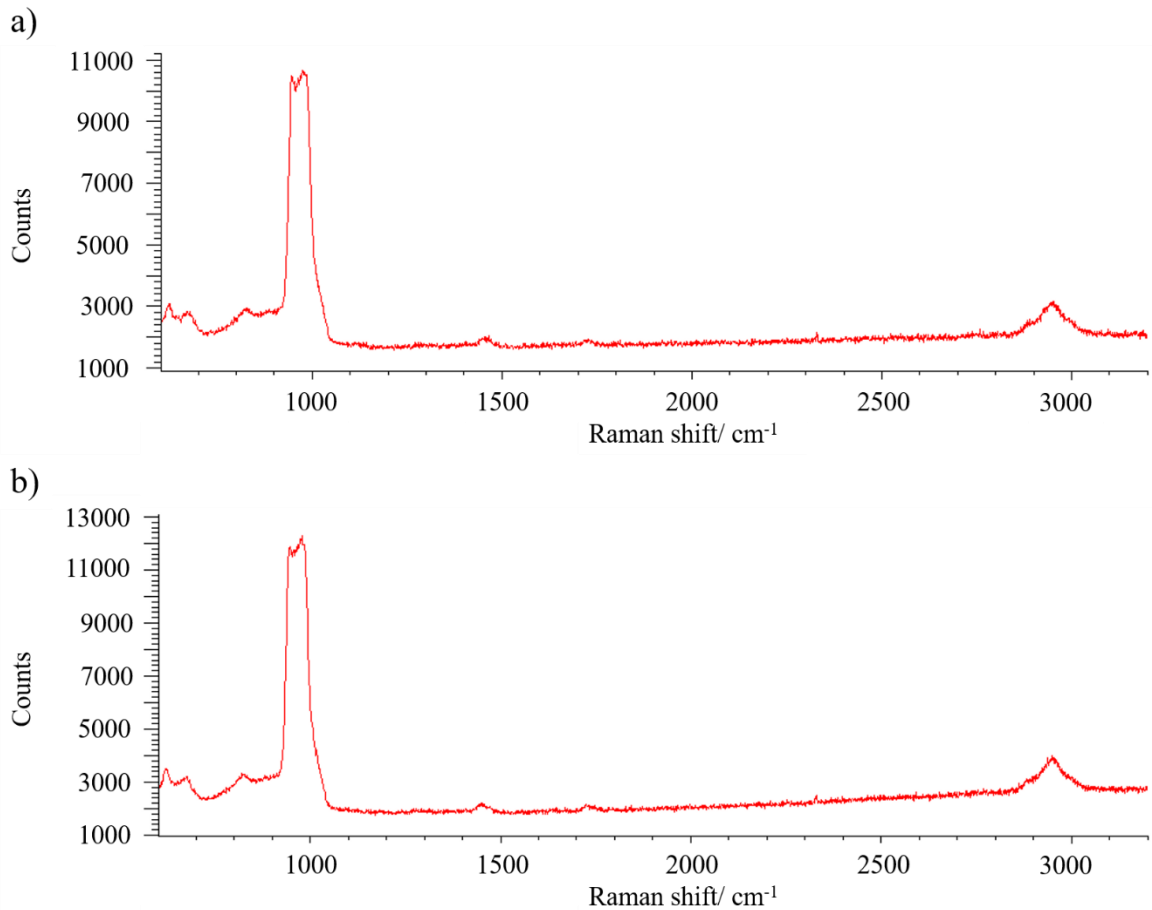


Figure 5.1 Raman spectrum taken from the pHEMA films having the thickness of 200 nm a) before the boiling experiments b) after the boiling experiments

Atomic Force Microscopy analysis (AFM): The surface properties of the polymer films were determined via Atomic Force Microscopy (Digital Instruments Nanoscope III) [110] (Figure 5.2). The roughness of pHEMA films with the thickness of 200 nm on an area of 10-micron square is measured as ± 1.8 nm before and after the boiling test. The elastic moduli of the films were measured using the peak force quantitative nano-mechanics (QNM) mode of the Multi-Mode AFM. Force curves were obtained at different parts of the polymer films, and Hertzian fit modeling was applied to the force-versus-separation curves. Accordingly, the elastic modulus of the pHEMA film with the thickness of 200 nm is found as 10.22 MPa.

The pool boiling experiments were conducted under atmospheric conditions. The reliability of coated surfaces was tested apart from the experiments. The treated pHEMA coated plate was exposed to a high temperature (150°C) by heating the plate using a film heater for a time period of 30 min. According to obtained results, no peeling or degradation was observed during and after the boiling experiments, which is consistent with the previous studies [83, 85, 115].

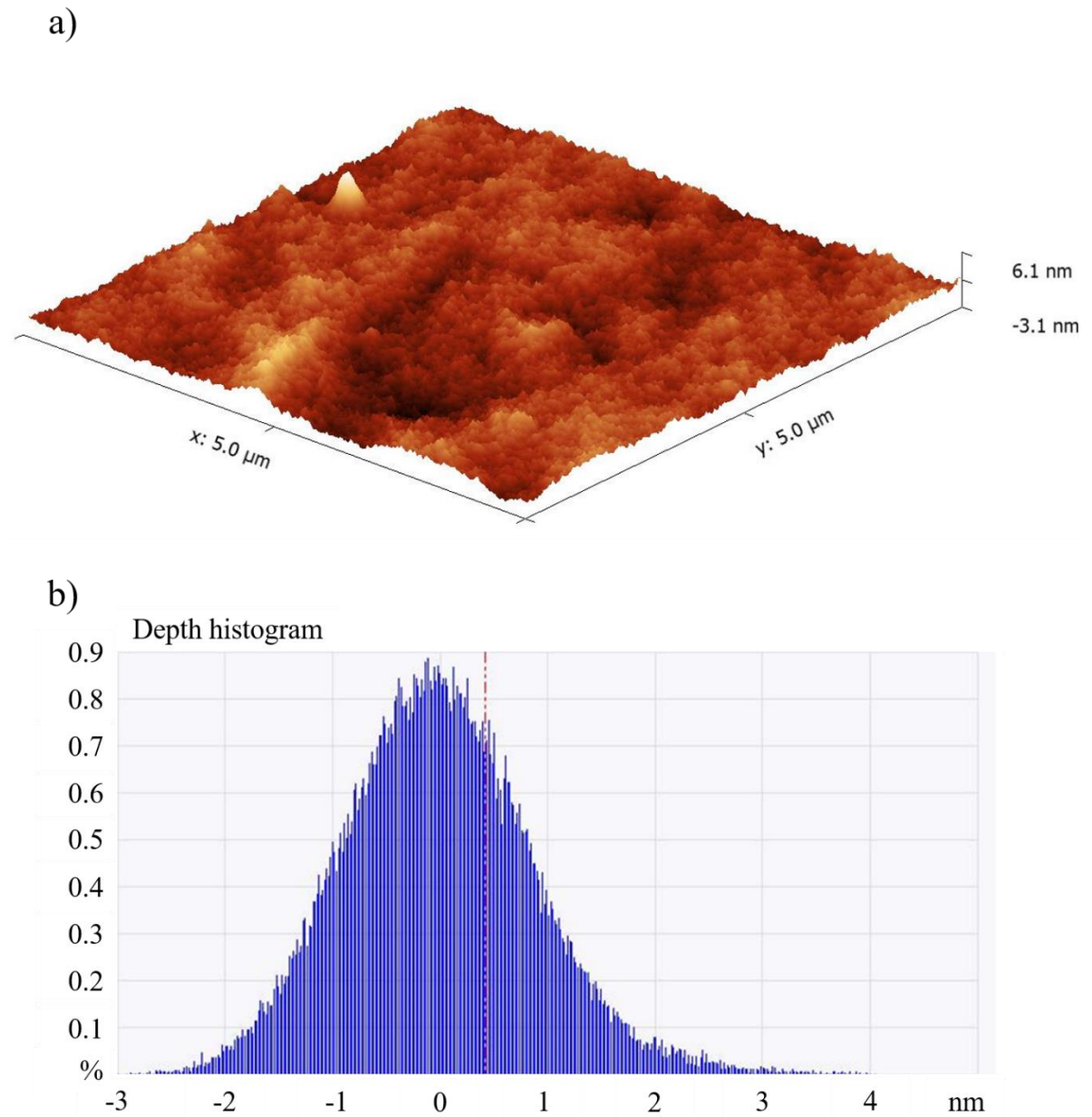


Figure 5.2 (a) Three-dimensional image and (b) depth histogram of an area of 10 μm square of the pHEMA film with the thickness of 200 nm

5.3 Results and discussion

5.3.1 Bubble nucleation and growth

Pool boiling experiments were conducted on nano-coated silicon surfaces (pHEMA coatings) with thicknesses of 50, 100 and 200 nm. One of the main characteristics of pHEMA coatings is their swelling behavior upon a contact with water, which provides a layer of porous structure on top of the silicon surface. Figure 5.3 shows the generated bubbles on the coated and uncoated surfaces for two heat fluxes of 20 kW/m² and 30 kW/m². As seen, nano-coatings have a considerable effect on bubble nucleation, and more bubbles emerge from the pHEMA coated surfaces. This is consistent with the reported data related to coated surfaces in the literature [84].

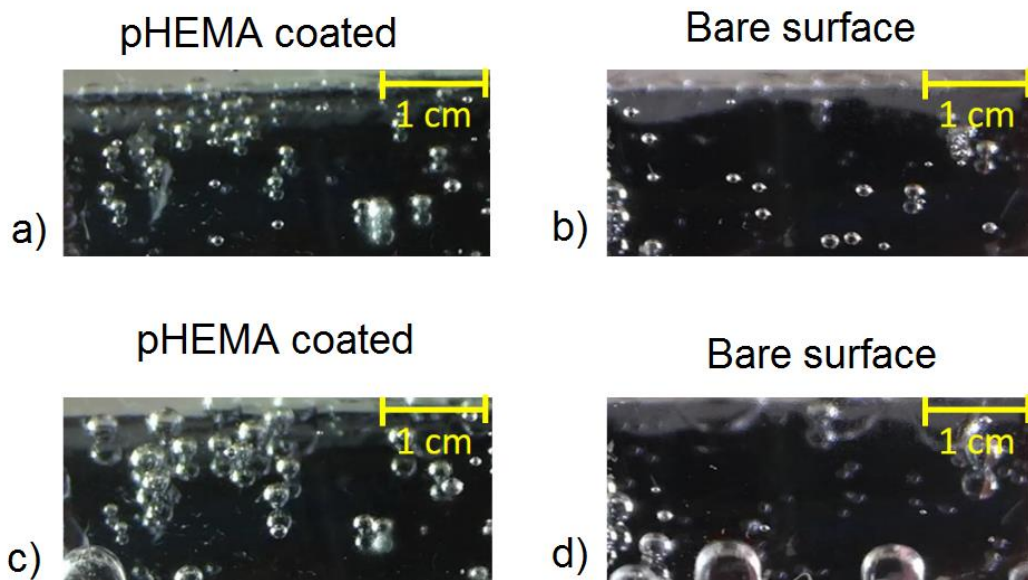


Figure 5.3 Bubbles and active nucleation sites on a) pHEMA coated surfaces with thicknesses of 100 nm for heat flux of 20 kW/m² b) silicon surface for heat flux 20 kW/m² c) pHEMA coated surfaces with thicknesses of 100 nm for heat flux of 30 kW/m² d) silicon surface for heat flux 30 kW/m²

Active nucleation site density increases with wall heat flux, and activation of nucleation sites is more dominant on coated surfaces compared to the bare silicon plate. It can be observed that numerous nucleation sites are activated inside the porous coating with a small increase in heat flux, which is shown in Figure 5.4. Accordingly, the active

nucleation site densities on bare silicon and pHEMA coated surfaces are ~ 4 and ~ 10 site/cm² at the heat flux of 35 kW/m², respectively, while they are ~ 5 and ~ 14 site/cm² at the heat flux of 50 kW/m², respectively. A similar observation was reported in the literature by Deng et al. [77].

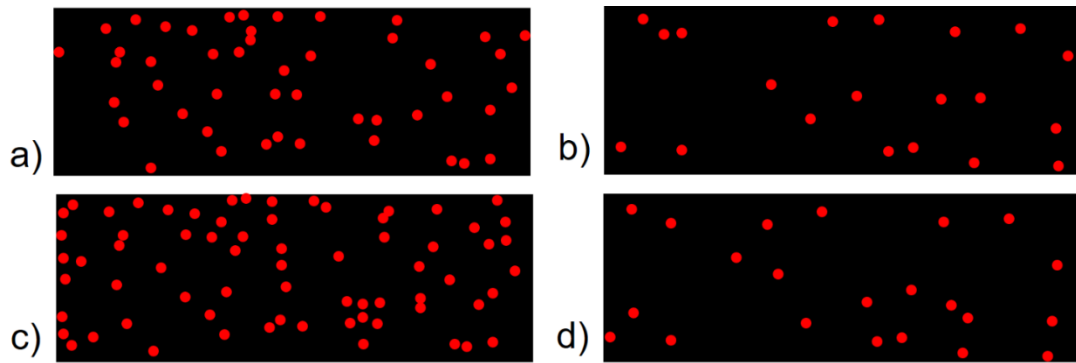


Figure 5.4 Effect of heat flux on active nucleation sites on a) pHEMA coated surface at 35 kw/cm² heat flux b) silicon surface at 35 kw/cm² heat flux c) pHEMA coated surface at 50 kw/cm² heat flux d) silicon surface at 50 kw/cm² heat flux

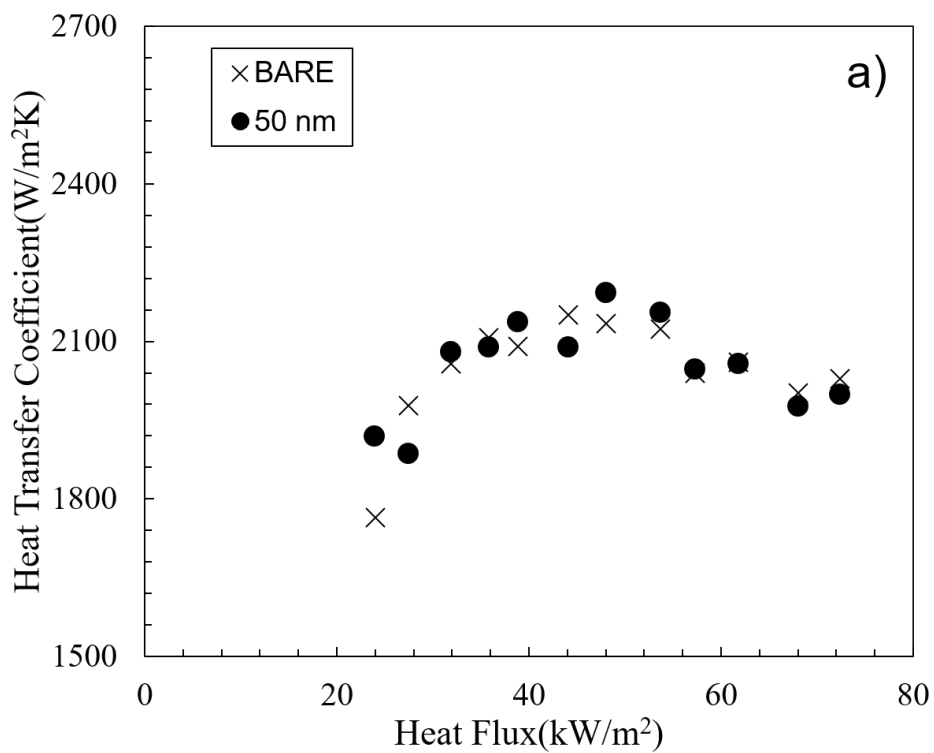
5.3.2 Boiling heat transfer

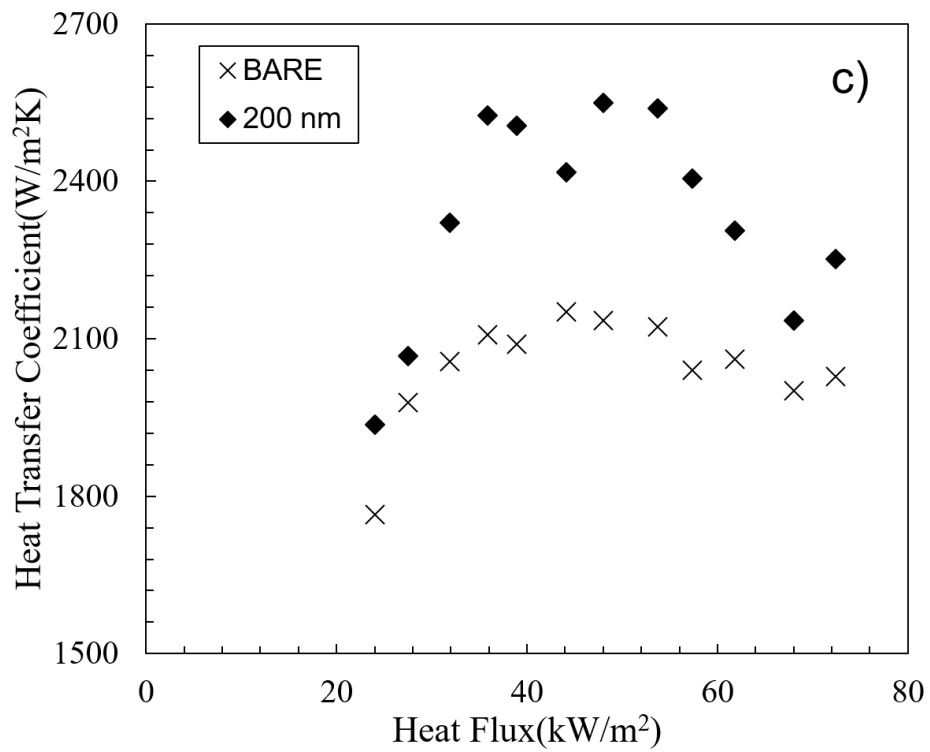
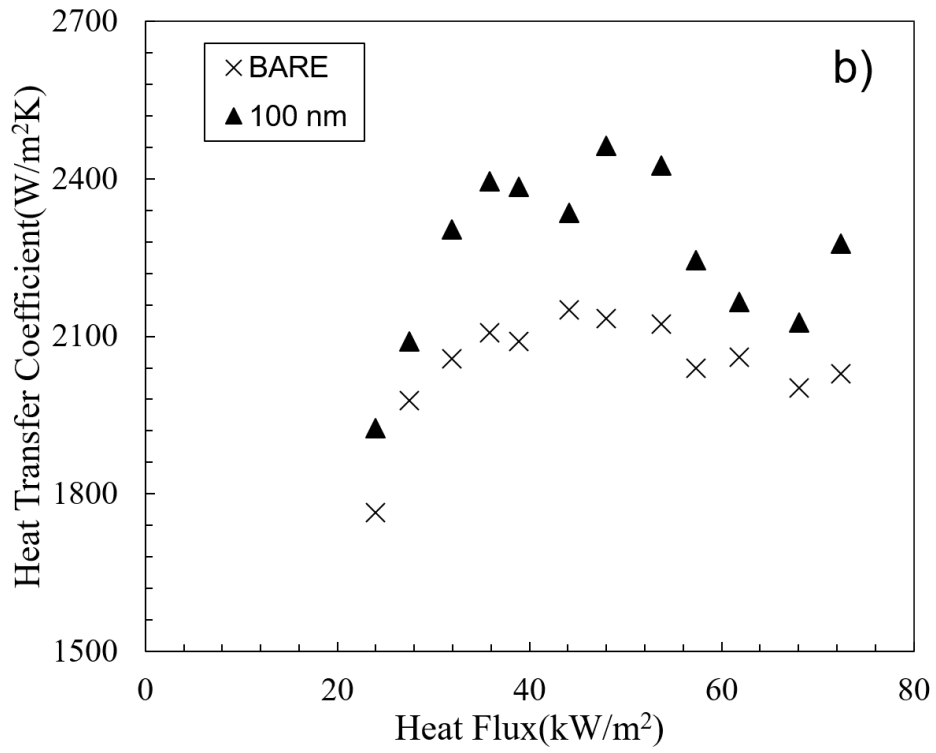
Increased active nucleation site density raises heat transfer from the surface. As a result, larger heat transfer coefficients and lower wall superheats are obtained from the coated surface at a fixed heat flux. Figure 5.5 shows the obtained heat transfer coefficients for silicon and pHEMA coated plates with different thicknesses. Enhancement in heat transfer coefficients on pHEMA surfaces can be seen relative to the bare silicon surface. In addition to more active nucleation sites, bubble departure frequencies are higher on coated surfaces resulting in heat transfer coefficient augmentation. On the other hand, the decrease in contact angle on the pHEMA coated surface (from 42° to 37°) leads to higher wettability, which affects the nucleation process in nucleate pool boiling by decreasing the number of active nucleation sites. However, surface porosity effects and subsequent modified bubble dynamics effects are dominant over this effect.

Furthermore; the effect of heat flux on average heat transfer coefficient enhancement for different coating thicknesses is shown in Figure 5.5d. For the coated surface with the thickness of 50 nm, a decreasing trend in heat transfer enhancement with wall heat flux can be seen, while this plate has lower heat transfer coefficients compared to the bare silicon surface for heat fluxes higher than 60 kW/m². On the other hand, an increasing

trend in enhancement is apparent with thickness for coated surfaces with thicknesses of 100 and 200 nm. The maximum enhancements are about 10%, 15%, and 20% for the surfaces with coatings having thicknesses of 50, 100 and 200 nm, respectively. The enhancements are larger for low and medium heat fluxes, while they become lower for higher heat fluxes.

In addition to more active nucleation sites, the enhancement in heat transfer on coated surfaces is attributed to the combined effects of the interaction between active nucleation sites, the increase in bubble generation frequency, and the increase in bubble interactions. This was also reported in the study of Chen and Peterson [116].





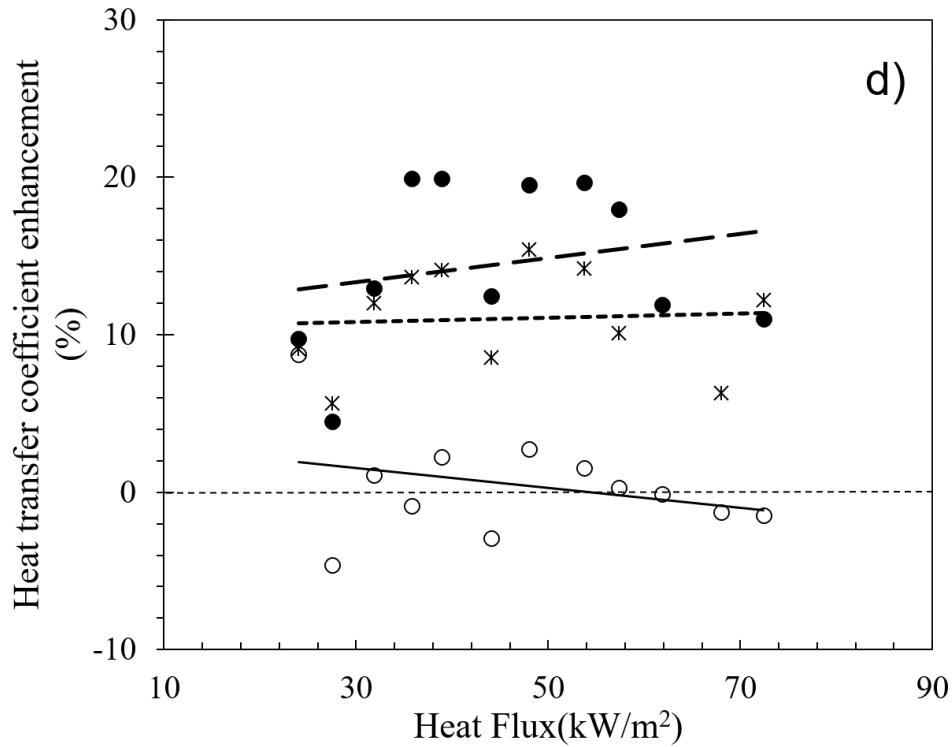


Figure 5.5 Heat transfer coefficients for pHEMA coated surfaces with thicknesses of a) 50, b) 100 c) 200nm d) heat transfer enhancement

Bubble nucleation and growth on pHEMA coated surfaces occurs in three stages. In the early stage of bubble nucleation on the pHEMA coated surfaces (stage 1), some small bubbles right upon their generation move along the surface, while their size grows (Figure 5.6). The resulting rewetting due to bubble movement on the pHEMA coated surface is another reason for heat transfer enhancement. According to the pixel-wise analysis, bubbles move with an average axial (x-direction) velocity of 22.4 mm/s at the heat flux of 40 kW/m². It should be noted that the maximum traveled distance for a bubble before departure is observed to be approximately 4 mm. According to visualization results, bubble departure diameter on pHEMA surfaces decreases by 15% in comparison to the bare silicon surface.

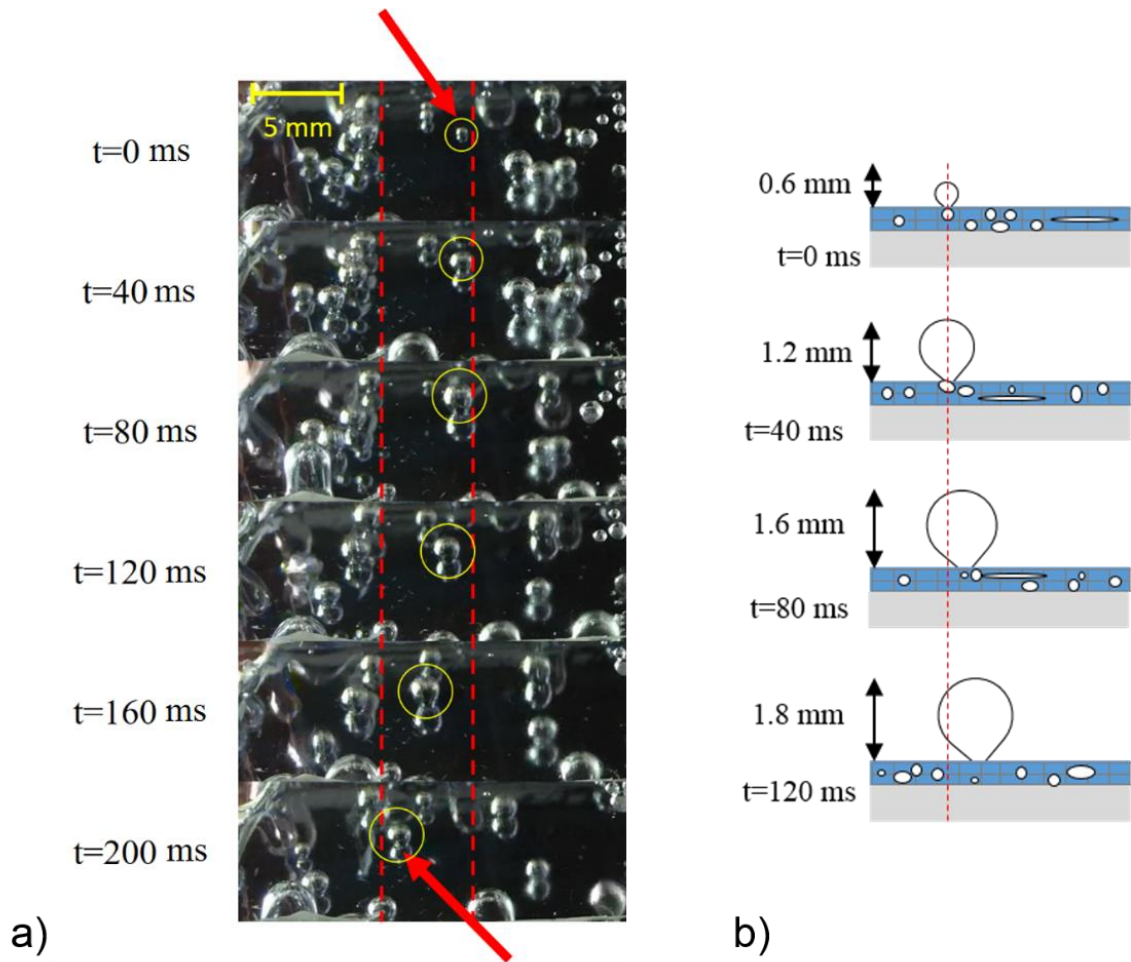


Figure 5.6. Bubble movement on pHEMA coated surfaces b) schematic of moving bubble in the growth stage

When the bubble size increases and the force acting on the bubble is not strong enough to move the bubble, bubble sticks to the surface and starts to grow and depart (stage 2). As seen in Fig. 10a, the surface tension force (still attached to the surface) resists the bubble growth. Therefore; the bubble keeps growing while still attached to the surface. In other words, on the bare silicon plates, the bubble diameter is a function of wall superheat and heat flux. On the other hand, for the pHEMA porous surface, as seen in Figure 5.7d, the bubble growth is confined to the edge of surface pores until the bubble starts to depart from the pore. It should be noted that one edge of the growing bubble remains in contact with the periphery of the surface pore, and the vapor is generated from the evaporation of the liquid inside surface pore. Therefore, on the structured surface, the pore diameter (coating thickness), the supply path of vapor as well as the heat flux are significant parameters, which determine the departure diameter of the bubble.

In the third stage of bubble nucleation and growth, bubble coalescence is observed on coated surfaces. Figure 5.7c and Figure 5.7d show bubble interactions near the departure point, and bubble departure angle on the coated and uncoated surfaces. Bubble coalescence during the departure on the porous surface helps the detachment of the bubbles. The interaction among nucleation sites is one of the main reasons for heat transfer enhancement.

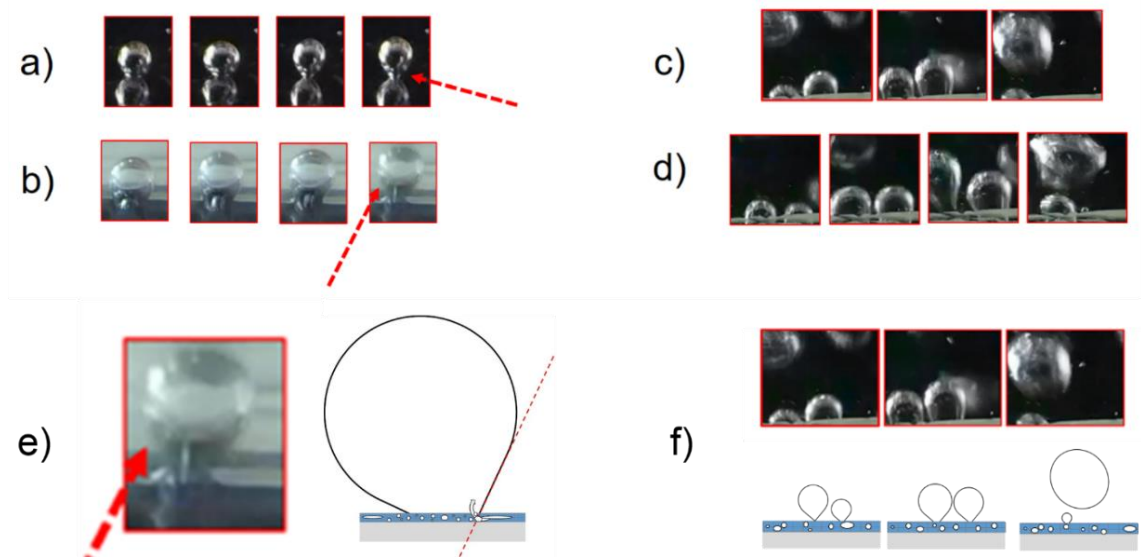


Figure 5.7 Bubble growth on a) bare silicon plate and b) pHEMA coated surface c- d) Bubble coalescence and interaction upon the departure on coated surfaces e) schematic of bubble departure on coated surface f) schematic of bubble coalescence on the coated surface

Pool boiling experiments were conducted on surfaces with inclination angles of 10° , 30° , 50° and 70° . Figure 5.8 shows generated bubbles on oriented surfaces for pHEMA coatings with the thickness of 100 nm. As seen, surface orientation has a major effect on bubble generation. Accordingly, the number of active nucleation sites increases with surface orientation while the number of activate nucleation sites is notably different for inclination angles of 10° , 30° , and 50° (larger for larger angles), and a smaller difference is apparent for surfaces with inclination angles higher than 50° .

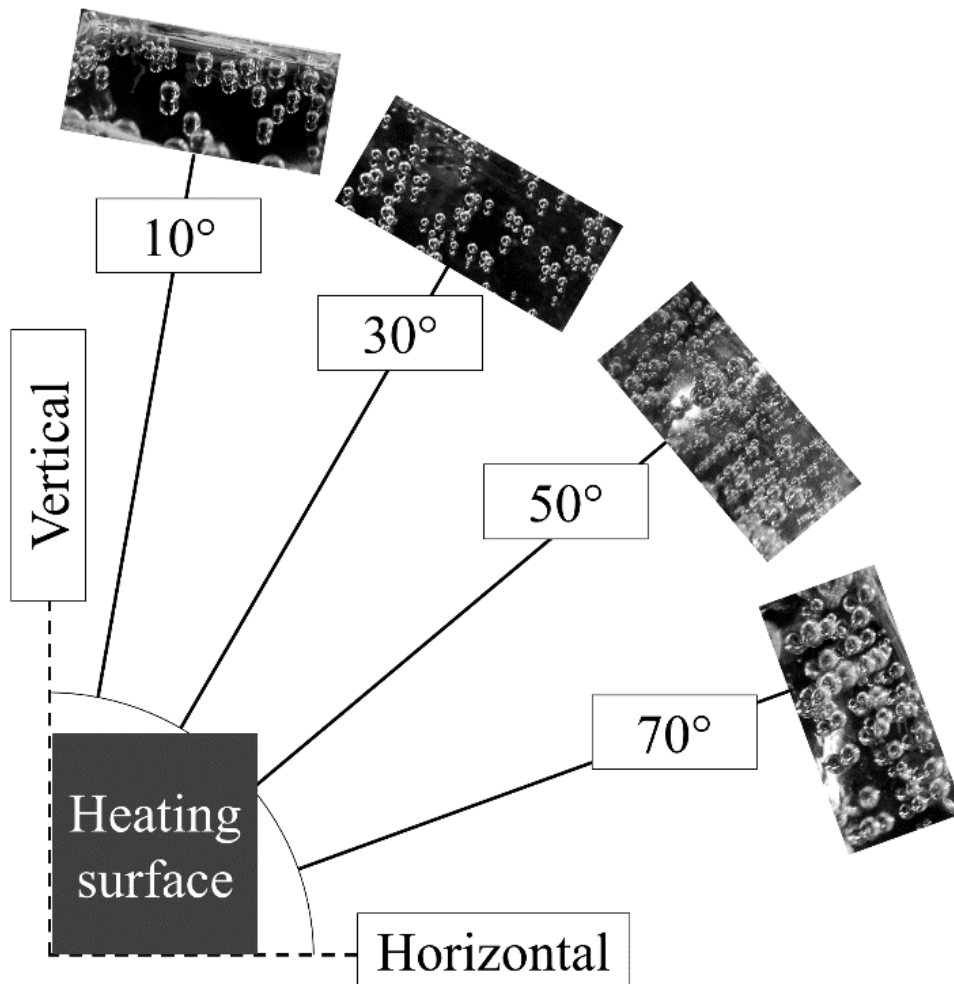


Figure 5.8 Effect of surface orientation on active nucleation sites on the surface with coating thickness of 100 nm

Surface orientation plays a major role on bubble dynamics. Figure 5.9 shows the coalescence of three bubbles for a time interval of 200 ms. Disregarding the horizontal movement of bubbles on the pHEMA coated surfaces (as showed in Figure 5.7), in contrast to the horizontal surface, where the bubbles mostly individually nucleate and depart, bubble sliding and coalescence along the wall happens on inclined surfaces. Bubble sliding on oriented surfaces results in forming a large merged bubble. Furthermore; due to higher nucleation site density on inclined surfaces (Figure 5.8), bubble coalescence is easily achieved on inclined surface. Such an observation was also reported by the study of Jung et al. [117].

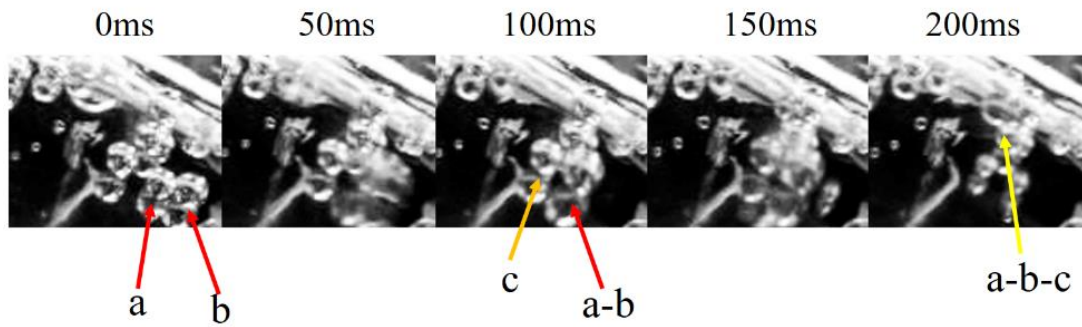


Figure 5.9 Bubble movement and collision on inclined surface

The schematic of the heat transfer mechanism on pHEMA coated surfaces is shown in Figure 5.10. Inclination of pHEMA coated surface is a method serving for vapor venting, which is one of the major mechanisms in boiling heat transfer enhancement. Vapor removal methods such as open channel geometry, foam structured surfaces, porous coatings, nano-wire coatings, membranes have been used for fast vapor phase removal from surfaces [94, 118-125]. Generated vapor inside the porous network escapes through the pores to the surface. As a result, escaped vapor provides free space in the porous matrix, which constitutes a path for the liquid to fill the generated space. This mechanism provides stable vapor departure and liquid replenishment in the porous structure, which leads to higher bubble departure frequency followed by effective heat transfer [123, 124, 126, 127].

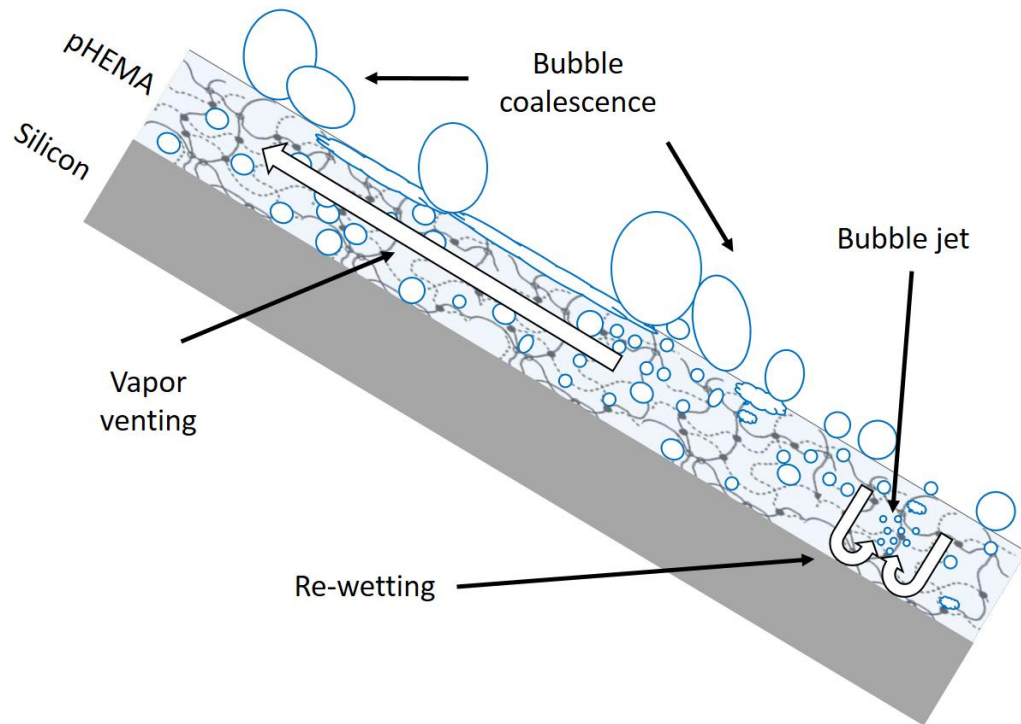
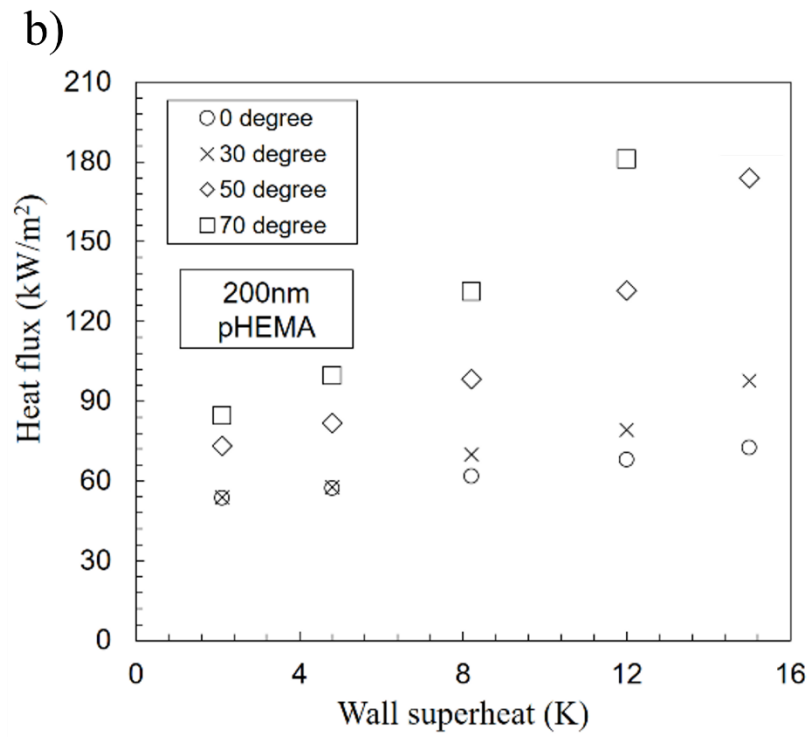
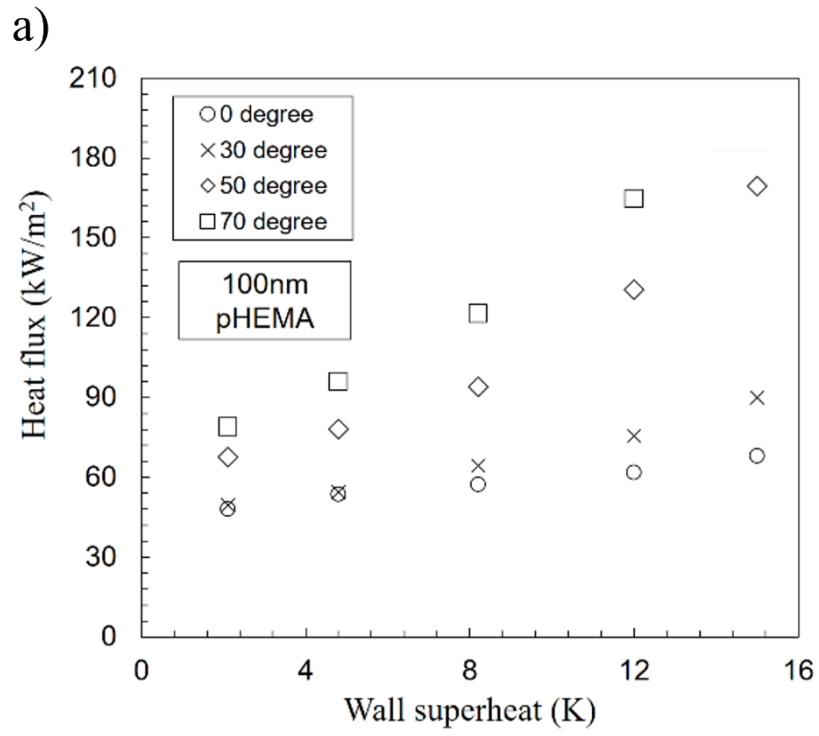


Figure 5.10 Schematic of heat transfer enhancement mechanism on the inclined pHEMA coated surface

The typical pool boiling curves for inclined coated surfaces (30° , 50° and 70°) thicknesses of 100 nm and 200 nm are shown in Figure 5.11a and Figure 5.11b, respectively. As seen, applied wall heat fluxes on oriented surfaces are higher than horizontal surfaces. Furthermore; obtained average enhancements in heat transfer on inclined coated surfaces with thicknesses of 100 nm and 200 nm are shown in Figure 5.11c. Heat transfer coefficient enhancements on inclined surfaces with inclination angle of 70° are more than 110%. According to the obtained results pHEMA coatings on oriented surfaces have proven to be a promising method for enhancing heat transfer.



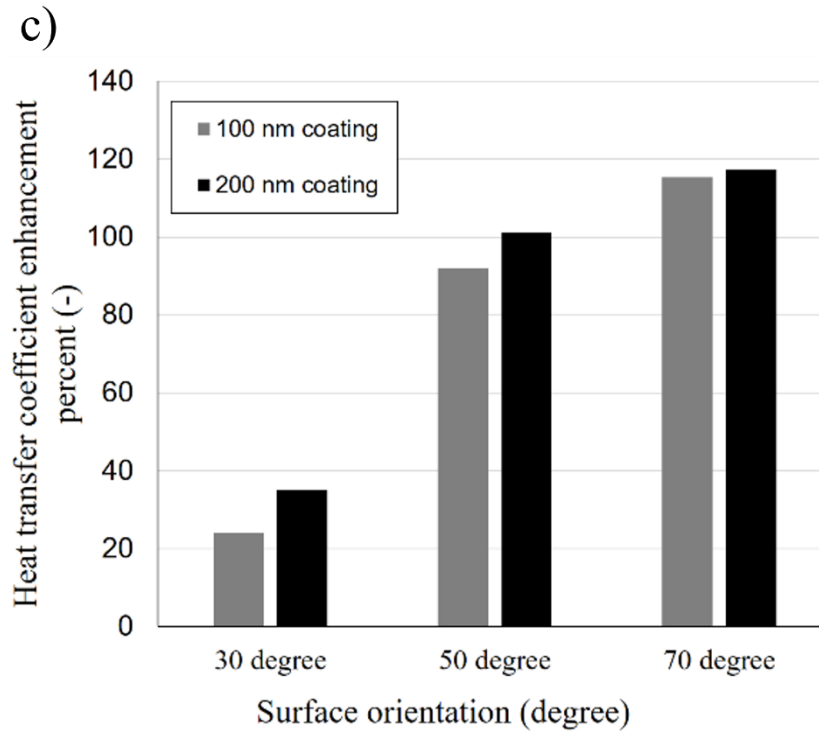


Figure 5.11 Effect of inclination angle on pool boiling curve for a) 100 nm coated surface b) 200nm coated surface c) percent of heat transfer coefficient enhancement

5.4 Conclusion

Pool boiling on pHEMA coated surfaces was investigated in this study. Coated samples with thicknesses of 50, 100 and 200 nm were used to study the effect of surface porosity and inclination angle on heat transfer and bubble departure process. Bubble departure process was recorded using a high speed camera. It was found that pHEMA coated surfaces result in more active nucleation sites with a higher bubble departure frequency compared to bare silicon wafer. Higher heat transfer coefficients were obtained from the coated surfaces. According to obtained visual results, combination of the effects of the interaction between active nucleation sites, the increase in bubble generation frequency, and the increase in bubble interactions were presented as the reasons behind the enhancement in heat transfer. It was observed that the inclined pHEMA coated surface offers effective vapor venting. Under an optimum condition for the inclination angle, the porous coating provides a suitable escape path for vapor phase, which results in space to be filled by the liquid phase thereby enabling liquid replenishment.

Part 3: Application

3D Graphene and Bio-coated surfaces for thermal management

6. 3-D Graphene coating

6.1 Introduction

In this chapter, the effect of 3-D graphene coated surfaces on boiling heat transfer is presented and discussed in details. Graphene is a new material and additionally due its unique properties and interesting capabilities, graphene has received much attention. Graphene consisting of sp^2 -hybridized carbon atoms in two dimensional hexagonal lattice [128] has been a promising alternative for many fields owing to its high thermal and electrical conductivity, noteworthy optical transmittance, superior chemical stability and high flexibility [129-132]. Although graphene has these unique properties, its preparation typically results in cracks, wrinkling, defects and mechanical problems when integrated into three dimensional applications [133-136]. To overcome this drawback, graphene has been prepared in three dimensional forms such as aerogel, foam and sponge during the last decade. These forms have low mass density, large surface area, good mechanical stability, high thermal and electrical conductivity. Besides energy, sensing, detecting, tissue engineering, and environmental applications [132, 137, 138], three dimensional (3D) graphene frameworks also have a potential in heat transfer enhancement because of their high thermal conductivity and porosity [139-145].

3D-graphene foams with thicknesses of 8, 13, 29, and 55nm were grown on porous nickel foam with a thickness of 1.6 mm and pore sizes ranging between 60-700 μ m (\geq 95% porosity, 99.99% purity) by the chemical vapor deposition (CVD) method in a horizontal furnace system. The forces acting on the bubbles in the porous media is investigated, and the effect of pore size on bubbling behavior is discussed. Boiling heat transfer and bubble dynamics characteristics were observed by using a high-speed camera and parametric results, the effects of coating thickness on nucleation site interactions and boiling heat transfer were discussed in detail.

6.2 Sample preparation and characterization

After the foams were cut to a size of 15mm×15mm, they were placed in the central zone of a horizontal quartz tube of a length of 1400 mm. Prior to the experiments, the vacuum chamber was evacuated using a dry pump until the pressure reached 2×10^{-2} Torr. Then, the furnace was heated up to the desired growth temperature within 20 min under H₂ and Ar flows. To provide a homogeneous graphene coating on a nickel foam substrate, the foams were annealed for 10 min with Ar and H₂ gases at the growth temperature. CH₄ as a carbon precursor was propelled at the required flow rate into the quartz tube for 7.5 to 12 min for the growth of graphene foams. Finally, the samples were allowed to cool down to the ambient temperature under Ar flow. The CVD growth conditions are summarized in Table 6-1. Three-dimensional graphene foams were transferred on SiO₂ surface using wet etching procedure. The detailed transferring procedure is shown in Figure 6.1.

Table 6-1 Growth parameters for prepared graphene foams using the chemical vapor deposition (CVD) method.

Sample No	Growth Temperature (°C)	Growth time (min.)	CH ₄ (sccm)	H ₂ (sccm)	Ar (sccm)
#1	975	12.5	80	100	275
#2	975	12.5	80	100	425
#3	975	7.5	80	100	275
#4	925	7.5	80	100	275

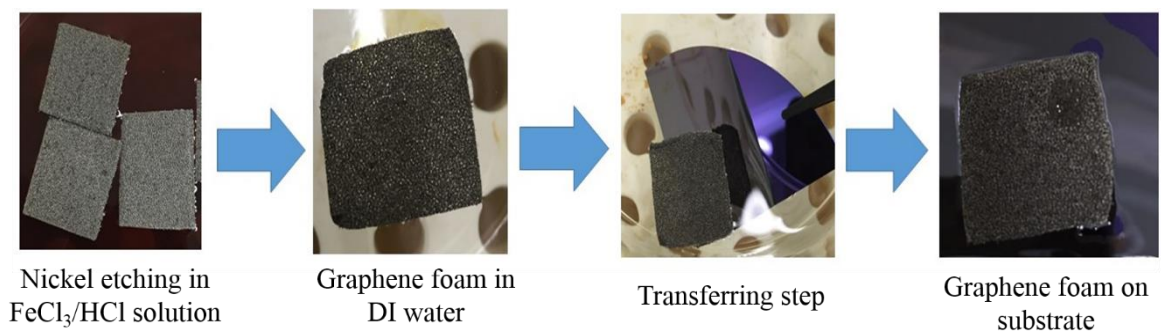


Figure 6.1 Transferring of graphene foam on substrate.

Because of the nature of SiO_2 , its surface contains abundant silanol (SiOH) groups. These groups are sensitive to the adsorption of water molecules, thus SiO_2 surface is hydrophilic. On the other hand, graphene shows hydrophobic feature in nature. This hydrophilic/hydrophobic interaction causes instability of the between interface of graphene and SiO_2 during transferring of graphene by wet etching procedure [146-150]. As a result, graphene cannot properly attach on SiO_2 surface. The adhesion between foam and substrate was tested using heating procedure. Samples (GF/substrate) were heated at different temperature (i.e. 25° , 40° and 80°), following by immersed into water. The immersion tests of samples into water are shown in Figure 6.2. As seen in Figure 6.2a and Figure 6.2b, foams heated 25° and 40° separated from substrate as they were immersed into water. On the other hand, the foam heated 80° didn't separate from substrate even it was immersed into water (Figure 6.2c and Figure 6.2d).

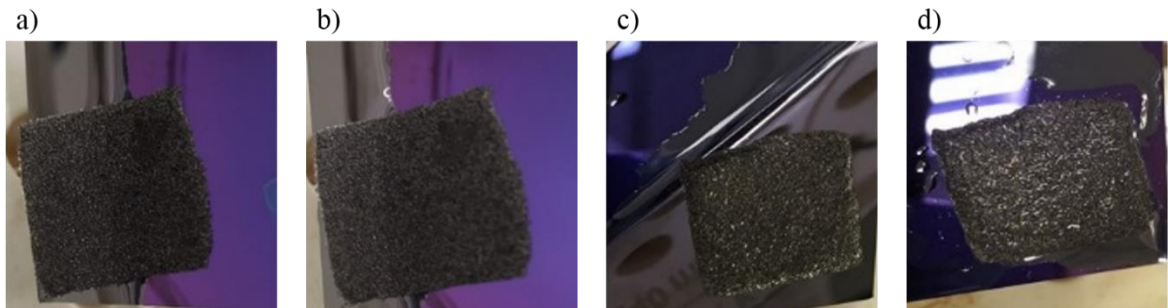


Figure 6.2 Adhesion tests between graphene foam and substrate

In order to obtain graphene foams without nickel scaffold, nickel foams were etched in 1 M FeCl_3 solution for 24 hours. After the nickel foams were completely etched, graphene foams were cleaned in de-ionized water/ HCl mixed solutions until FeCl_3 residues were completely gone. At the last step, the samples were transferred onto SiO_2/Si substrate with $20\text{mm} \times 20\text{mm}$ and then dried at 80°C for 30 min in an oven to enable the adhesion of the graphene foams on substrate. The Brunauer-Emmet-Teller (BET) surface area measurement technique (Micromeritics ASAP 2020) was used to measure the specific surface area of graphene foams. The samples were degassed using flowing N_2 at 200°C for 24 h before the measurements. The characterization of 3D-graphene foams was performed by the X-Ray Diffraction (XRD, Bruker AXS Advance), Raman (Renishaw inVia Reflex) and SEM (SEM, Zeiss Gemini 1530) techniques. The crystalline

structures of samples were determined by XRD patterns, which were obtained at ambient temperature over 2θ values within the range of 20° – 80° under Cu $K\alpha$ X-radiation ($\lambda_{Cu} = 1.5406 \text{ \AA}$). The Raman spectra were collected for the wavelength of 100 to 3200 cm^{-1} under 532 nm excitation at $2\mu\text{m}$ spot size to identify the graphene morphology. The scanning electron microscope (SEM) operated at 20 kV was used to observe 3D structures of graphene foams. shows the graphene thicknesses for each sample.

Table 6-2 Sample characterization. Specific surface area (SSA), graphene thicknesses, and water contact angles measurement of each sample.

Sample No	Specific surface area (m^2/g)	Graphene thickness (nm)	WCA measurement (degrees)
#1	550	8	$123\pm 1^\circ$
#2	350	13	$124\pm 1^\circ$
#3	150	29	$125\pm 1^\circ$
#4	80	55	$128\pm 1^\circ$

The three-dimensional networks are identified via the scanning electron microscopy (SEM) technique, as shown in Figure 6.3, for sample #4. The SEM image of the interconnected 3D-nickel foam structure with a smooth surface is shown in Figure 6.3a. After CVD growth, graphene layers cover the nickel foam surface (Figure 6.3b). Single layer graphene flakes and multilayer graphene flakes are represented as single layer graphene (SLG) and multilayer graphene (MLG) on the SEM image, respectively. Figure 6.5c displays the SEM images of graphene foams without nickel foam template. It can be seen from SEM images that graphene foam copied the interconnected 3D structure of nickel foam template. Since the graphene foam is extremely thin, wrinkles occur on the graphene surface during the etching process. The pore size of graphene foam was calculated as between 70 – $400 \mu\text{m}$, and the thickness of branch width was found to be about $70\mu\text{m}$.

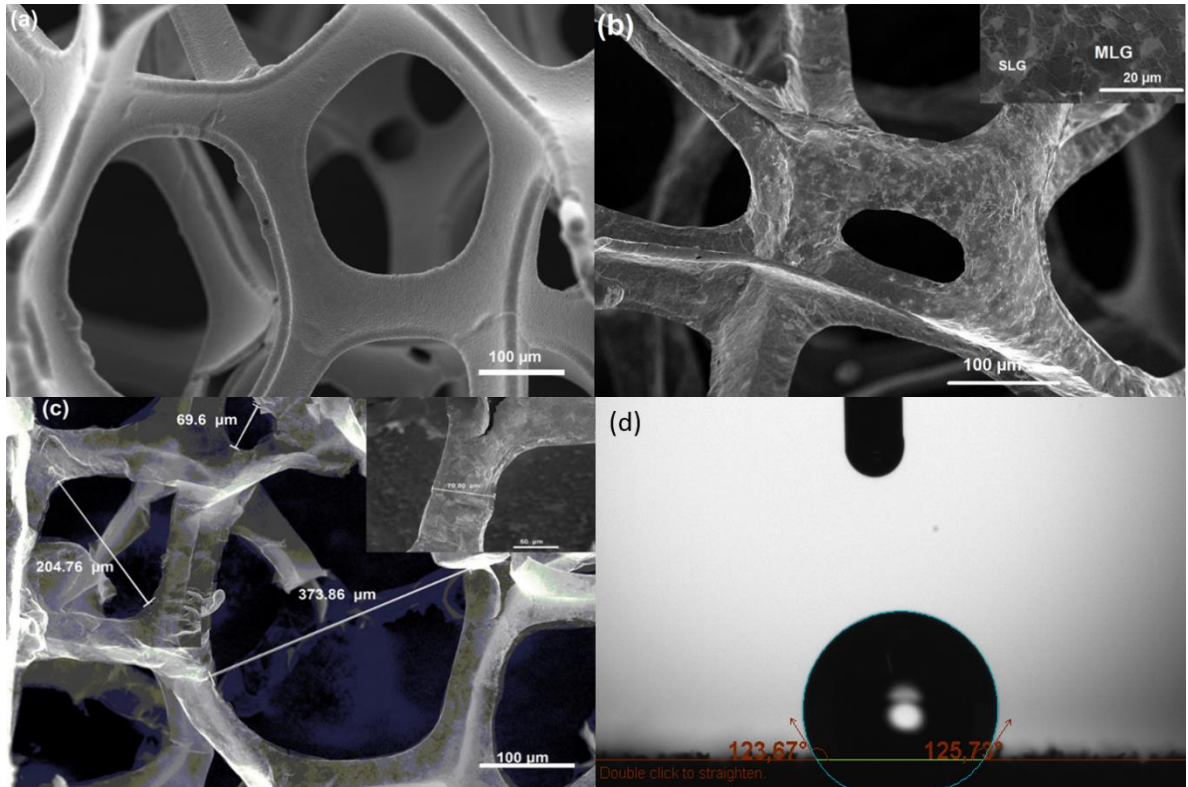


Figure 6.3 Obtained SEM images for (a) nickel foam, (b) GF/nickel foam (c) GF (sample#4) d) contact angle goniometer image (sample#3).

Figure 6.4a displays XRD spectrum of the 3D graphene foam (sample #4). The sharp diffraction peaks (2θ) at 26.5° , corresponding to the plane (002), are reflections of the high crystallinity of defect-free CVD grown graphene. (JCPDS 75-1621). In Figure 6.4b, Raman spectrum of the 3D-graphene foam (Sample-4) is depicted. In this spectrum, three specified graphene peaks centered at 1580 , 2550 and 2720 cm^{-1} , which are attributed to G, G* and 2D bands as can be clearly observed, while the D band at 1350 cm^{-1} (which is associated with disorders) cannot be detected. The absence of D peak in Raman spectrum indicates that graphene foams are of high quality. The intensity of I_{2D}/I_G correlated with number of graphene layers was calculated between 1.58 and 0.36 for graphene foams. According to this result, it can be deduced that single-layer and multi-layer graphene flakes coexist together in 3D-graphene foams.

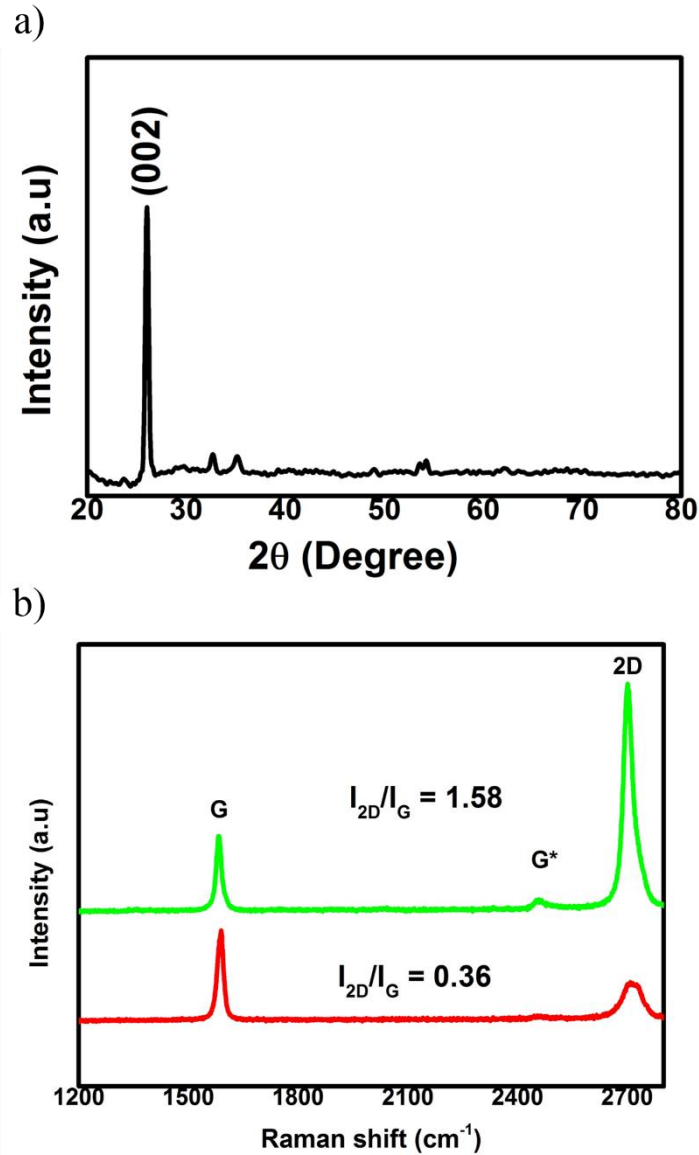


Figure 6.4 a) XRD spectrum of 3D-graphene foam (samle#4) b) Raman spectrum of 3D-graphene foam (sample#4)

6.3 Discussion

It is known that only cavities within a specific size range can be activated during the nucleation process at low wall superheats. The size range depends on several factors such as liquid superheat, implying that a sufficient liquid superheat is required for bubble growth from a nucleus. Figure 6.5 compares the bubble nucleation process from a single cavity and within porous medium. As can be seen, bubble nucleation from surfaces with only discrete cavities strongly depends on the individual cavity radius and its surrounding

fluid temperature, which causes different bubble departure diameters on such surfaces (Figure 6.5a). For surfaces with porous coatings, as demonstrated in Figure 6.5b, the cavities are connected with a mesh structure. By providing interconnected paths for liquid and vapor phases, the pore network increases the interaction among nucleation sites and surrounding fluid.

Pool boiling experiments were conducted under atmospheric pressure using deionized water as the working fluid. A detailed description of the experimental setup, procedure and uncertainty analysis is presented in APPENDIX 2. Heat transfer mechanisms and forces acting on the individual bubbles in partial nucleate boiling region (wall superheat lower than $\sim 15(\text{K})$) and vapor columns in developed nucleate boiling (wall superheat higher than $\sim 15(\text{K})$) are different from each other. It should note that the difference between wall and saturation temperatures (boiling point at the saturated pressure - in this experiments $T_{\text{sat}} = 99(^{\circ}\text{C})$) is defined as wall superheat (ΔT_{sup}).

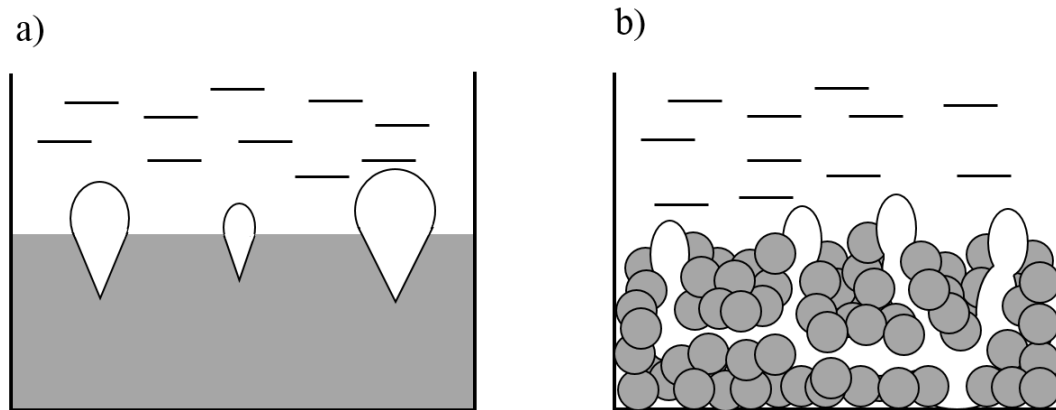
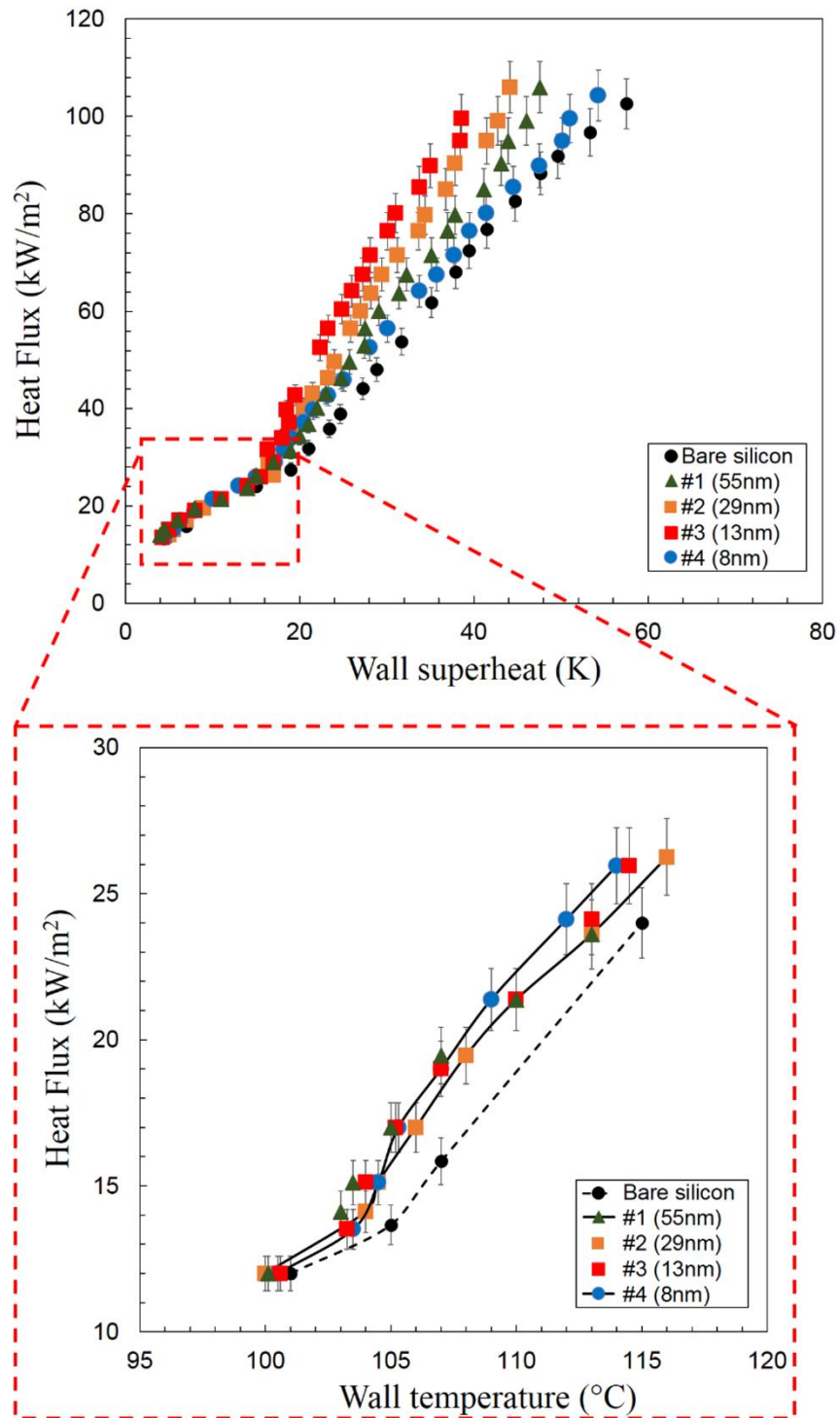


Figure 6.5 Bubble nucleation from surfaces with a) discrete cavity structure b) pore network. The porous medium directly affects the nucleation process by providing interconnected paths for vapor and liquid transport.

The onset of partial nucleate boiling is identified with individual bubbles growing and departing from the heated surface. According to the obtained wall superheats shown in Figure 6.5a, at a fixed wall heat flux (up to $\sim 30 (\text{kW}/\text{m}^2)$) graphene coatings have a considerable effect on wall superheat ($\Delta T_{\text{sup}} < 15(\text{K})$). Due to high thermal conductivity of graphene coating, bubbles not only nucleate at the bottom of coating but also nucleation happens within the porous medium. The heat transfer coefficients are shown in Figure 6.5b. As expected, promising heat transfer enhancement is observed for graphene

coatings. The heat transfer enhancement at partial nucleate boiling ($\Delta T_{\text{sup}} < 15 \text{ K}$) increases with graphene thickness, such that the maximum heat transfer enhancement for coatings with graphene thicknesses of 55, 29, 13, and 8 nm are ~56%, ~33%, ~23%, and ~12%, respectively.

a)



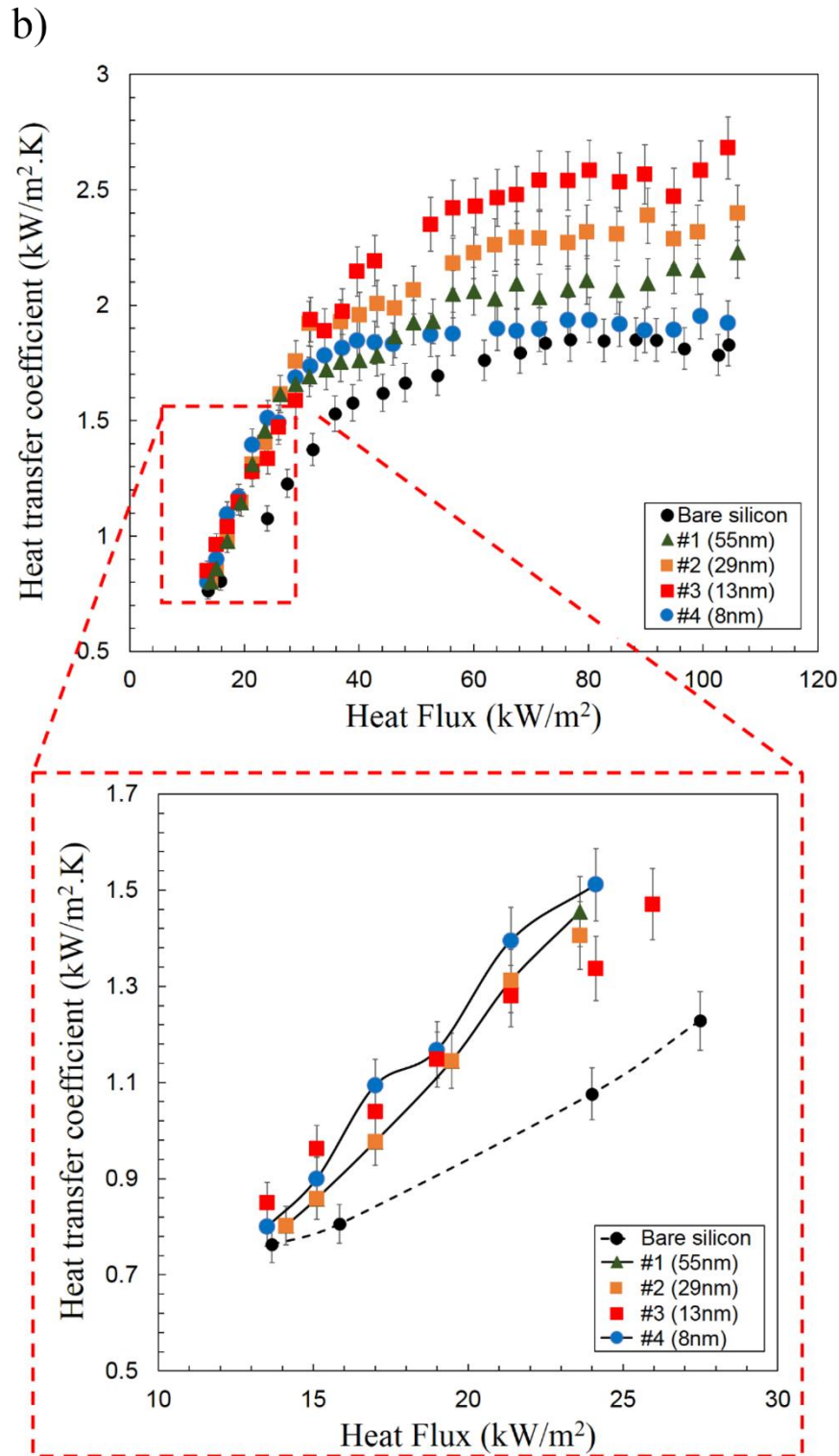


Figure 6.6 Obtained wall superheats (a) and calculated heat transfer coefficients (b) as a function of applied heat flux for bare silicon and graphene coated surfaces.

In order to have an understanding about the bubble departure diameter at partial nucleate boiling, a model is developed based on the bubble growth force, buoyancy force, inertia forces, lift force, and surface tension force [151]. Figure 6.8a shows the forces

acting on a departed bubble from a pore. The buoyancy and lift forces tend to detach the bubble from the surface while other forces keep it attached. The force balance equation is obtained as:

$$F_{Bouyancy} + F_{Lift} - (F_{growth} + F_{Surfacetension} + F_{inertia}) = 0 \quad 6.1$$

The expressions of the forces acting on the bubble is used to analyze the effect of graphene coating on the bubble upon the departure point are as follows:

$$\text{Bubble growth force} \quad F_{growth} = 10 \rho_l \pi \dot{D}^2 D^2 \quad 6.2$$

$$\text{Buoyancy force } F_{Buo} = (\rho_l - \rho_g) g \left[\frac{\pi}{3} \left(\frac{D^3}{4} + \frac{D^2}{4} \sqrt{D^2 - D_p^2} + \frac{D_p^2}{8} \sqrt{D^2 - D_p^2} \right) \right] \quad 6.3$$

$$\text{Surface tension force} \quad F_{ST} = \sigma \pi D_p \sin \left(\sin^{-1} \left(\frac{D_p}{D} \right) \right) \quad 6.4$$

$$\text{Lift force} \quad F_{Lift} = \frac{2.4}{8} \pi \rho_l (D_b \dot{D})^2 \quad 6.5$$

$$\text{Inertia force} \quad F_{Inertia} = \dot{D}^2 \rho_v \frac{\pi}{12} \left(\frac{3D^2}{4} + \frac{1}{4} \left(\frac{D^3 - 2DD_p^2}{\sqrt{D^2 - D_p^2}} \right) - \frac{D_p^2 D}{8\sqrt{D^2 - D_p^2}} \right) \quad 6.6$$

Here, ρ , D , D_d , and σ are density, bubble diameter, bubble departure diameter, and surface tension, respectively [152, 153]. The departure diameter can be obtained at the departure time by balancing the acting forces on the bubble.

The heat transfer from the superheated liquid into the bubble is considered to be a transient conduction process (Figure 6.7b). Within the porous medium, heat transfer from the superheat liquid is much more than the uncoated sample. Taken into account that at partial nucleate boiling region bubble nucleation strongly depends on liquid superheat, 3D graphene foam acts as a conductive network providing the required liquid temperature for the onset of nucleation process. The time required for the liquid to attain this superheat is called the waiting period. Heat transfer from the superheated liquid into the bubble is considered to be a transient conduction process. The graphene network reduces the waiting period, thereby offering enhanced conduction heat transfer within the porous medium and consequently enhanced pool boiling heat transfer. This accelerates the

nucleation process and results in lower bubble growth force, as shown in Figure 6.7a. Consequently, graphene coating reduces the bubble departure diameter. Bubble departure diameter decreases simultaneously with a departure frequency decrease, which enhances cooling of the surface.

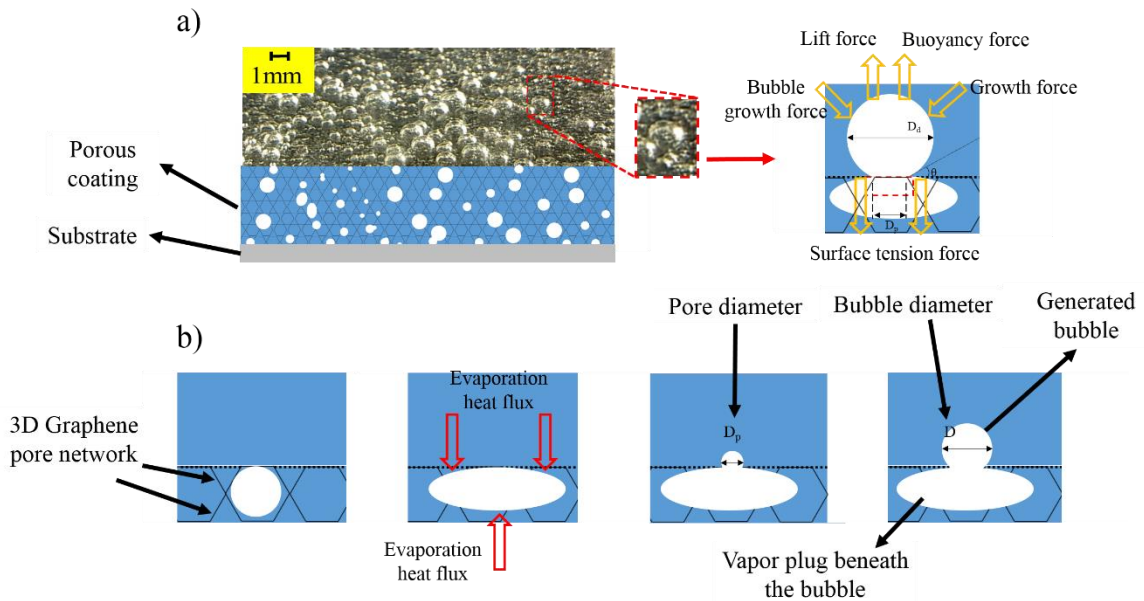


Figure 6.7 a) Bubble nucleation on graphene coated porous surface and forces acting on a bubble upon departure from a porous surface b) bubble nucleation and growth inside the porous medium

Furthermore, using visualization technique bubble departure diameter and frequencies are measured in the experiments. A detailed procedure for bubble departure diameter and frequency calculation is presented in the APPENDIX 3 [154]. The obtained bubble departure diameters and frequencies are presented in Figure 6.9c and Figure 6.9d. According to obtained results at partial nucleate boiling region the bubble departure frequency increases with graphene thickness, indicating enhancing effect of coating on surface cooling. Comparing the trends in obtained results shown in Figure 6.8c-d, it can be seen that the differences between departure frequency and bubble departure diameter for graphene coated surfaces are much lower than one of bare silicon surfaces. One of the main reasons for such a trend on coated surfaces is attributed to the interaction of active nucleation sites in porous surfaces.

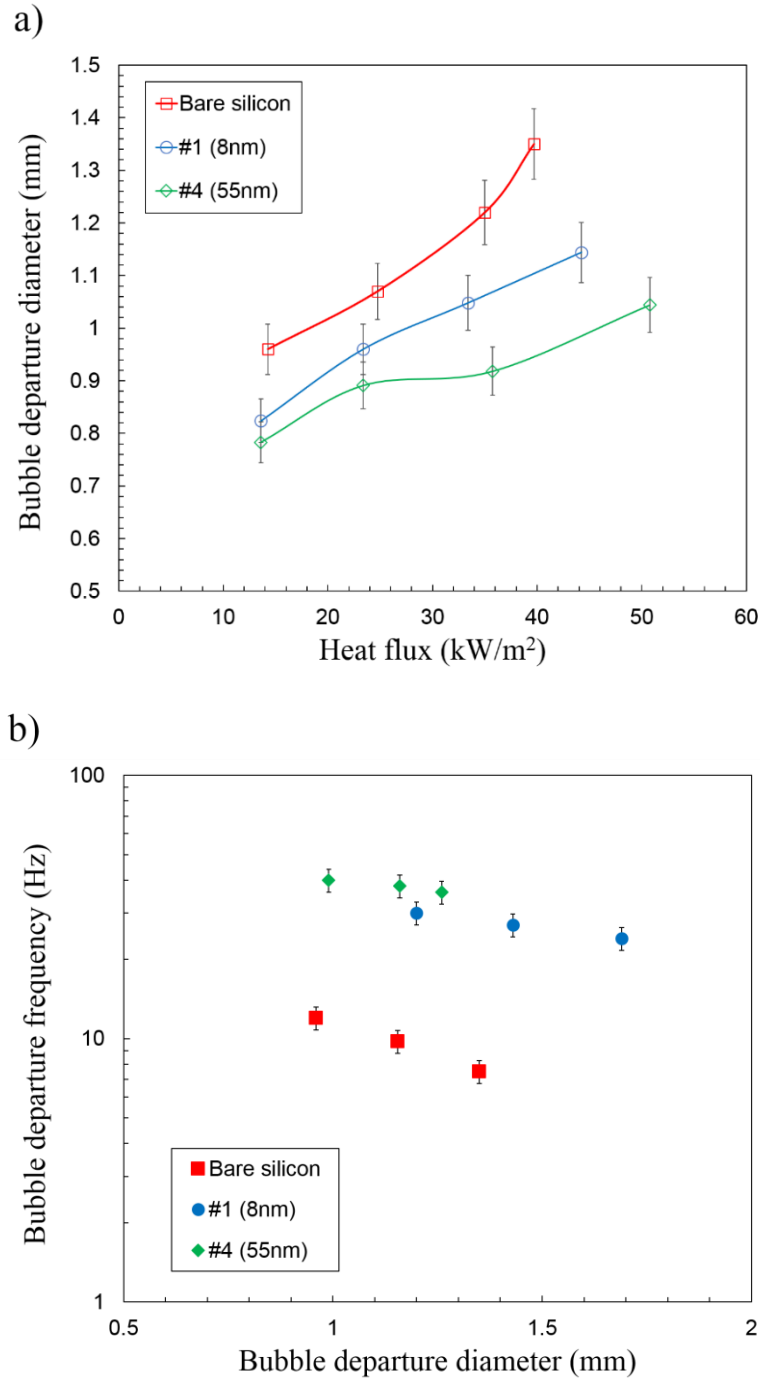


Figure 6.8 a) experimental bubble departure diameters b) experimental bubble departure frequencies for surfaces with different coating thicknesses

Although under experimental conditions for all ranges of wall heat flux, lower surface temperatures and higher heat transfer coefficients are obtained for all graphene coated samples compared to bare silicon surface (as shown in Figure 6.5b), at developed boiling region ($\Delta T_{\text{sup}} > 15 \text{ K}$) 3DG coated surfaces demonstrate a different trend comparing to partial nucleate boiling region ($\Delta T_{\text{sup}} < 15 \text{ K}$). At partial nucleate boiling region heat

transfer coefficient increases with graphene thickness. For developed boiling region it was found that heat transfer coefficient increases as graphene thickness decreases down to 13nm, where the obtained heat transfer coefficients for the 8nm sample are much lower than the ones of the 13nm sample. There are several factors attribute to different heat transfer behavior of 3D foam-like graphene coatings as disconnected-pores, vapor column size, graphene interface evaporation, and mechanical resonance of the 3D structure.

SEM images indicated that as graphene thickness decreases the amount of disconnected rods increases in the 3D branches, implying that the pore sizes increases with graphene thickness decrement. Accordingly one reason for heat transfer deterioration in 8nm thick sample could be due to bubble trapping in the porous structure. At high heat fluxes the maximum pore size is large enough to trap the bubbles and vapor blanket inside, which acts as insulator and deteriorates the heat transfer performance of the samples (Table 6-2).

The other factor affecting heat transfer mechanism in developed nucleate boiling region could be attributed to formed vapor column size within the 3D graphene structure. As the wall heat flux increases, individual bubbles form vapor layer in the coating, which characterizes the developed nucleate boiling region. Figure 6.9a shows the departure bubbles at the heat flux of 100 W/cm^2 (for sample #3). The schematic of the vapor column within the porous medium is shown in Figure 6.9b. Visualization studies reveal different vapor column formation on graphene coated samples, indicating the effect of graphene thickness. As shown in Figure 6.9c and Figure 6.9d, the coating with 55nm thick graphene structures generate smaller bubbles but more vapor columns compared to 8nm graphene coating. According to obtained results it was found that vapor column size increasers as graphene thickness decreases.

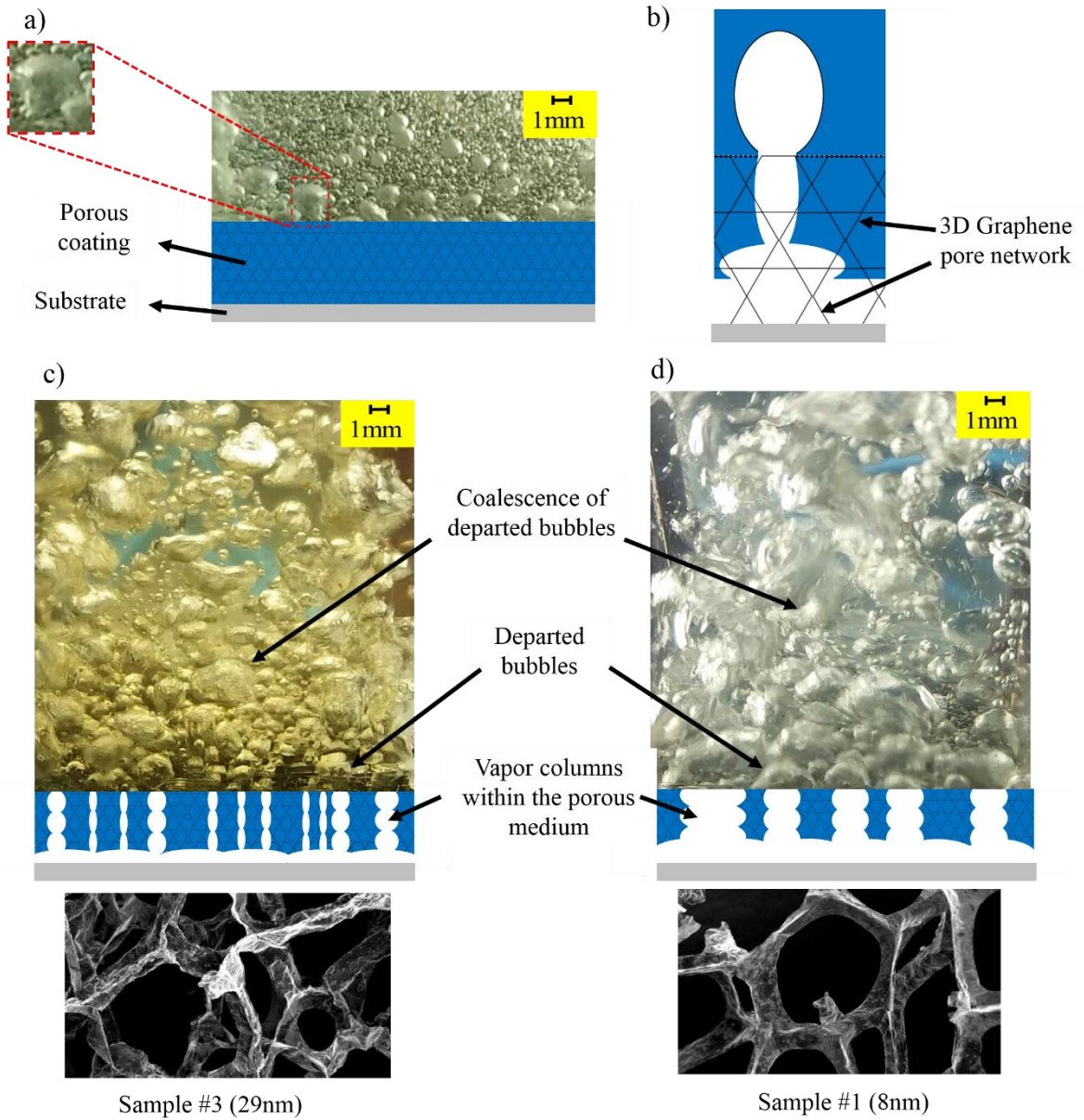


Figure 6.9 a) Schematic of the nucleate boiling on porous structure b) bubble departure initiation upon a pore

The forces acting on the vapor column in the porous medium can be determined by Bond ($Bo = \frac{\Delta\rho g a^2}{\sigma}$) and Capillary ($Ca = \frac{\eta \bar{u} a^2}{\sigma \kappa}$) (non-dimensional) numbers [155-157]. Here $\Delta\rho$, g , a , σ , η , \bar{u} , and κ are density difference between vapor and water ($\text{kg}\cdot\text{m}^{-3}$), gravity acceleration constant ($\text{m}\cdot\text{s}^{-2}$), the characteristic length (e.g., pore radius), water–vapor surface tension ($\text{N}\cdot\text{m}^{-1}$), dynamic viscosity ($\text{N}\cdot\text{s}\cdot\text{m}^{-2}$), mean fluid velocity ($\text{m}\cdot\text{s}^{-1}$), and porous medium permeability, respectively. Due to lower density, the resulting balance inside the porous medium forces the vapor phase to form vapor columns in the

saturated medium (fully developed nucleate boiling). Graphene coatings with different pore sizes have different Bond and Capillary numbers such that coating with a higher graphene coating thickness has denser and smaller pore sizes meaning lower Bond number but higher Capillary number for the corresponding coating, which leads to smaller vapor column formation.

The vapor column growth can also be analyzed based on the thermal resistance network model proposed by Ha and Graham [158], which suggests that heat transfer occurs by evaporation at the interface. The other reason for higher heat transfer coefficient corresponding to 3D coatings with thinner graphene coatings is that the evaporation in the larger interface area per volume enhances the heat transfer performance of such coatings. As expected, at high heat fluxes, the graphene coating raises the bubble departure frequency. Weak van der Waals forces between graphene layers enable graphene layers to slide easily, and give flexibility to the structure. The resulted mechanical resonance due to bubbling effect within the porous medium, and reaction force of departed bubble on the coating surface may change to heat transfer enhancement mechanism in foam-like graphene coating. Observed different bubble departure angles, and bubble coalescence shapes on coated surfaces with different graphene thicknesses could be attributed to the mechanical resonance for the 3D structure. The effect of graphene coating on bubble departure process is shown in Figure 6.10. At high heat fluxes, the graphene coating raises the bubble departure frequency. Smaller bubbles depart from the surface, while higher concentration of coalesced bubbles is visible.

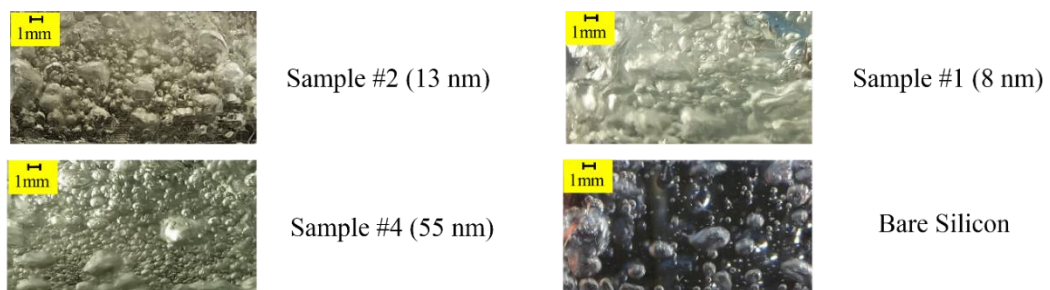


Figure 6.10 Generated bubbles for different coatings and bare silicon surfaces at the heat flux of 90 kW/m².

6.4 Conclusion

This study presents pool boiling experiments conducted on CVD grown 3D foam-like graphene coated surfaces to show the effect of graphene coating thickness on the pool boiling heat transfer performance. According to the obtained results, 3D structure of the coating has a significant effect on pool boiling heat transfer mechanism. Factors such as pore shape and mechanical resonance of the 3D structure could be possible reasons for bubbling behavior in developed nucleate boiling. Furthermore it was found that there exists an optimum thickness of 3D graphene coatings, where the maximum heat transfer coefficient were achieved. This is mainly due to the trapped bubbles inside the porous medium, which affects the bubble dynamics involving bubble departure diameter and frequency. The results reveal that the facile method of producing 3D foam like graphene coatings can be used as an effective alternative for boiling heat transfer enhancement.

7. Bio-coating

7.1 Introduction

In this chapter, a novel bio-coating is proposed for enhancing boiling heat transfer and critical heat flux via an athermophilic archaeon. Archaea are known as one of the three main domains of life and are divided into five phyla [159, 160]. Archaeon cells characteristics similar to eubacteria, including unicellular morphology. They have a circular chromosome and resemble eukaryotic cells due to having metabolisms involving DNA replication and transcription [161, 162]. Most strikingly, archaeal cells have very unique mechanisms that keep them alive under physiologically harsh conditions, such as low or high temperatures ($-2-15^{\circ}\text{C}$ or $60-122^{\circ}\text{C}$), high salinity (2–5 M NaCl) and low or high pH (<4 or >9) [163-165].

Crenarchaeon *Sulfolobus solfataricus* P2 was used as coating material to investigate the effect of coating, and coating thickness on BHF and CHF. Pool boiling experiments were conducted on silicon surfaces that were coated with different coating thicknesses of thermophilic archaeon. Two solutions containing different poly-L-lysine:archaeon ratios (1:2.5 and 1:5) were used for coating the silicon samples, leading to an archaeon layer thicknesses of 1 and 2 μm respectively. All of the experiments were done with deionized water under atmospheric conditions.

7.2 Sample preparation and characterization

A hyperthermophilic archaeon called *S. solfataricus* belongs to the Crenarchaeota phylum and was first isolated in Italy by Pisciarelli Solfatara [166]. *S. solfataricus* is an irregular and lobe-shaped archaeon having a size in the range of 0.2–2 μm , grows optimally at $80-85^{\circ}\text{C}$, has a pH of ~ 3 (while maintaining an intracellular pH of ~ 6.5), and can utilize variable carbon sources to maintain cellular homeostasis [167]. This robust

and heat-resistant microorganism is a good candidate for providing organic porous coatings for energy saving and efficiency in an economical, facile, and environmentally friendly fashion, which constitutes the motivation behind this method.

The methods used for crenarchaeon *S. solfataricus* P2 preparation and the coating process are summarized in Figure 7.1. The biocoated surfaces were produced on 500 μm thick silicon wafer substrates with the heat cure method, which is cheap and easy compared to other coating methods. In order to ensure the repeatability of the examined surfaces, samples were characterized before and after each experiment. Coated surface structures were analyzed and characterized using scanning electron microscope (SEM) techniques. Cavity size, shape, range, and distribution along the surfaces were obtained using the 2-D and 3-D surface profilometer technique.

S. solfataricus is one of the hyperthermophilic and acidophilic archaea and could be a good model for temperature dependent phenomena such as cooling. For this purpose, *S. solfataricus* P2, was grown in a batch culture under mild agitation at 80°C, pH 3. Basal salt and modified Allen media [168] were used to obtain optimal growth. However, as the salt medium is based on minimal media containing only minerals as a carbon source, it was supplemented with different concentrations of sucrose (0.5, 2, or 5 g/L) with 0.2 % (w/v) tryptone. Stock cultures were maintained in 2 g sucrose/L and 100 g glycerol/L. Cells from -80°C stocks were inoculated into 50 mL fresh culture medium. After 24 h of propagation, the cell culture was transferred to 500 mL of the pre-heated media. Cell growth was then monitored with a UV Spectrophotometer at 600 nm every 24 h until 96 h. A 1-ml sample of cells was pelleted at 4000 g for 5 min and then re-suspended in 500 μl of 4 % (v/v) PFA (paraformaldehyde) for 20 min, followed by permeabilization with 0.1% (v/v) Triton X-100 at RT for 5 min. Fixed and permeabilized cells were washed twice with PBS (phosphate buffer saline) buffer and spread on poly-L-lysine coated cover slides. After air-drying, cells were stained with DAPI (4',6-diamidino-2-phenylindole, 10 μM). The cover slides were then mounted and inspected under 40X magnification using a BX60 fluorescence microscope (Olympus, BX60, Japan).

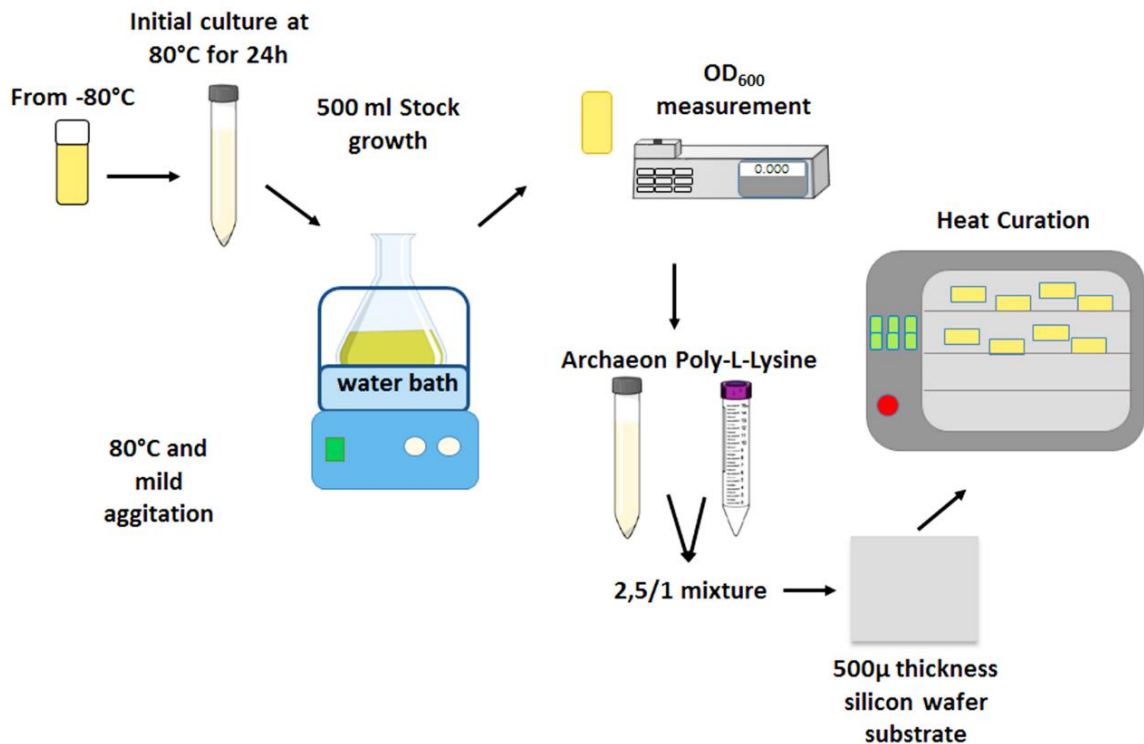


Figure 7.1 preparation and the coating process of crenarchaeon *S. solfataricus* P2

A scanning electron microscope (FEG-SEM Leo Supra 35, Oberkochen, Germany) was used to obtain the microstructural images of the specimen surfaces before and after treatment. One particularly useful imaging method involves collecting low energy secondary electron (SE) signals that originate within a few nanometers from the specimen surface. Due to this process, the SE method allows imaging of the surface with a high spatial resolution. The micrographs were collected using the SE mode at a low voltage (2 KV) within different tilts to allow for the full imaging of the surface area and cross sectional area. The wettability of the biocoated surfaces was tested using the WCA (water contact angle) method. The sessile drop method was used to measure the CA (contact angle) by dispensing a 5 μL water drop, and the average CA from five different positions on each sample was taken into consideration. The dynamic contact angles were measured by holding the water drop with a stationary needle in contact with the surface and moving the goniometer stage along one direction. The surfaces were tilted at an angle of 25° relative to the horizontal direction. To check whether the angles were the true advancing and receding angles, the surface was further tilted to 50° . The angles remained nearly unchanged, implying that these were representatives of the advancing and receding contact angles

Figure 7.2 a, Figure 7.2b, and Figure 7.2c show the 2D surface profile, cavity size distribution, and 3D surface profile, respectively, of a 2- μm thick coated sample. As can be seen, large colonies with structures of a minimum height of 1 μm are located separately with distances of up to 100 μm , creating a nano-micro interconnected porous medium (Figure 7.3). Cavity size distribution (Figure 7.2b) indicates that more than 60% of the surface is coated with large colonies with sizes bigger than 4 μm . Static contact angle measurements of silicon wafer and biocoated silicon wafer are presented in Figure 2d. Accordingly, surfaces with bio-coatings have a higher wettability. On the other hand, dynamic contact angle measurements on the bare, 1 μm , and 2 μm coated surfaces revealed receding contact angles of 42°, 22°, and 5°, respectively. This highlights the pronounced wetting behavior of the coated surfaces in boiling, especially prior to the CHF condition. The porous nano-micro structures provided by such bio-coatings offer separate channels to intensify wicking flows through the media. The interconnected porous media are responsible for the lower contact angle followed by higher surface wettability, which also generates capillary motion within the pores of such structures. This observation agrees with the data reported by Singh et al. [169] and Das et al. [170].

Archaeon cultures ($\text{OD}_{600} = 1$, after ~ 72 h incubation) were cooled down on ice, then centrifuged for 15 min at 4000 g and washed twice with ice-cold phosphate buffer. The pellets were then resuspended in 5 mL PBS (0.1 g/mL), and 2.5 mL of this solution was mixed with 1 mL poly-L-Lysine (0.01 % (w/v) in H_2O) to cover a 500 μm thick silicon wafer substrate with the heat cure method. Crenarchaeon were cultured in a minimum salt solution including different amounts of sucrose (0.5, 2, 5 g/L) at 80°C, pH 3. Time-dependent growth was analyzed based on optical density at a wavelength of 600 nm using a spectrophotometer. A more stable growth was obtained in the medium that was supplemented with 2 g/L sucrose, and all of the subsequent experiments were performed using the same growth conditions. *Sulfolobus* species have been known to form aggregates under certain conditions such as UV treatment [171]. According to microscopy examinations, the archaeon was found mostly in the aggregated form (72 h, 2 g/L sucrose), with the aggregates covering 20–30 % of the surface (Figure 7.2f).

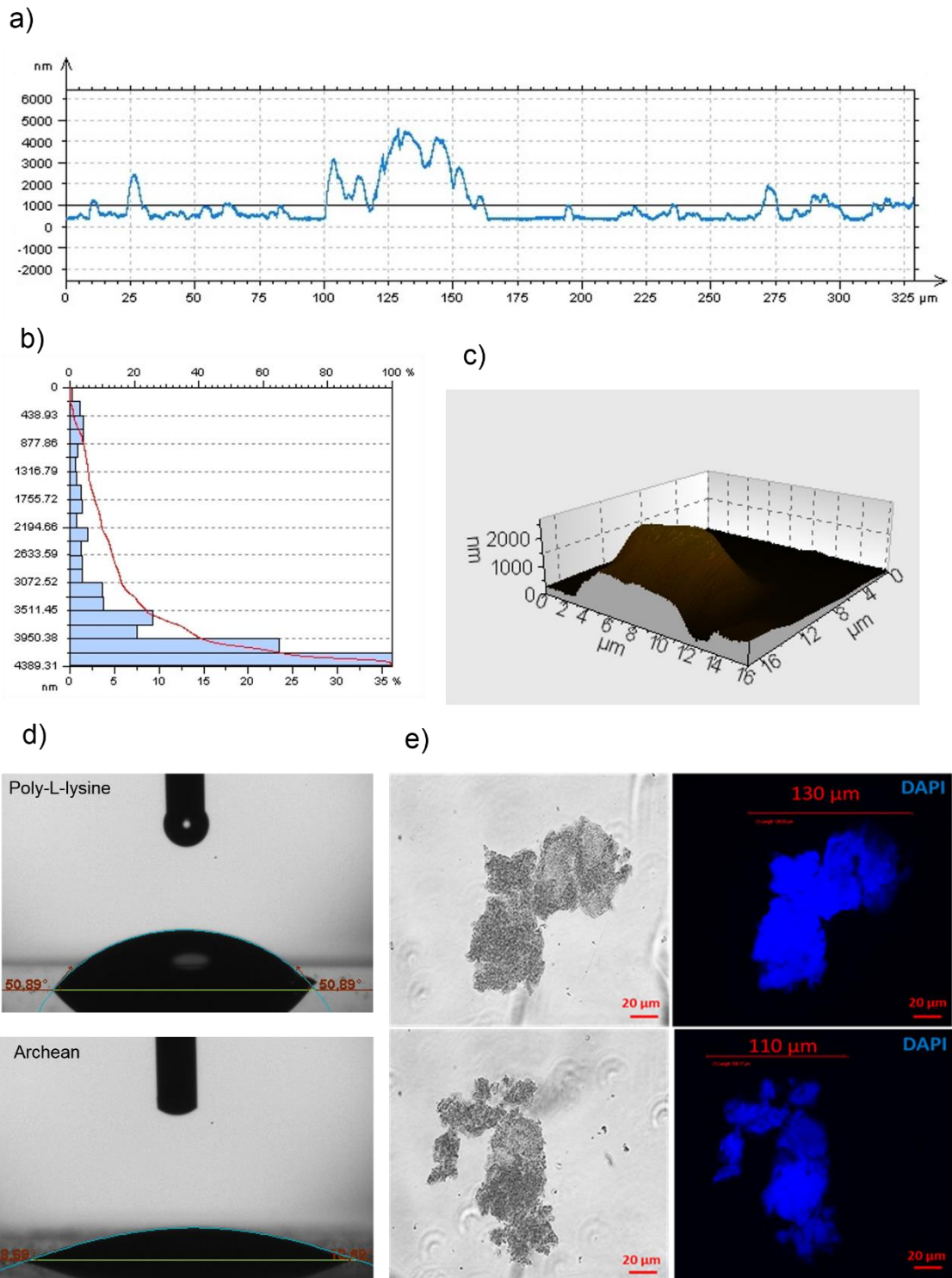


Figure 7.2 (a) 2D surface profile (b) Cavity size distribution (c) 3D surface profile of a cavity of $\sim 2 \mu\text{m}$ thick coating. (d) Water contact angle measurement (e) Fluorescence micrograph of cellular structures from crenarchaeon. DNA stained by DAPI (blue). (f) SEM images of the coated surface showing surface porosity.

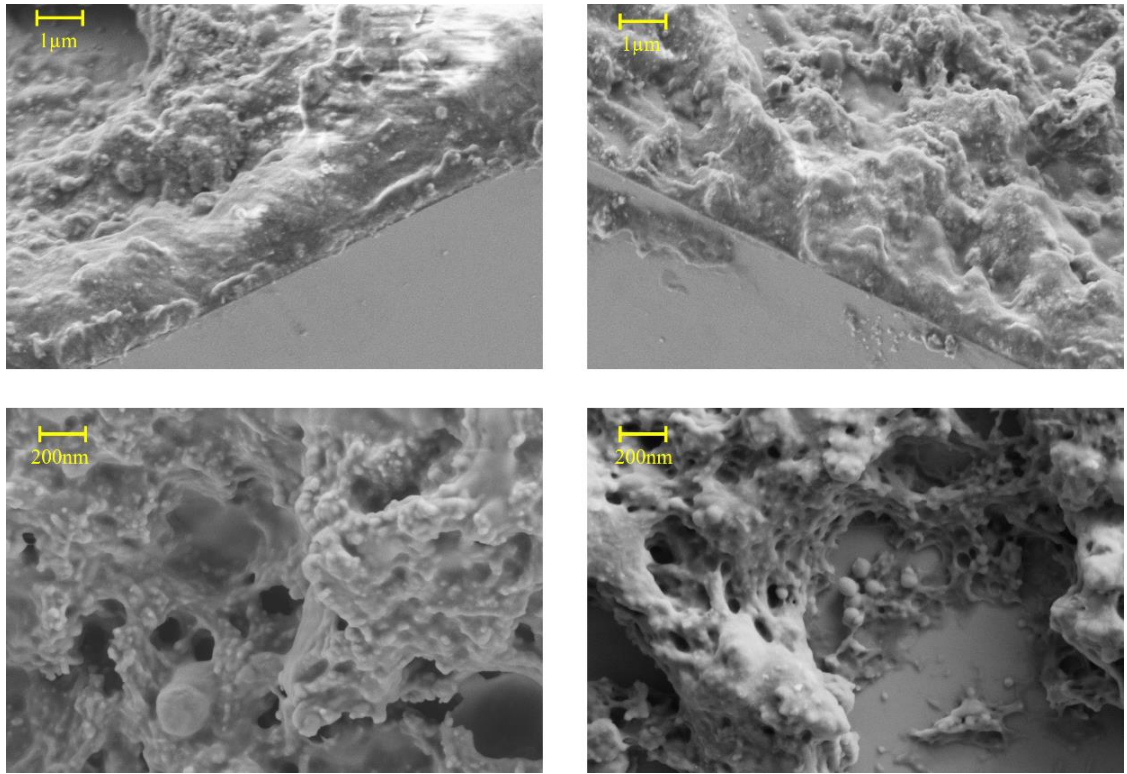


Figure 7.3 SEM images of biocoated surfaces

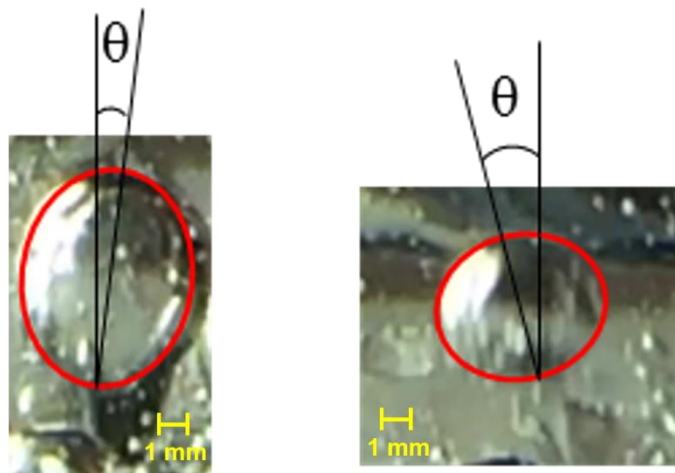
7.3 Discussion

As mentioned in the previous section, poly-L-lysine was used to increase the adhesion of biocoating to silicon surface during the transformation process. To ensure the independency of obtained results from the adhesion layer, pool boiling experiments were performed on poly-L-lysine coated surfaces. Accordingly no significant difference was observed between obtained results of bare silicon surface and those of poly-L-lysine coated surface. *S. solfataricus* coatings with two different thicknesses were used to investigate the effect of biocoating thickness on boiling heat transfer.

The structure of *S. Solfataricus* coating enhances the bubble nucleation and departure processes by providing more active nucleation sites on the surface, and bubble merging mechanism through the pores. Using a high speed camera (250 fps) nucleated and departed bubbles on the biocoating were examined. Due to nature of porous structure, unlike low heat fluxes ($q'' < 30 \text{ W/cm}^2$) – where departed bubbles are mostly spherical – at high heat fluxes bubbles leave the superheated surface with an inclined angle. This makes it difficult to measure the bubble departure diameter at high heat fluxes. As a

results it was assumed that the departed bubbles have ellipsoidal shapes, as shown in Figure 7.6a, and instead of bubble departure diameter, bubble departure volume is considered as the parameter for comparison between tested samples. Accordingly, it was found that the bubble departure volume decreases on the coated surfaces in comparison to bare silicon surface. The obtained results are shown in Figure 7.6b. For example at wall heat flux of 56 W/cm^2 the bubble departure volume (corresponding departure frequency) on silicon, $1\mu\text{m}$, and $2\mu\text{m}$ biocoated surfaces are $\sim 29\text{mm}^3$ ($\sim 7.5\text{Hz}$), $\sim 8\text{mm}^3$ ($\sim 33\text{Hz}$), and $\sim 7\text{mm}^3$ ($\sim 38\text{Hz}$), respectively. One of the main reasons for the difference in bubble departure frequency and departure diameter between biocoated and uncoated surfaces is the presence of porous layer and the bubble departure mechanism prior to the departure process [197]

a)



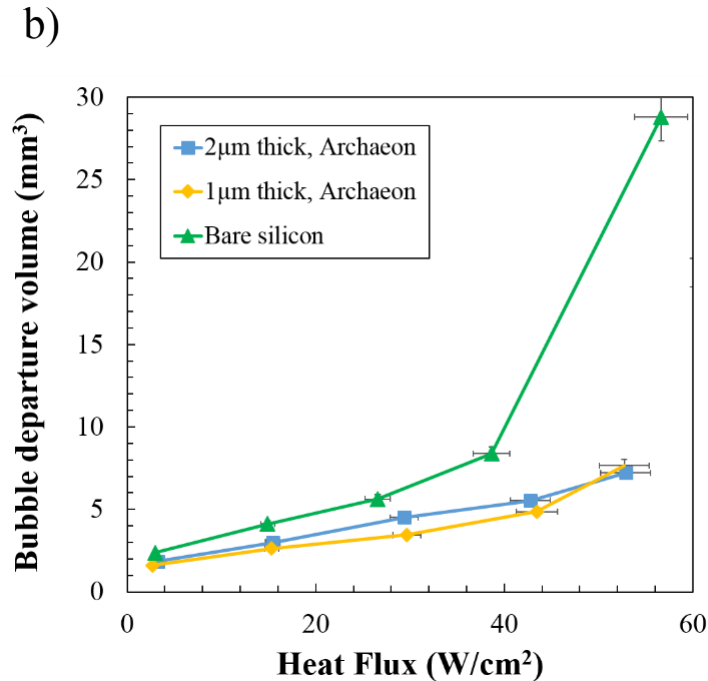


Figure 7.4 a) departed bubble with non-spherical shape form biocoated surface at wall heat flux of 50W/cm² b) bubble departure diameter on tested samples at low and moderate heat fluxes

Figure 7.5a shows the obtained wall superheat – heat flux diagrams for testes samples. Accordingly, at a constant wall heat flux, coated surfaces have much lower wall superheats, indicating the superior cooling performance of the proposed coatings. The coated surfaces enhance the boiling heat transfer by increasing the number of nucleation sites. The presence of numerous nucleation sites on coated surfaces with different sizes facilitate the inception of boiling on biocoated surfaces. As a result lower wall temperatures are required for onset of nucleate boiling on these surfaces, as can be seen in Figure 7.5a.

The heat transfer coefficient profiles are shown in Figure 7.5b. The obtained HTC's from biocoated surfaces are much higher than those of bare silicon surface. Comparing to untreated surface, coated surfaces with average 1µm and 2µm thicknesses offer 94% and 126% enhancement in boiling heat transfer coefficient, respectively. These results show that the *S. solfataricus* alter the surface morphology and causing better boiling heat removal. While chemical surface treatments are severely toxic, such bio-coatings are suitable candidates to change surface structures in an environmental friendly and biocompatible fashion.

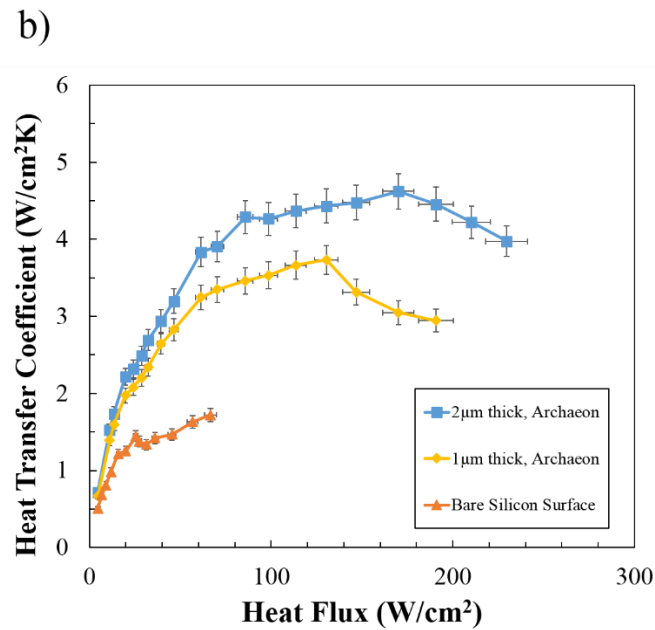
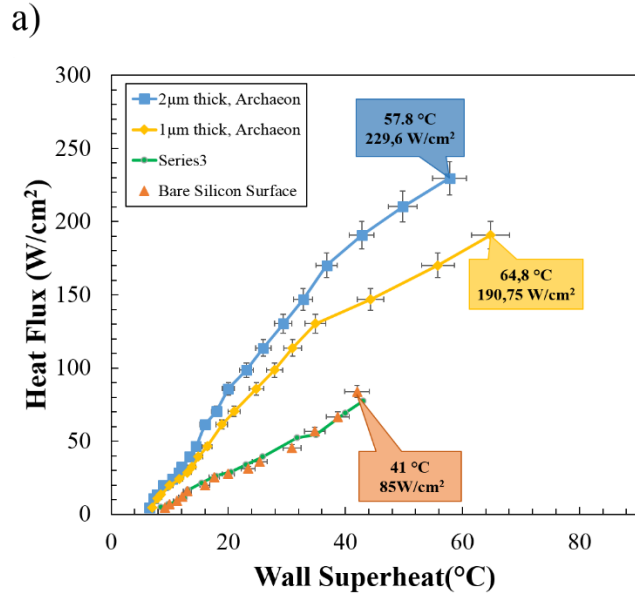


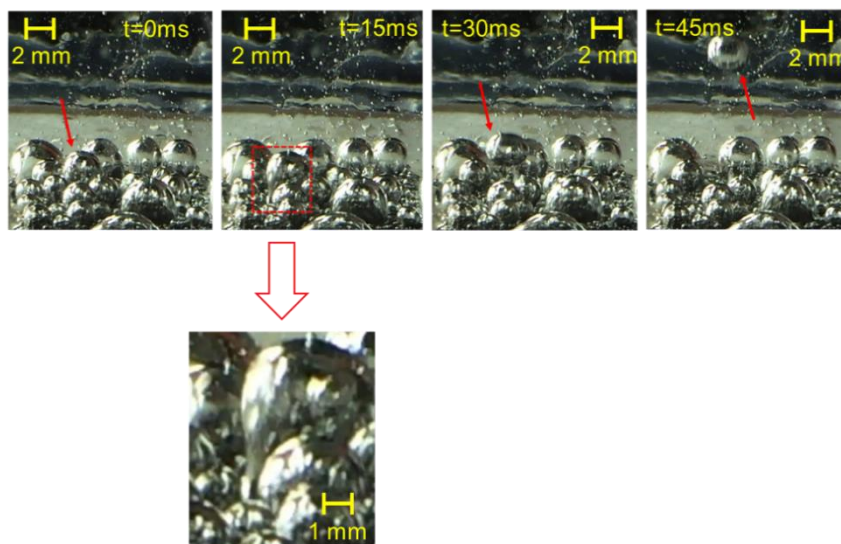
Figure 7.5 a) Boiling curves b) obtained heat transfer coefficients on tested samples

The superior heat transfer performance on the biocoated surfaces is mainly attributed to the morphology of the coated surfaces. As shown in Figure 7.3, biocoated surfaces have porous structure with pore sizes ranging from 100nm to 2µm, acting as nucleation sites. These structures, and the interaction between these pores facilitates onset of nucleation boiling, and enhance the boiling heat transfer. This can be seen in Figure 5.6 demonstrating numerous nucleated bubbles from these sites on biocoated surfaces compared to uncoated sample. Due to physical structure of the coating, nucleation sites are separated via In addition, the presence of such porous structure enhances the surface

rewetting after bubble departure, resulting in better heat transfer. The surface replenishment effect is more prominent at high heat fluxes. The presence of porous structure with such variable pore size has a considerable effect on surface wetting through the coating. The interrelated porous form micro-channels which assist liquid-transportation between pores, resulting in surface dryout delay [184].

Capillary pumping is another mechanism that has a considerable effect on surface rewetting by providing liquid flow to dry spots. In other words, capillary flow reduces liquid-vapor counter flow resistance by providing a flow path for liquid and vapor, and preventing the dry-out condition [185]. In the literature [186], a method was reported to release trapped vapor in a porous layer by adding vapor channels, offering paths for the escaping vapor. It can thus be hypothesized that the colonial structure of the archaeon porous layer can provide separate vapor channels. These channels can release trapped vapor at the bottom of the porous layer, thereby delaying the CHF condition. Electron microscopy and surface profile images (Figure 7.2 and Figure 7.3) indicate that the crenarchaeon coatings are distributed over the surface like separate colonies with a minimum size of 1 μm . The distance between these colonies are coated with layers of archaeon acting as channels for vapor venting inside the porous layers. These channels not only remove the vapor layer at the bottom of the porous structure but also separate the vapor and liquid path flow, another reason for the enhancement of the CHF and HTC [186].

a)



b)

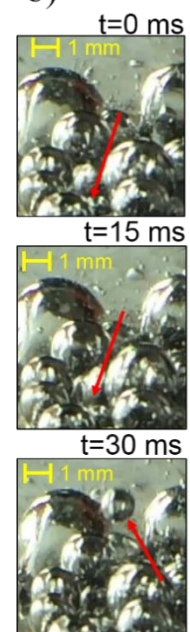


Figure 7.6 a) inclined departed bubble b) isolated bubble in nucleate boiling region

The CHF location and the corresponding wall superheat were labeled for each sample (Figure 7.5). For all of the bare and crenarchaeon-coated surfaces, the HTC increased with heat flux until the CHF point. The CHF of the bare silicon surface was measured as 85 W/cm^2 (with a corresponding wall superheat of 41°C), while the CHF of biocoated surfaces reached 190.75 W/cm^2 (with a corresponding wall superheat of 64.8°C) and 229.16 W/cm^2 (corresponding wall superheat of 57.8°C) for surfaces with the coating thicknesses of $1 \mu\text{m}$ and $2 \mu\text{m}$, respectively. Taken together, the results show that CHF increases with crenarchaeon coating thickness.

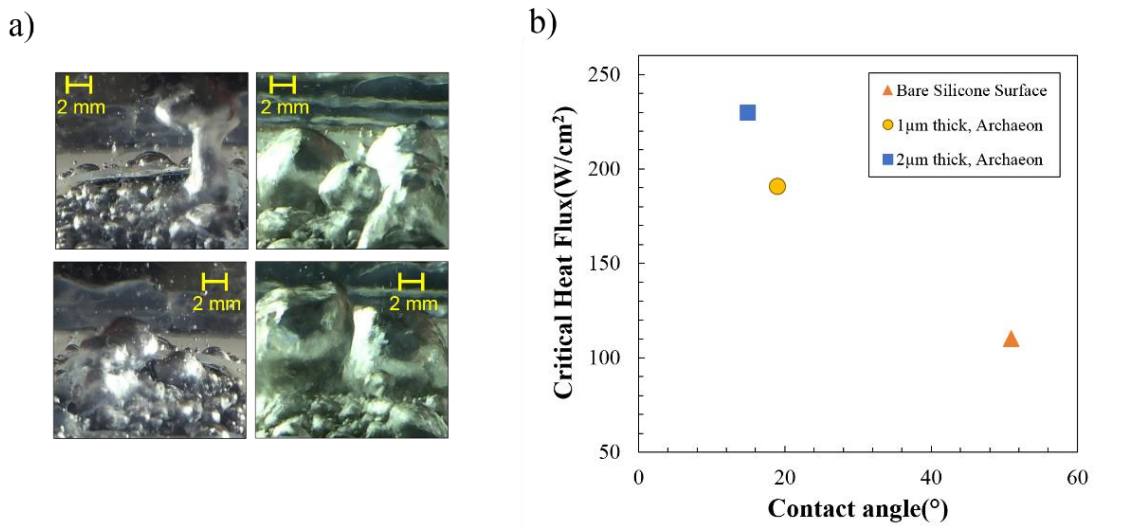


Figure 7.7 a) Formed vapor columns on silicon (right) and biocoated (left) surfaces prior to dryout condition b) CHF values on tested samples

7.4 Conclusion

A novel coating, crenarchaeon *Sulfolobus solfataricus* P2 biocoatings, were proposed for the performance enhancement of heating and cooling devices, thermofluidic systems, batteries, and micro- and nanofluidic devices. These biocoatings have the potential for addressing high heat removal requirements in many applications involving heat and fluid flows. Pool boiling experiments were performed on biocoated surfaces with thicknesses of $1 \mu\text{m}$ and $2 \mu\text{m}$. The obtained results indicated that biocoated surfaces enhance boiling heat transfer by providing numerous nucleation site densities and by increasing bubble interaction on the superheated surface. Interconnected channels inside the porous coating,

and capillary pumping enhance liquid transportation and reduce the liquid-vapor counter flow resistance, thereby delaying CHF condition.

Part 4: Conclusion remarks and outputs

8. Conclusion, contribution and future works

8.1 Introduction

In the final chapter of this thesis, the achieved objectives are highlighted and briefly explained. Finally recommendations for future research activities in pool boiling on engineered surfaces are summarized.

8.2 Main objectives and findings

Parametric studies were carried out on engineered surfaces to investigate the effects of nucleation site diameter and pitch size, mixed wettability, and nanocoatings on boiling heat transfer and critical heat flux. Different types of surfaces were fabricated and examined under different operating conditions such as surface inclination angles, surface wettabilities, and wall heat fluxes. Boiling heat transfer, bubble dynamics and CHF mechanisms were analyzed. The main objectives achieved are summarized as follows:

- A Comprehensive literature review of existing boiling heat transfer and CHF mechanisms, as well as engineered surfaces including microstructured surfaces, nanostructured surfaces, and nanocoated surfaces are presented. To fill the gap in the literature, five different types of engineered surfaces were fabricated and tested.
- Fundamentals, technology, innovation, and application were aspects that were aimed to be covered in the studies presented. Fundamentals of pool boiling were investigated using three parametric studies on biphilic surfaces, surfaces with artificial cavities, and nano-coated surfaces. MEMS techniques such as lithography, dry etching, wet etching, chemical vapor deposition, and evaporation were used for fabrication of test samples. The applicability of the fabricated samples were tested by applying the proposed technique to a commercial refrigerator as a real life application.

- An experimental setup was built to perform pool boiling experiments. Several modifications were introduced to the experimental setup to improve the errors and uncertainties of experimental parameters such as temperature. To calculate the effective heat flow to the pool, the thermal losses were identified and calibration correlations were developed. The experimental setup was validated by comparing the obtained results and three different mostly used correlations in the literature.
- Five novel surface structures were introduced with acceptable complexity to perform parametric and mechanistic studies on pool boiling. Surfaces with artificial cavities, biphilic surfaces with different hydrophobic/total surface area, temperature responsive pHEMA coated surfaces, graphene coated surfaces, and *Sulfolobus solfataricus* P2 bio-coatings were fabricated and tested in the experimental facility.
- Hydrophobic artificial cavities – Inception of bubble nucleation strongly depends on cavity properties. Activated nucleation sites continue to generate bubbles until CHF occurs. In my latest research, we examined hydrophobic surfaces (Teflon coated) with artificial cavities (act as bubble nucleation sites) to examine the dual effect of surface wettability and nucleation site on boiling heat transfer and CHF mechanism. We found that local dryout (bubble crowding) was the main mechanism for CHF occurrence on hydrophobic artificial cavities, where Kelvin-Helmholtz instability at the interface of emerging upward vapor flow and downward liquid flow was the main mechanism responsible for CHF and liquid flow (rewetting) blockage on hydrophilic surfaces.
- Biphilic surfaces – Mixed wettability alters surface rewetting under high vapor quality conditions. We performed a parametric study on boiling performance of biphilic surfaces with mixed superhydrophobic (nanograss) and hydrophilic (SiO₂) areas. It was revealed that boiling inception takes place at the contact line separating superhydrophobic and hydrophilic areas. Furthermore, horizontal bubble coalescence on fabricated surfaces was the main mechanism for increasing bubble departure frequency and heat transfer enhancement. We found the same optimal ratios of surface areas for maximum boiling heat transfer and CHF, which indicates the importance of interfacial momentum exchange between liquid and vapor phases on biphilic surfaces.
- pHEMA/pPFDA coatings – Polymer film coating is a method for wettability alteration. Especially, stimuli-responsive polymers and hydrogels such as thermo-responsive polymers have been widely used for boiling heat transfer enhancement. In

a study we performed boiling experiments on pHEMA/pPFDA polymeric network. Temperature-responsive swelling behavior of pHEMA provides a gradient wettability for the coating, enhances bubble manipulation and surface rewetting. Attached bubbles move on the coating network, act as bubble venting mechanism and enhance surface cooling.

- 3D graphene –Bubble growth strongly depends on the micro layer evaporation and thermal condition surrounding the bubble. The idea of 3D graphene foam coating for enhancing pool boiling came from its high thermal conductivity and porous structure (due to low Bond number the coating acts like a micropump) to enhance bubble growth rate, and vapor venting, respectively. Interestingly, we found that the mechanical resonance of the 3D structure could contribute to the liquid transport and bubble departure process. From the obtained result we proposed a new type of coating and mechanism for heat pipe applications.
- Sulfolobus Solfataricus P2 Bio-coating – Most of the proposed techniques in the thermal-fluid industry such as microstructured surfaces and spray coating are not cost effective, scalable, and suitable for closed geometries. We proposed a novel bio-coating material, Sulfolobus Solfataricus P2, which is a thermophilic archaeon, for boiling heat transfer enhancement. Sulfolobus creates a porous media with pore sizes ranging from 0.1 to 0.5 μm , and thickness ranging from 0.1 to 5 μm . Unique structure of the coating provides interconnected channels for liquid transportation and vapor venting.

8.3 Recommendations for future work

Within scope of this thesis several important aspects of pool boiling on enhanced surfaces have been fulfilled. However, these studies generate research questions, which needs to be investigated.

- Onset on nucleate boiling (ONB): Further investigations on the minimum temperature for activation of nucleation sites on enhanced surfaces such as hydrophobic channeled surfaces are required using precise temperature acquisition systems for design of such surfaces.

- The temperature distribution beneath the growing bubbles on enhanced surfaces can be helpful for understanding of heat transfer mechanisms during the bubble growth attributed to different surface modification techniques.
- Although one of the major focuses of this dissertation was to investigate the bubble dynamics during the growth and departure periods, visualization studies suitable for investigation of nucleation, growth and departure of single/double bubble(s) would be beneficial for further investigation of behavior of triple line on engineered surface.
- CHF: Considered as the most important limit of boiling heat transfer, further investigations are required to study the possible mechanisms responsible for CHF occurrence on engineered surfaces. High speed visualizations in parallel with precise temperature measurements could be helpful for detection of vapor shape (and corresponding surface temperature) and behavior near the superheated surface responsible for sudden temperature rise.

Bibliography

1. Thome, J.R., *Boiling in microchannels: a review of experiment and theory*. International Journal of Heat and Fluid Flow, 2004. **25**(2): p. 128-139.
2. Incropera, F.P., *Liquid cooling of electronic devices by single-phase convection*. Vol. 3. 1999: Wiley-Interscience.
3. Kim, J., *Spray cooling heat transfer: the state of the art*. International Journal of Heat and Fluid Flow, 2007. **28**(4): p. 753-767.
4. Zhou, D., C.-Y. Zhao, and Y. Tian, *Review on thermal energy storage with phase change materials (PCMs) in building applications*. Applied energy, 2012. **92**: p. 593-605.
5. Kandasamy, R., X.-Q. Wang, and A.S. Mujumdar, *Transient cooling of electronics using phase change material (PCM)-based heat sinks*. Applied Thermal Engineering, 2008. **28**(8): p. 1047-1057.
6. Sadaghiani, A.K., et al., *Boiling heat transfer performance enhancement using micro and nano structured surfaces for high heat flux electronics cooling systems*. Applied Thermal Engineering, 2017. **127**: p. 484-498.
7. Collier, J.G. and J.R. Thome, *Convective boiling and condensation*. 1994: Clarendon Press.
8. Nikolayev, V., et al., *Experimental evidence of the vapor recoil mechanism in the boiling crisis*. Physical review letters, 2006. **97**(18): p. 184503.
9. Şişman, Y., et al., *Subcooled flow boiling over microstructured plates in rectangular minichannels*. Nanoscale and Microscale Thermophysical Engineering, 2016. **20**(3-4): p. 173-190.
10. Ramişon, J.M. and J. Lienhard, *Transition boiling heat transfer and the film transition regime*. Journal of heat transfer, 1987. **109**(3): p. 746-752.
11. Luke, A., *Pool boiling heat transfer from horizontal tubes with different surface roughness*. International journal of refrigeration, 1997. **20**(8): p. 561-574.
12. Sadaghiani, A.K., et al., *Pool Boiling Heat Transfer Characteristics of Inclined pHEMA-Coated Surfaces*. Journal of Heat Transfer, 2017. **139**(11): p. 111501.

13. Sadaghiani, A.K., M. Yildiz, and A. Koşar, *Numerical modeling of convective heat transfer of thermally developing nanofluid flows in a horizontal microtube*. International Journal of Thermal Sciences, 2016. **109**: p. 54-69.
14. Esmaeilzadeh, E., et al., *Study on heat transfer and friction factor characteristics of γ -Al₂O₃/water through circular tube with twisted tape inserts with different thicknesses*. International Journal of Thermal Sciences, 2014. **82**: p. 72-83.
15. Chu, K.-H., R. Enright, and E.N. Wang, *Structured surfaces for enhanced pool boiling heat transfer*. Applied Physics Letters, 2012. **100**(24): p. 241603.
16. Ahn, H.S., et al., *Pool boiling CHF enhancement by micro/nanoscale modification of zircaloy-4 surface*. Nuclear Engineering and Design, 2010. **240**(10): p. 3350-3360.
17. Kandlikar, S., *Controlling bubble motion over heated surface through evaporation momentum force to enhance pool boiling heat transfer*. Applied Physics Letters, 2013. **102**(5): p. 051611.
18. Motezakker, A.R., et al., *Surface modifications for phase change cooling applications via crenarchaeon *Sulfolobus solfataricus* P2 bio-coatings*. Scientific Reports, 2017. **7**(1): p. 17891.
19. Motezakker, A.R., et al., *Surface modifications for phase change cooling applications via crenarchaeon *Sulfolobus solfataricus* P2 bio-coatings*. 2017. **7**(1): p. 17891.
20. Sadaghiani, A.K., et al., *Foamlike 3D graphene coatings for cooling systems involving phase change*. 2018. **3**(3): p. 2804-2811.
21. Sadaghiani, A.K., et al., *Pool boiling heat transfer characteristics of inclined pHEMA-coated surfaces*. 2017. **139**(11): p. 111501.
22. Motezakker, A.R., et al., *Optimum ratio of hydrophobic to hydrophilic areas of biphilic surfaces in thermal fluid systems involving boiling*. 2019. **135**: p. 164-174.
23. Hendricks, T.J., et al., *Enhancement of pool-boiling heat transfer using nanostructured surfaces on aluminum and copper*. International Journal of Heat and Mass Transfer, 2010. **53**(15): p. 3357-3365.
24. Li, C., et al., *Nanostructured copper interfaces for enhanced boiling*. small, 2008. **4**(8): p. 1084-1088.

25. Şişman, Y., et al., *Subcooled Flow Boiling Over Microstructured Plates in Rectangular Minichannels*. *Nanoscale and Microscale Thermophysical Engineering*, 2016(just-accepted).
26. Kim, J.J.I.J.o.M.F., *Review of nucleate pool boiling bubble heat transfer mechanisms*. 2009. **35**(12): p. 1067-1076.
27. Liang, G. and I. Mudawar, *Pool boiling critical heat flux (CHF)–Part I: Review of mechanisms, models, and correlations*. *International Journal of Heat and Mass Transfer*, 2018. **117**: p. 1352-1367.
28. Zuber, N., *On the stability of boiling heat transfer*. *Trans. Am. Soc. Mech. Engrs.*, 1958. **80**.
29. Zuber, N., *Hydrodynamic aspects of boiling heat transfer (thesis)*. 1959, Ramo-Wooldridge Corp., Los Angeles, CA (United States); Univ. of California, Los Angeles, CA (United States).
30. Bang, I.C., S.H. Chang, and W.-P. Baek, *Visualization of a principle mechanism of critical heat flux in pool boiling*. *International journal of heat and mass transfer*, 2005. **48**(25-26): p. 5371-5385.
31. Yagov, V., *A physical model and calculation formula for critical heat fluxes with nucleate pool boiling of liquids*. *Thermal Engineering*, 1988. **35**(6): p. 333-339.
32. Honda, H., H. Takamastu, and J. Wei, *Enhanced boiling of FC-72 on silicon chips with micro-pin-fins and submicron-scale roughness*. *Journal of heat transfer*, 2002. **124**(2): p. 383-390.
33. Wei, J. and H. Honda, *Effects of fin geometry on boiling heat transfer from silicon chips with micro-pin-fins immersed in FC-72*. *International journal of heat and mass transfer*, 2003. **46**(21): p. 4059-4070.
34. Mitrovic, J. and F. Hartmann, *A new microstructure for pool boiling*. *Superlattices and Microstructures*, 2004. **35**(3-6): p. 617-628.
35. Mitrovic, J., *How to create an efficient surface for nucleate boiling?* *International Journal of Thermal Sciences*, 2006. **45**(1): p. 1-15.
36. Ustinov, A., V. Ustinov, and J. Mitrovic, *Pool boiling heat transfer of tandem tubes provided with the novel microstructures*. *International Journal of Heat and Fluid Flow*, 2011. **32**(4): p. 777-784.

37. Launay, S., et al., *Hybrid micro-nano structured thermal interfaces for pool boiling heat transfer enhancement*. *Microelectronics Journal*, 2006. **37**(11): p. 1158-1164.
38. Zhang, M. and K. Lian, *Using bulk micromachined structures to enhance pool boiling heat transfer*. *Microsystem Technologies*, 2008. **14**(9-11): p. 1499-1505.
39. Kim, S., et al., *Effects of nano-fluid and surfaces with nano structure on the increase of CHF*. *Experimental thermal and fluid science*, 2010. **34**(4): p. 487-495.
40. Cooke, D. and S.G. Kandlikar. *Pool boiling heat transfer and bubble dynamics over plain and enhanced microchannels*. in *ASME 2010 8th International Conference on Nanochannels, Microchannels, and Minichannels collocated with 3rd Joint US-European Fluids Engineering Summer Meeting*. 2010. American Society of Mechanical Engineers.
41. Ahn, H.S., V. Sathyamurthi, and D. Banerjee, *Pool Boiling Experiments on a Nano-Structured Surface*. *IEEE Transactions on Components and Packaging Technologies*, 2009. **32**(1): p. 156-165.
42. Kubo, H., H. Takamatsu, and H. Honda, *Effects of size and number density of micro-reentrant cavities on boiling heat transfer from a silicon chip immersed in degassed and gas-dissolved FC-72*. *Journal of Enhanced Heat Transfer*, 1999. **6**(2-4).
43. Honda, H., H. Takamatsu, and J. Wei, *Enhanced boiling heat transfer from silicon chips with micro-pin fins immersed in FC-72*. *Journal of Enhanced Heat Transfer*, 2003. **10**(2).
44. Shojaeian, M. and A. Koşar, *Pool boiling and flow boiling on micro-and nanostructured surfaces*. *Experimental Thermal and Fluid Science*, 2015. **63**: p. 45-73.
45. Lu, Y.-W. and S.G. Kandlikar, *Nanoscale Surface Modification Techniques for Pool Boiling Enhancement—A Critical Review and Future Directions*. *Heat Transfer Engineering*, 2011. **32**(10): p. 827-842.
46. Şeşen, M., et al. *A compact nanostructure integrated pool boiler for microscale cooling applications*. in *ASME 2009 International Mechanical Engineering Congress and Exposition*. 2009. American Society of Mechanical Engineers.

47. Bourdon, B., et al., *Wettability influence on the onset temperature of pool boiling: Experimental evidence onto ultra-smooth surfaces*. Advances in Colloid and Interface Science, 2015. **221**: p. 34-40.
48. Gong, S. and P. Cheng, *Lattice Boltzmann simulations for surface wettability effects in saturated pool boiling heat transfer*. International Journal of Heat and Mass Transfer, 2015. **85**: p. 635-646.
49. Yang, L.-X., et al., *Wettability and boiling heat transfer study of black silicon surface produced using the plasma immersion ion implantation method*. Applied Thermal Engineering, 2016. **99**: p. 253-261.
50. Kweon, Y. and M. Kim, *Experimental study on nucleate boiling enhancement and bubble dynamic behavior in saturated pool boiling using a nonuniform dc electric field*. International Journal of Multiphase Flow, 2000. **26**(8): p. 1351-1368.
51. Mukherjee, A. and S.G. Kandlikar, *Numerical study of single bubbles with dynamic contact angle during nucleate pool boiling*. International Journal of Heat and Mass Transfer, 2007. **50**(1): p. 127-138.
52. Hsieh, S.-S. and C.-G. Ke, *Bubble dynamic parameters and pool boiling heat transfer on plasma coated tubes in saturated R-134a and R-600a*. Journal of heat transfer, 2002. **124**(4): p. 704-716.
53. Barthau, G., *Active nucleation site density and pool boiling heat transfer—an experimental study*. International journal of heat and mass transfer, 1992. **35**(2): p. 271-278.
54. Benjamin, R. and A. Balakrishnan, *Nucleation site density in pool boiling of saturated pure liquids: effect of surface microroughness and surface and liquid physical properties*. Experimental Thermal and Fluid Science, 1997. **15**(1): p. 32-42.
55. Yang, S. and R. Kim, *A mathematical model of the pool boiling nucleation site density in terms of the surface characteristics*. International journal of heat and mass transfer, 1988. **31**(6): p. 1127-1135.
56. Wang, C. and V. Dhir, *Effect of surface wettability on active nucleation site density during pool boiling of water on a vertical surface*. Journal of Heat Transfer, 1993. **115**(3): p. 659-669.
57. Chen, R., et al., *Nanowires for enhanced boiling heat transfer*. Nano letters, 2009. **9**(2): p. 548-553.

58. Li, D., et al., *Enhancing flow boiling heat transfer in microchannels for thermal management with monolithically-integrated silicon nanowires*. Nano letters, 2012. **12**(7): p. 3385-3390.
59. Patil, C.M. and S.G. Kandlikar, *Review of the manufacturing techniques for porous surfaces used in enhanced pool boiling*. Heat Transfer Engineering, 2014. **35**(10): p. 887-902.
60. Ahn, H.S., et al., *A novel role of three dimensional graphene foam to prevent heater failure during boiling*. Scientific reports, 2013. **3**: p. 1960.
61. Sadaghiani, A.K., et al., *Foamlike 3D Graphene Coatings for Cooling Systems Involving Phase Change*. ACS Omega, 2018. **3**(3): p. 2804-2811.
62. Huh, C. and L. Scriven, *Hydrodynamic model of steady movement of a solid/liquid/fluid contact line*. Journal of Colloid and Interface Science, 1971. **35**(1): p. 85-101.
63. Nikolayev, V.S., *Dynamics of the triple contact line on a nonisothermal heater at partial wetting*. Physics of Fluids, 2010. **22**(8): p. 082105.
64. Choi, C. and M. Kim, *Wettability effects on heat transfer*, in *Two Phase Flow, Phase Change and Numerical Modeling*. 2011, InTech.
65. Vinogradova, O., et al., *Submicrocavity structure of water between hydrophobic and hydrophilic walls as revealed by optical cavitation*. Journal of colloid and interface science, 1995. **173**(2): p. 443-447.
66. Betz, A.R., et al., *Do surfaces with mixed hydrophilic and hydrophobic areas enhance pool boiling?* Applied Physics Letters, 2010. **97**(14): p. 141909.
67. Betz, A.R., J. Jenkins, and D. Attinger, *Boiling heat transfer on superhydrophilic, superhydrophobic, and superbiphilic surfaces*. International Journal of Heat and Mass Transfer, 2013. **57**(2): p. 733-741.
68. Tang, Y., et al., *Pool-boiling enhancement by novel metallic nanoporous surface*. Experimental Thermal and Fluid Science, 2013. **44**: p. 194-198.
69. Mao, R., et al., *Effect of preparation conditions on morphology and thermal stability of nanoporous copper*. Corrosion Science, 2012. **60**: p. 231-237.
70. Hayes, J., et al., *Monolithic nanoporous copper by dealloying Mn–Cu*. Journal of Materials Research, 2006. **21**(10): p. 2611-2616.
71. Zhang, Z., et al., *Nanoporous gold ribbons with bimodal channel size distributions by chemical dealloying of Al– Au alloys*. The Journal of Physical Chemistry C, 2009. **113**(4): p. 1308-1314.

72. Zhao, C., et al., *Fabrication and characterization of monolithic nanoporous copper through chemical dealloying of Mg–Cu alloys*. *Corrosion Science*, 2009. **51**(9): p. 2120-2125.
73. Xu, P., Q. Li, and Y. Xuan, *Enhanced boiling heat transfer on composite porous surface*. *International Journal of Heat and Mass Transfer*, 2015. **80**: p. 107-114.
74. Lee, C.Y., M.M.H. Bhuiya, and K.J. Kim, *Pool boiling heat transfer with nanoporous surface*. *International Journal of Heat and Mass Transfer*, 2010. **53**(19-20): p. 4274-4279.
75. Li, C.H., et al., *Comparison study of liquid replenishing impacts on critical heat flux and heat transfer coefficient of nucleate pool boiling on multiscale modulated porous structures*. *International Journal of Heat and Mass Transfer*, 2011. **54**(15-16): p. 3146-3155.
76. Tang, Y., et al., *Pool-boiling enhancement by novel metallic nanoporous surface*. *Experimental Thermal and Fluid Science*, 2013. **44**: p. 194-198.
77. Deng, D., et al., *Comparative experimental study on pool boiling performance of porous coating and solid structures with reentrant channels*. *Applied Thermal Engineering*, 2016. **107**: p. 420-430.
78. Deng, D., et al., *Pool boiling heat transfer of porous structures with reentrant cavities*. *International Journal of Heat and Mass Transfer*, 2016. **99**: p. 556-568.
79. Storr, A.T., *The effects of heating surface geometry and orientation on nucleate boiling of subcooled water*. 1959.
80. Githinji, P.M. and R.H. Sabersky, *Some Effects of the Orientation of the Heating Surface in Nucleate Boiling*. *Journal of Heat Transfer*, 1963. **85**(4): p. 379-379.
81. Rainey, K.N. and S.M. You, *Effects of heater size and orientation on pool boiling heat transfer from microporous coated surfaces*. *International Journal of Heat and Mass Transfer*, 2001. **44**(14): p. 2589-2599.
82. Ho, J.Y., K.C. Leong, and C. Yang, *Saturated pool boiling from carbon nanotube coated surfaces at different orientations*. *International Journal of Heat and Mass Transfer*, 2014. **79**: p. 893-904.
83. Kaya, A., G. Ozaydin-Ince, and M. Sezen, *Boiling heat transfer enhancement in mini/microtubes via polyhydroxyethylmethacrylate (pHEMA) coatings on inner microtube walls at high mass fluxes*. *Journal of Micromechanics and Microengineering*, 2013. **23**(11): p. 115017.

84. Sadaghiani, A.K., et al. *An Experimental Study on Flow Boiling Characteristics of pHEMA Nano-Coated Surfaces in a Microchannel*. in *ASME 2016 5th International Conference on Micro/Nanoscale Heat and Mass Transfer*. 2016. American Society of Mechanical Engineers.
85. Çıkım, T., et al., *Flow boiling enhancement in microtubes with crosslinked pHEMA coatings and the effect of coating thickness*. *Journal of Heat Transfer*, 2014. **136**(8): p. 081504.
86. Seo, H., et al., *Pool boiling CHF of reduced graphene oxide, graphene, and SiC-coated surfaces under highly wettable FC-72*. *International Journal of Heat and Mass Transfer*, 2015. **82**(Supplement C): p. 490-502.
87. Jaikumar, A., S.G. Kandlikar, and A. Gupta, *Pool Boiling Enhancement through Graphene and Graphene Oxide Coatings*. *Heat Transfer Engineering*, 2017. **38**(14-15): p. 1274-1284.
88. Jaikumar, A., et al., *Microscale Morphology Effects of Copper–Graphene Oxide Coatings on Pool Boiling Characteristics*. *Journal of Heat Transfer*, 2017. **139**(11): p. 111509-111509-11.
89. Kim, J.M., et al., *Effect of a graphene oxide coating layer on critical heat flux enhancement under pool boiling*. *International Journal of Heat and Mass Transfer*, 2014. **77**: p. 919-927.
90. Park, S.D., et al., *Effects of nanofluids containing graphene/graphene-oxide nanosheets on critical heat flux*. *Applied Physics Letters*, 2010. **97**(2): p. 023103.
91. Ahn, H.S., et al., *A novel role of three dimensional graphene foam to prevent heater failure during boiling*. *Scientific reports*, 2013. **3**.
92. Ahn, H.S., et al., *Enhanced heat transfer is dependent on thickness of graphene films: the heat dissipation during boiling*. *Scientific reports*, 2014. **4**.
93. Jo, H., et al., *A study of nucleate boiling heat transfer on hydrophilic, hydrophobic and heterogeneous wetting surfaces*. *International Journal of Heat and Mass Transfer*, 2011. **54**(25-26): p. 5643-5652.
94. Phan, H.T., et al., *Surface wettability control by nanocoating: the effects on pool boiling heat transfer and nucleation mechanism*. *International Journal of Heat and Mass Transfer*, 2009. **52**(23-24): p. 5459-5471.

95. Khalili Sadaghiani, A., et al., *Pool Boiling Heat Transfer Characteristics of Inclined pHEMA-Coated Surfaces*. Journal of Heat Transfer, 2017. **139**(11): p. 111501-111501-11.
96. Sadaghiani, A.K., et al., *Foamlike 3D Graphene Coatings for Cooling Systems Involving Phase Change*. ACS Omega, 2018. **3**(3): p. 2804-2811.
97. Rayleigh, L., VIII. *On the pressure developed in a liquid during the collapse of a spherical cavity*. The London, Edinburgh, and Dublin Philosophical Magazine and Journal of Science, 1917. **34**(200): p. 94-98.
98. Mikic, B., W. Rohsenow, and P. Griffith, *On bubble growth rates*. International Journal of Heat and Mass Transfer, 1970. **13**(4): p. 657-666.
99. Mikic, B. and W. Rohsenow, *A new correlation of pool-boiling data including the effect of heating surface characteristics*. Journal of Heat Transfer, 1969. **91**(2): p. 245-250.
100. Haramura, Y. and Y. Katto, *A new hydrodynamic model of critical heat flux, applicable widely to both pool and forced convection boiling on submerged bodies in saturated liquids*. International Journal of Heat and Mass Transfer, 1983. **26**(3): p. 389-399.
101. Lienhard, J. and V.J.J.o.H.T. Dhir, *Hydrodynamic prediction of peak pool-boiling heat fluxes from finite bodies*. 1973. **95**(2): p. 152-158.
102. Kandlikar, S.G.J.J.o.H.T., *A theoretical model to predict pool boiling CHF incorporating effects of contact angle and orientation*. 2001. **123**(6): p. 1071-1079.
103. Kim, J., et al., *Effect of surface roughness on pool boiling heat transfer at a heated surface having moderate wettability*. 2016. **101**: p. 992-1002.
104. Golobič, I., A.E.J.E.T. Bergles, and F. Science, *Effects of heater-side factors on the saturated pool boiling critical heat flux*. 1997. **15**(1): p. 43-51.
105. Rajvanshi, A., J. Saini, and R. Prakash, *Investigation of macrolayer thickness in nucleate pool boiling at high heat flux*. International journal of heat and mass transfer, 1992. **35**(2): p. 343-350.
106. Sakashita, H. and A. Ono, *Boiling behaviors and critical heat flux on a horizontal plate in saturated pool boiling of water at high pressures*. International Journal of Heat and Mass Transfer, 2009. **52**(3-4): p. 744-750.
107. Jansen, H., et al., *The black silicon method: a universal method for determining the parameter setting of a fluorine-based reactive ion etcher in deep silicon*

- trench etching with profile control*. Journal of Micromechanics and Microengineering, 1995. **5**(2): p. 115.
108. Schmidt, M.S., J. Hübner, and A. Boisen, *Large area fabrication of leaning silicon nanopillars for surface enhanced Raman spectroscopy*. Advanced Materials, 2012. **24**(10).
 109. Hsu, C.-M., et al., *Wafer-scale silicon nanopillars and nanocones by Langmuir–Blodgett assembly and etching*. Applied Physics Letters, 2008. **93**(13): p. 133109.
 110. Wierzbicki, R., et al., *Black silicon maskless templates for carbon nanotube forests*. Microelectronic Engineering, 2013. **104**: p. 110-113.
 111. Bankoff, S.G., *Entrapment of gas in the spreading of a liquid over a rough surface*. AIChE Journal, 1958. **4**(1): p. 24-26.
 112. Choi, J.Y., et al., *Development of a dry patch model for critical heat flux prediction*. 2016. **100**: p. 386-395.
 113. Gong, S. and P. Cheng, *Numerical simulation of pool boiling heat transfer on smooth surfaces with mixed wettability by lattice Boltzmann method*. International Journal of Heat and Mass Transfer, 2015. **80**: p. 206-216.
 114. Tenhaeff, W.E. and K.K. Gleason, *Initiated and oxidative chemical vapor deposition of polymeric thin films: iCVD and oCVD*. Advanced Functional Materials, 2008. **18**(7): p. 979-992.
 115. Nedaei, M., et al., *Enhancement of flow boiling heat transfer in pHEMA/pPFDA coated microtubes with longitudinal variations in wettability*. AIP Advances, 2016. **6**(3): p. 035212.
 116. Li, C. and G. Peterson, *Parametric study of pool boiling on horizontal highly conductive microporous coated surfaces*. Journal of heat transfer, 2007. **129**(11): p. 1465-1475.
 117. Jung, S. and H. Kim, *Effects of surface orientation on nucleate boiling heat transfer in a pool of water under atmospheric pressure*. Nuclear Engineering and Design, 2016. **305**: p. 347-358.
 118. Cooke, D. and S.G. Kandlikar, *Effect of open microchannel geometry on pool boiling enhancement*. International Journal of Heat and Mass Transfer, 2012. **55**(4): p. 1004-1013.
 119. Moghaddam, S., M. Ohadi, and J. Qi. *Pool boiling of water and FC-72 on copper and graphite foams*. in *ASME 2003 International Electronic Packaging*

- Technical Conference and Exhibition*. 2003. American Society of Mechanical Engineers.
120. Ji, X., et al., *Pool boiling heat transfer on uniform and non-uniform porous coating surfaces*. *Experimental Thermal and Fluid Science*, 2013. **48**: p. 198-212.
 121. Jaikumar, A. and S.G. Kandlikar, *Enhanced pool boiling for electronics cooling using porous fin tops on open microchannels with FC-87*. *Applied Thermal Engineering*, 2015. **91**: p. 426-433.
 122. Demir, E., et al., *Effect of silicon nanorod length on horizontal nanostructured plates in pool boiling heat transfer with water*. *International Journal of Thermal Sciences*, 2014. **82**: p. 111-121.
 123. Patil, C.M. and S.G. Kandlikar, *Pool boiling enhancement through microporous coatings selectively electrodeposited on fin tops of open microchannels*. *International Journal of Heat and Mass Transfer*, 2014. **79**: p. 816-828.
 124. Smirnov, H.F., *Boiling on Coated Surfaces and in Porous Structures*. 2001. **4**(1): p. 20.
 125. Jaikumar, A. and S.G. Kandlikar, *Ultra-high pool boiling performance and effect of channel width with selectively coated open microchannels*. *International Journal of Heat and Mass Transfer*, 2016. **95**: p. 795-805.
 126. Webb, R.L., *Nucleate Boiling on Porous Coated Surfaces*. *Heat Transfer Engineering*, 1983. **4**(3-4): p. 71-82.
 127. Bergles, A.E. and M.C. Chyu, *Characteristics of Nucleate Pool Boiling From Porous Metallic Coatings*. *Journal of Heat Transfer*, 1982. **104**(2): p. 279-285.
 128. Novoselov, K., et al., *Two-dimensional atomic crystals*. *Proceedings of the National Academy of Sciences of the United States of America*, 2005. **102**(30): p. 10451-10453.
 129. Neto, A.C., et al., *The electronic properties of graphene*. *Reviews of modern physics*, 2009. **81**(1): p. 109.
 130. Scarpa, F., S. Adhikari, and A.S. Phani, *Effective elastic mechanical properties of single layer graphene sheets*. *Nanotechnology*, 2009. **20**(6): p. 065709.
 131. Bonaccorso, F., et al., *Graphene photonics and optoelectronics*. *Nature photonics*, 2010. **4**(9): p. 611-622.
 132. Yavari, F., et al., *High sensitivity gas detection using a macroscopic three-dimensional graphene foam network*. *Scientific reports*, 2011. **1**.

133. Fang, Q., Y. Shen, and B. Chen, *Synthesis, decoration and properties of three-dimensional graphene-based macrostructures: a review*. Chemical Engineering Journal, 2015. **264**: p. 753-771.
134. Yao, Z., Y.-W. Lu, and S.G. Kandlikar, *Fabrication of nanowires on orthogonal surfaces of microchannels and their effect on pool boiling*. Journal of Micromechanics and Microengineering, 2012. **22**(11): p. 115005.
135. Mao, S., G. Lu, and J. Chen, *Three-dimensional graphene-based composites for energy applications*. Nanoscale, 2015. **7**(16): p. 6924-6943.
136. Zhang, L. and G. Shi, *Preparation of highly conductive graphene hydrogels for fabricating supercapacitors with high rate capability*. The Journal of Physical Chemistry C, 2011. **115**(34): p. 17206-17212.
137. Xue, Y., et al., *Three-dimensional B, N-doped graphene foam as a metal-free catalyst for oxygen reduction reaction*. Physical Chemistry Chemical Physics, 2013. **15**(29): p. 12220-12226.
138. Lee, J.-S., et al., *Three-dimensional nano-foam of few-layer graphene grown by CVD for DSSC*. Physical Chemistry Chemical Physics, 2012. **14**(22): p. 7938-7943.
139. Zhang, X., et al., *Mechanically strong and highly conductive graphene aerogel and its use as electrodes for electrochemical power sources*. journal of materials chemistry, 2011. **21**(18): p. 6494-6497.
140. Yong, Y.-C., et al., *Macroporous and monolithic anode based on polyaniline hybridized three-dimensional graphene for high-performance microbial fuel cells*. ACS nano, 2012. **6**(3): p. 2394-2400.
141. Cao, X., et al., *Preparation of novel 3D graphene networks for supercapacitor applications*. small, 2011. **7**(22): p. 3163-3168.
142. Pettes, M.T., et al., *Thermal transport in three-dimensional foam architectures of few-layer graphene and ultrathin graphite*. Nano letters, 2012. **12**(6): p. 2959-2964.
143. Lin, H., et al., *Significantly reduced thermal diffusivity of free-standing two-layer graphene in graphene foam*. Nanotechnology, 2013. **24**(41): p. 415706.
144. Nguyen, D.D., et al., *Superhydrophobic and superoleophilic properties of graphene-based sponges fabricated using a facile dip coating method*. Energy & environmental science, 2012. **5**(7): p. 7908-7912.

145. Dong, X., et al., *Hybrid structure of zinc oxide nanorods and three dimensional graphene foam for supercapacitor and electrochemical sensor applications*. RSC Advances, 2012. **2**(10): p. 4364-4369.
146. Gao, W., K.M. Liechti, and R. Huang, *Wet adhesion of graphene*. Extreme Mechanics Letters, 2015. **3**: p. 130-140.
147. Asay, D.B. and S.H. Kim, *Evolution of the adsorbed water layer structure on silicon oxide at room temperature*. The Journal of Physical Chemistry B, 2005. **109**(35): p. 16760-16763.
148. Gao, L., et al., *Face-to-face transfer of wafer-scale graphene films*. Nature, 2014. **505**(7482): p. 190.
149. Lee, M.J., et al., *Characteristics and effects of diffused water between graphene and a SiO₂ substrate*. Nano Research, 2012. **5**(10): p. 710-717.
150. Kumar, S., D. Parks, and K. Kamrin, *Mechanistic origin of the ultrastrong adhesion between graphene and α -SiO₂: beyond van der Waals*. ACS nano, 2016. **10**(7): p. 6552-6562.
151. Murthy, S., et al., *Enhanced boiling heat transfer simulation from structured surfaces: semi-analytical model*. International journal of heat and mass transfer, 2006. **49**(11): p. 1885-1895.
152. Ramaswamy, C., et al., *Semi-analytical model for boiling from enhanced structures*. International Journal of Heat and Mass Transfer, 2003. **46**(22): p. 4257-4269.
153. Zeng, L., J. Klausner, and R. Mei, *A unified model for the prediction of bubble detachment diameters in boiling systems—I. Pool boiling*. International Journal of Heat and Mass Transfer, 1993. **36**(9): p. 2261-2270.
154. Khalili Sadaghiani, A., et al., *Pool boiling heat transfer characteristics of inclined pHEMA-coated surfaces*. Journal of Heat Transfer, 2017. **139**(11).
155. Yortsos, Y.C. and A.K. Stubos, *Phase change in porous media*. Current opinion in colloid & interface science, 2001. **6**(3): p. 208-216.
156. Or, D., *Scaling of capillary, gravity and viscous forces affecting flow morphology in unsaturated porous media*. Advances in water resources, 2008. **31**(9): p. 1129-1136.
157. Méheust, Y., et al., *Interface scaling in a two-dimensional porous medium under combined viscous, gravity, and capillary effects*. Physical Review E, 2002. **66**(5): p. 051603.

158. Ha, M. and S. Graham, *Pool boiling characteristics and critical heat flux mechanisms of microporous surfaces and enhancement through structural modification*. Applied Physics Letters, 2017. **111**(9): p. 091601.
159. Reeve, J.N., *Archaeobacteria then... Archaea now (are there really no archaeal pathogens?)*. Journal of bacteriology, 1999. **181**(12): p. 3613-3617.
160. Woese, C.R. and G.E. Fox, *Phylogenetic structure of the prokaryotic domain: the primary kingdoms*. Proceedings of the National Academy of Sciences, 1977. **74**(11): p. 5088-5090.
161. Ciaramella, M., F.M. Pisani, and M. Rossi, *Molecular biology of extremophiles: recent progress on the hyperthermophilic archaeon Sulfolobus*. Antonie Van Leeuwenhoek, 2002. **81**(1-4): p. 85-97.
162. Bell, S.D. and S.P. Jackson, *Transcription and translation in Archaea: a mosaic of eukaryal and bacterial features*. Trends in microbiology, 1998. **6**(6): p. 222-228.
163. Chaban, B., S.Y. Ng, and K.F. Jarrell, *Archaeal habitats—from the extreme to the ordinary*. Canadian journal of microbiology, 2006. **52**(2): p. 73-116.
164. Schleper, C., et al., *Picrophilus gen. nov., fam. nov.: a novel aerobic, heterotrophic, thermoacidophilic genus and family comprising archaea capable of growth around pH 0*. Journal of bacteriology, 1995. **177**(24): p. 7050-7059.
165. Kashefi, K. and D.R. Lovley, *Extending the upper temperature limit for life*. Science, 2003. **301**(5635): p. 934-934.
166. Moll, R. and G. Schäfer, *Chemiosmotic H⁺ cycling across the plasma membrane of the thermoacidophilic archaeobacterium Sulfolobus acidocaldarius*. FEBS letters, 1988. **232**(2): p. 359-363.
167. Grogan, D.W., *Phenotypic characterization of the archaeobacterial genus Sulfolobus: comparison of five wild-type strains*. Journal of Bacteriology, 1989. **171**(12): p. 6710-6719.
168. Brock, T.D., et al., *Sulfolobus: a new genus of sulfur-oxidizing bacteria living at low pH and high temperature*. Archives of Microbiology, 1972. **84**(1): p. 54-68.
169. Singh, S.K., et al., *Wetting dynamics and evaporation of sessile droplets on nano-porous alumina surfaces*. Colloids and Surfaces A: Physicochemical and Engineering Aspects, 2013. **432**: p. 71-81.

170. Das, S. and S. Bhaumik, *Experimental study of nucleate pool boiling heat transfer using water on thin-film surface*. Iranian Journal of Science and Technology, Transactions of Mechanical Engineering, 2016. **40**(1): p. 21-29.
171. Battin, T.J., et al., *Microbial landscapes: new paths to biofilm research*. Nature Reviews Microbiology, 2007. **5**(1): p. 76-81.
172. Schrenk, M.O., et al., *Low archaeal diversity linked to seafloor geochemical processes at the Lost City Hydrothermal Field, Mid-Atlantic Ridge*. Environmental Microbiology, 2004. **6**(10): p. 1086-1095.
173. Macalady, J.L., D.S. Jones, and E.H. Lyon, *Extremely acidic, pendulous cave wall biofilms from the Frasassi cave system, Italy*. Environmental Microbiology, 2007. **9**(6): p. 1402-1414.
174. Niederberger, T.D., et al., *Ignisphaera aggregans gen. nov., sp. nov., a novel hyperthermophilic crenarchaeote isolated from hot springs in Rotorua and Tokaanu, New Zealand*. International journal of systematic and evolutionary microbiology, 2006. **56**(5): p. 965-971.
175. Ionescu, D., et al., *Microbial and chemical characterization of underwater fresh water springs in the Dead Sea*. PloS one, 2012. **7**(6): p. e38319.
176. Davey, M.E. and G.A. O'toole, *Microbial biofilms: from ecology to molecular genetics*. Microbiology and molecular biology reviews, 2000. **64**(4): p. 847-867.
177. Flemming, H.-C. and J. Wingender, *The biofilm matrix*. Nature reviews. Microbiology, 2010. **8**(9): p. 623.
178. Zolghadr, B., et al., *Appendage-mediated surface adherence of Sulfolobus solfataricus*. Journal of bacteriology, 2010. **192**(1): p. 104-110.
179. Schrenk, M.O., et al., *Incidence and diversity of microorganisms within the walls of an active deep-sea sulfide chimney*. Applied and Environmental Microbiology, 2003. **69**(6): p. 3580-3592.
180. Henche, A.L., et al., *Influence of cell surface structures on crenarchaeal biofilm formation using a thermostable green fluorescent protein*. Environmental microbiology, 2012. **14**(3): p. 779-793.
181. Fröls, S., et al., *UV-inducible cellular aggregation of the hyperthermophilic archaeon Sulfolobus solfataricus is mediated by pili formation*. Molecular microbiology, 2008. **70**(4): p. 938-952.

182. Koerdt, A., et al., *Complementation of Sulfolobus solfataricus PBL2025 with an α -mannosidase: effects on surface attachment and biofilm formation*. *Extremophiles*, 2012. **16**(1): p. 115-125.
183. Ajon, M., et al., *UV-inducible DNA exchange in hyperthermophilic archaea mediated by type IV pili*. *Molecular microbiology*, 2011. **82**(4): p. 807-817.
184. Furberg, R., et al., *The use of a nano-and microporous surface layer to enhance boiling in a plate heat exchanger*. *Journal of Heat Transfer*, 2009. **131**(10): p. 101010.
185. Liter, S.G. and M. Kaviany, *Pool-boiling CHF enhancement by modulated porous-layer coating: theory and experiment*. *International Journal of Heat and Mass Transfer*, 2001. **44**(22): p. 4287-4311.
186. Ha, M. and S. Graham. *Pool boiling enhancement through hierarchical texturing of surfaces*. in *Thermal and Thermomechanical Phenomena in Electronic Systems (ITherm), 2016 15th IEEE Intersociety Conference on*. 2016. IEEE.
187. Rohsenow, W.M., J.P. Hartnett, and Y.I. Cho, *Handbook of heat transfer*. Vol. 3. 1998: McGraw-Hill New York.
188. Gorenflo, D. and D. Kenning, *H2 Pool boiling*. 2009: Springer.
189. Coleman, H.W. and W.G. Steele, *Experimentation, validation, and uncertainty analysis for engineers*. 2018: John Wiley & Sons.
190. Coleman, H.W. and W.G. Steele, *Experimentation, validation, and uncertainty analysis for engineers*. 2009: John Wiley & Sons.
191. Lemczyk, T. and D. Molloy, *Fluid Properties Research Report: Advanced Engineering NP-329*. Long Manufacturing, 1996.
192. Babcock, et al., *Steam: its generation and use*. 1992: Babcock & Wilcox.
193. Liu, D. and S.V. Garimella, *Flow boiling heat transfer in microchannels*. *Journal of Heat Transfer*, 2007. **129**(10): p. 1321-1332.
194. McHale, J.P. and S.V. Garimella, *Bubble nucleation characteristics in pool boiling of a wetting liquid on smooth and rough surfaces*. *International Journal of Multiphase Flow*, 2010. **36**(4): p. 249-260.
195. Michaelides, E.E., *Hydrodynamic force and heat/mass transfer from particles, bubbles, and drops—the Freeman scholar lecture*. *Journal of fluids engineering*, 2003. **125**(2): p. 209-238.

196. Ishii, M. and N. Zuber, *Drag coefficient and relative velocity in bubbly, droplet or particulate flows*. AIChE Journal, 1979. **25**(5): p. 843-855.
197. Chien, L.-H. and R.L. Webb, *Measurement of bubble dynamics on an enhanced boiling surface*. Experimental Thermal and Fluid Science, 1998. **16**(3): p. 177-186.

APENDIX 1 – Experimental setup and procedure

A1.1 Experimental setup

The experimental facility includes a glass pool, an aluminum block heater, 5 cartridge heaters, 6 thermocouples, a power supply, a reflux condenser, a Teflon insulation block, thermos-meters, and a high speed camera. Figure A1- 1 shows the schematic of the experimental setup. De-ionized water was used as the working fluid in pool boiling experiments. Silicon wafers with dimensions of 15×15 (mm²), surface roughness of 0.145 nm, thickness of 500 μ m, and thermal conductivity of 130 (W/m.K) were used as substrates. Due to high thermal conductivity and ease of machinability Aluminum was selected as the heating block material. The Aluminum heating block accommodates four vertical cartridge heaters connected to a DC power supply. Five calibrated K type thermocouples (with uncertainty ± 0.3 %) were tight-fastened in designated holes with diameter of 0.7mm and depth of 7.5 mm. Horizontal thermocouples (located 2mm below the tested samples) were used for surface measurements, while vertical thermocouples were used for the heat flux calculation (1-D conduction).

A Teflon block was used to minimize heat losses to the ambient. Teflon was used as the thermal insulator material due to its low thermal conductivity (0.05 W/m.K) and ease of machinability. A glass pool was used to visualize the boiling phenomena on different specimens. The glass pool has the outer and inner dimensions of $60 \times 60 \times 50$, and $40 \times 40 \times 50$ (mm³), respectively. On top of the glass, an O ring was used to seal the pool. A thermocouple (for temperature measurement) and a submerged heater (for maintaining the saturated condition) were inserted into the pool. A reflux condenser (open to the atmosphere) was used on top of the test section to keep the amount of working fluid constant during the experiments. A sandwich mechanism was utilized to put the all parts together. Pool boiling experiments were conducted under atmospheric pressure using water as the working fluid.

The power supply was connected to cartridge heaters. The cartridge heaters were press-fitted into cylindrical holes, while high-quality conductive silicon grease was utilized to fill the gap between the cartridge heaters and inner areas of the holes. Two holder plates were used to sandwich the glass block and the Teflon block. The upper holder plate had four holes that were used for filling up the glass block with working fluid, inserting a thermocouple to measure the bulk temperature of fluid, inserting a vertical heater to keep the fluid at the saturation temperature, and to make a connection with the vertical condenser to provide a constant supply of deionized water.

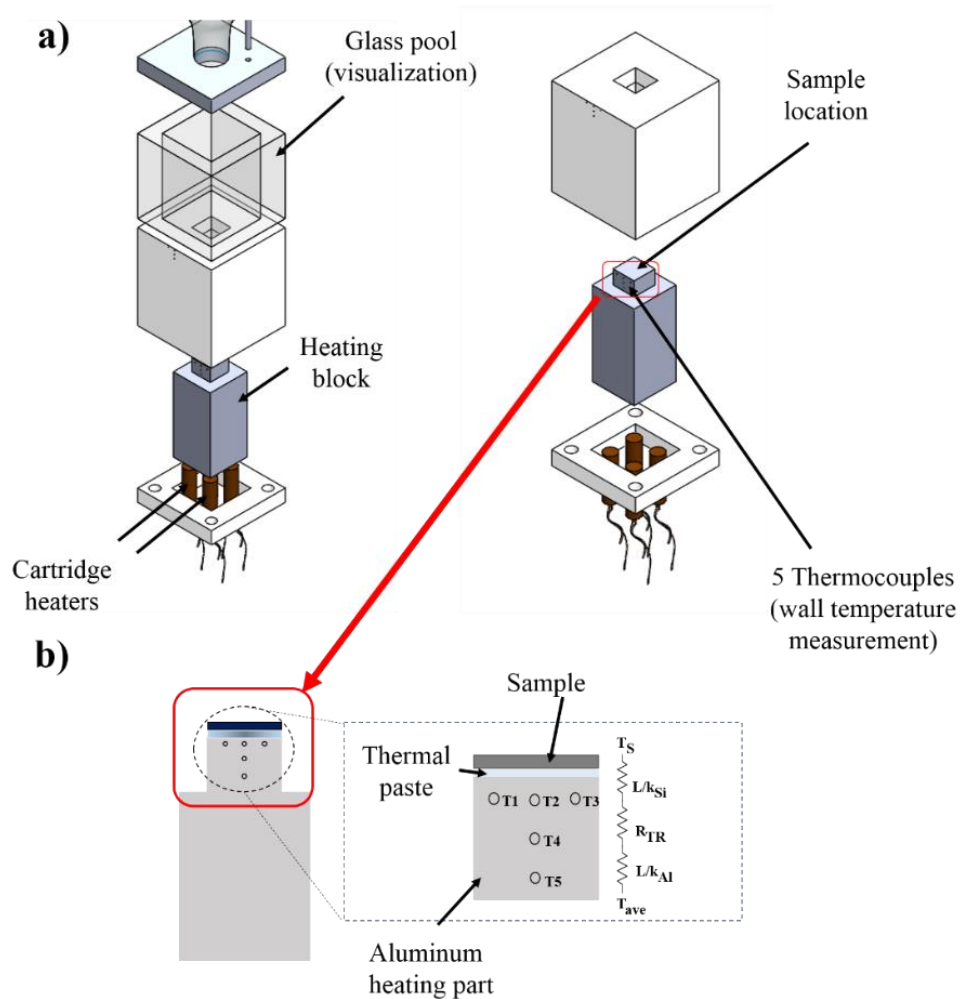


Figure A1- 1 a) Schematic of the test section and assemblies of the experimental setup b) wall temperature measurement locations

Heating block: Four vertical holes at the bottom of heating parts, and five horizontal holes were manufactured on the heating block for cartridge heaters and thermocouples, respectively. Heating was applied to the heating section using a digital power supply connected to the press fitted cartridge heaters. Samples with areas of

15×15 and 40×40 mm² were attached to the same area of aluminum heating area. A high quality conductive glue was used to fill the air gap between heating and surrounding areas such as cartridge heaters and their housings, and heating surface and samples.

Glass block: A glass hollow cube with the outer and inner dimensions of 60×60×60 mm³, and 40×40×60 cm³ (W×L×H), respectively, were attached on top of the heating block for visualization purposes. A thermocouple was inserted to the pool to be in contact with the working fluid for liquid temperature measurements. In addition to cartridge heaters inserted to the heating block, a heater is emerged into the working liquid to increase the temperature to saturated temperatures (for saturation pool boiling experiments).

Sandwich mechanism: Two holder plates were used to sandwich the glass block and the Teflon block. The upper holder plate has four holes, which were used for heating the working fluid, insert a thermocouple to measure bulk temperature of fluid, insert a vertical heater to keep the fluid at saturation temperature and make a connection with the vertical condenser to provide a constant supply of working fluid. High temperature resistive gaskets were used between glass and heating blocks to prevent any leakage.

A reflux condenser were used to maintain the working fluid at a constant amount of 80ml. The reflux condenser is made of concentric glass tubes of inner and outer diameters of 22 mm and 40 mm, respectively, and a length of 200 mm. A secondary cold water was flowing through the gap between the outer and inner tubes to condense the vapor escaping through the inner tube, which is open to atmosphere, to maintain the tests at the ambient pressure. The volume of liquid was measured before and after each test to check for the change in the liquid amount. It was found that the vertical reflux condenser was efficient, and the amount of water remained nearly the same.

High speed camera: A high-speed camera (250 frames/sec) was used to visualize pool boiling experiments. Bubble dynamics and behavior prior to and during the departure were examined and analyzed to attain a better understanding of the enhancement mechanism. For each experiment, more than 50 bubbles were selected to determine average bubble departure volume.

A1.2 Procedure

With the help of a digital power supply with high-precision multimeters, current and voltage were adjusted. All of the experiments were conducted at saturation temperature under ambient pressure with deionized water that was degassed by boiling for 15 min as working fluid. The water was heated to saturation temperature by an emerged cartridge heater. During the experiments, the amount of working fluid was kept constant using a vertical condenser on top of the pool that was opened to atmospheric pressure.

The CHF was defined as the first detected excessive rise in wall temperature during the experiments. At that moment, the sample was totally covered by a vapor blanket that was recorded using a high-speed camera. In most cases, CHF occurrence led to the burnout condition.

All the temperatures were recorded under steady state conditions. To ensure repeatability, every sample was tested three times. The heat flux was increased in small steps until the CHF point was reached. At this point, an excessive rise in wall temperature and a vapor blanket on the samples were observed. The experimental data were reduced to obtain the heat transfer coefficient and heat flux.

All the experiments were conducted at saturation temperature and ambient pressure with degassed deionized water (DI) as the working fluid. The DI water was heated to the saturation temperature by cartridge heaters. The waiting time to reach the steady-state condition depends on the heat flux. The CHF condition was defined as the occurrence of excessive rise in the wall temperature.

A1.3 Validation

Prior to the experiments, the experimental setup and procedure were validated using two widely used correlations:

$$\text{Rohsenow et al. [187]} \quad \frac{c_p \Delta T}{h_{lg}} = C_{sf} \left(\frac{q''}{h_{lg} \mu_l \left[\frac{\sigma}{g(\rho_l - \rho_g)} \right]^{1/2}} \right)^m \left(\frac{c_{pl} \mu_l}{k_l} \right)^n \quad \text{A1. 1}$$

Gorenflo [188]

$$\alpha = \alpha_0 \left(\frac{q}{q_0} \right)^{0.9-0.3Pr^{0.3}} \left(1.2P_r^{0.27} + 2.5P_r + \frac{P_r}{1-P_r} \right) \left(\frac{R_a}{R_{a^0}} \right)^{2/15} \left(\frac{k\rho c}{k_0\rho_0c_0} \right)^{1/4} \quad A1.2$$

The comparison between the results obtained from the plain surface and predictions of these correlations is shown in Figure A1- 2. As seen, experimental heat transfer coefficients are in an acceptable agreement with these correlations. At low heat fluxes, Gorenflo correlation's prediction is better, while Rohsenow correlation provides a better prediction for high heat fluxes. The main reason for the deviation of experimental heat transfer coefficients from the predictions of the correlations is that the experiments were performed using silicon surfaces, while available correlations are recommended for metallic surfaces [187, 188].

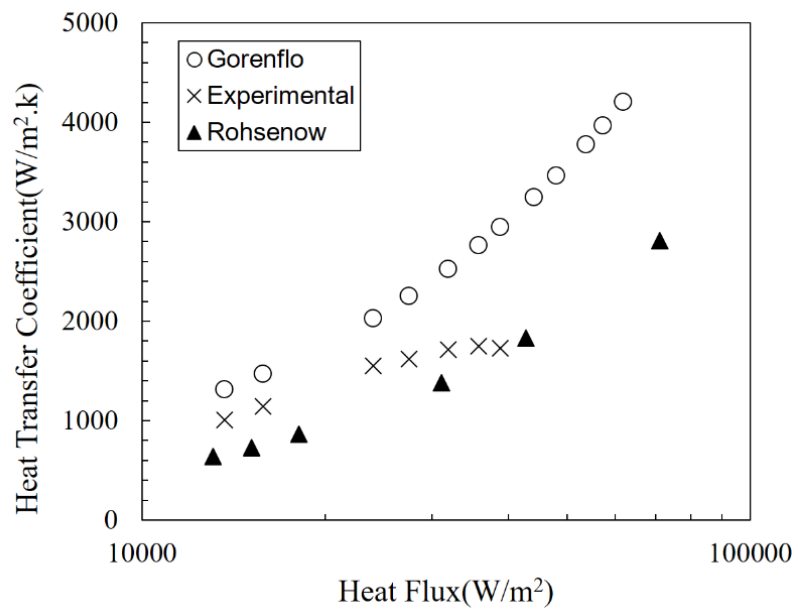


Figure A1- 2 Validation with available nucleate pool boiling correlations in the literature [187, 188].

APENDIX 2 - Data reduction and uncertainty analyses

A2.1 Data reduction

Constant heat flux boundary condition was applied to the heating surface by changing the voltage and current of the power supply gradually for each step. The net heat flux was calculated as:

$$q'' = \frac{VI - Q_{loss}}{A} \quad \text{A2. 1}$$

Here, V and I are supplied voltage and current to the cartridge heaters, A is the heated surface area, and Q_{loss} is the heat loss. Heat loss is the difference between input power and the amount of cooling energy in single-phase flow regime in boiling experiments. For minimizing the amount of heat loss, the aluminum heating part is surrounded by a Teflon block which is a prevalent as of insulator. To calculate the amount of heat loss for each test, a natural convection analysis was performed. Accordingly, the heat losses are less than 5%.

The boiling heat transfer coefficient, h , was calculated using the following expression:

$$h = \frac{q''}{T_w - T_{sat}} \quad \text{A2. 2}$$

Here, q'' , T_w , and T_{sat} are wall heat flux, wall temperature, and saturation temperature, respectively. Applied wall heat flux was also calculated using the recorded T_2 , T_4 , and T_5 temperatures. Here, a vertical 1-D heat conduction analysis is made as follows:

$$q'' = -k \frac{dT}{dx} \quad \text{A2. 3}$$

In this equation, the temperature gradient ($\frac{dT}{dx}$) is calculated using the approach of 3 point back-ward Taylor series as

$$dT/dx = \frac{(3T_2 - 4T_4 + T_5)}{2dx} \quad \text{A2. 4}$$

. With the known wall heat flux and a thermal resistance network (shown in Fig. 3), the surface temperature can be found as:

$$T_s = T_{ave} - q'' \left(\frac{L_{Al}}{K_{Al}} + R_{TR} + \frac{L_{Si}}{K_{Si}} \right) \quad \text{A2. 5}$$

Here, $T_{ave} = (T_1 + T_2 + T_3)/3$ is the average temperature, k is the solid thermal conductivity, $R_{TR} = 6 \times 10^{-6} \left(\frac{\text{m}^2\text{K}}{\text{W}} \right)$ is the thermal paste resistance, L_{Al} and L_{Si} are the thickness of aluminum and silicon samples, respectively. The wall superheat (ΔT_{sat}) is defined as the difference between the saturation temperature (T_{sat}) and surface temperature (T_s).

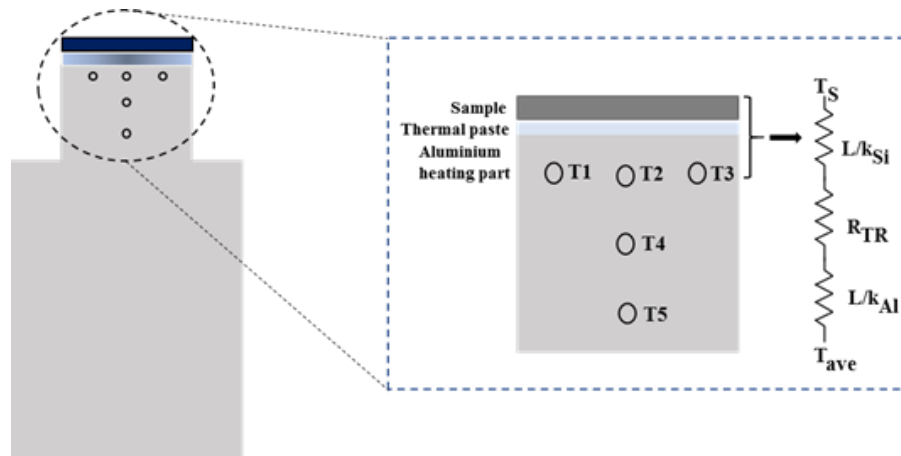


Figure A2- 1 Schematic of thermocouple locations and approach of surface temperature measurement

Wall superheat, ΔT_{sat} , is defined as the difference between the saturation temperature, T_{sat} , and the average surface temperature, $T_w = \sum_1^3 T_{w,i} / 3$, which is defined as the average of three thermocouples located beneath the heating surface. The wall temperatures were obtained by considering the thermal contact resistance from the thermocouple to the surface R_C and the average of the thermocouple measurements, T_{th} , as:

$$T_{w,i} = T_{\text{th},i} - q'' \times R_C \quad \text{A2. 6}$$

All of the temperatures and power readings were recorded under steady-state conditions. To ensure repeatability, every sample was tested three times. The heat flux was increased in small steps until the CHF point was reached. At this point, an excessive rise in the wall temperature and vapor blanket was observed. The experimental data were reduced to obtain the heat transfer coefficients (HTCs) and heat flux.

A2.2 Uncertainty analysis

Each experiment was performed for three times to ensure the repeatability of the measurements. An uncertainty analysis is used for measuring instruments and experimental data based on the error propagation methodology proposed by Coleman and Steele [189]. The general formulation is expressed as:

$$U_y = \sqrt{\sum_{i=1}^n \left\{ \left(\frac{\partial y}{\partial x_i} \right) U_{x_i} \right\}^2} \quad \text{A2. 7}$$

Here, U_{x_i} is the uncertainty in the parameter X_i .

Each measured value X_i has an associated uncertainty represented by the notation ∂X_i , the effect of the uncertainty in X_i on the result R is calculated by:

$$\delta R_{x_i} = \frac{\partial R}{\partial X_i} \delta X_i \quad \text{A2. 8}$$

Where δR_{X_i} refers to the uncertainty in R as a result of the uncertainty in the X_i measurement. Then the uncertainty in the result is given in general form as:

$$\delta R = \sqrt{\left(\frac{\partial R}{\partial X_1} \delta X_1\right)^2 + \left(\frac{\partial R}{\partial X_2} \delta X_2\right)^2 + \left(\frac{\partial R}{\partial X_3} \delta X_3\right)^2 + \dots + \left(\frac{\partial R}{\partial X_n} \delta X_n\right)^2} \quad \text{A2.}$$

9

When R depends on a number of measured quantities and this dependence can be expressed in the form:

$$R = X_1^{C_1} X_2^{C_2} X_3^{C_3} \dots X_n^{C_n} \quad \text{A2. 10}$$

The overall uncertainty is determined from the uncertainties of each of the individual measurements:

$$\frac{\delta R}{R} = \pm \sqrt{\left(C_1 \frac{\delta X_1}{X_1}\right)^2 + \left(C_2 \frac{\delta X_2}{X_2}\right)^2 + \left(C_3 \frac{\delta X_3}{X_3}\right)^2 + \dots + \left(C_n \frac{\delta X_n}{X_n}\right)^2} \quad \text{A2. 11}$$

The result of this equation is the overall uncertainty in R expressed as a percentage. The following section describes the uncertainty associated with the instrumentation and the method used in the measurements of each of the individual quantities.

As an example properties of water (liquid and vapor) were determined based on correlations of tabulated values as function of temperature presented by Lemczyk and Molloy [191] and Babcock and Wilcox [192]. The correlations deviate from the tabulated values by less than 0.4 %. Therefore, the uncertainty in the fluid properties is:

$$\frac{\partial \text{Properties}}{\text{Properties}} = \pm 4 \times 10^{-3} \quad \text{A.1}$$

Also the heat transfer coefficient for saturated two-phase flow was calculated as

$$h = \frac{q_w}{(T_w - T_{sat})}. \text{ After applying the general form and rearrangement of terms:}$$

$$\frac{\partial h_{tp}}{h_{tp}} = \pm \sqrt{\left(\frac{\partial q_w}{q_w}\right)^2 + \left(\frac{T_w}{T_w - T_{sat}} \frac{\partial T_w}{T_w}\right)^2 + \left(\frac{T_{sat}}{T_w - T_{sat}} \frac{\partial T_{sat}}{T_{sat}}\right)^2}$$

The calculated uncertainties are presented in Table A2- 1.

Table A2- 1 Estimated uncertainties of experimental parameters

Parameters	Uncertainty
Voltage	± 1 V
Electrical current	± 0.1 A
Image pixel size	250 μm
Wall Temperature	± 1 -5%
Fluid Temperature	± 1 -4%
Heat Transfer Coefficient	± 2 -5%
Critical Heat Flux (CHF)	± 5 %
Bubble departure frequency (Hz)	± 4 %
Bubble departure volume (mm^3)	± 0.05 mm^3

A2.3 Bubble departure process

Bubble departure frequency and diameter were calculated by averaging the obtained values for at least 10 nucleation sites per case, where 5 sequential bubbles in the images were tracked from growth initiation to the time they reached to the middle of the image frame. Manual pixel-wise calculation were used to determine the locations of diametrical points on bubbles. For each time interval the bubble centroid location was obtained by averaging the diametrical x and y coordinates. When the bubble radial growth becomes constant, time history of vertical position of the bubble centroid approximates the bubble departure frequency. This approximation is in agreement with Rayleigh [97] , Mikic, Rohsenow, and Griffith [98]. Due to constant radial growth rate assumption for attached bubble, the centroid location shows a linear change. Straight lined were fitted to the growth and rising portions. The intersection of the growth line with horizon (x-axis), and growth line and rising lines give the initiation and departure points, respectively. The proposed calculations are in parallel with the method recommended by McHale and Garimella [194].

The general governing equation and boundary conditions for the freely rising bubble is given as follow:

$$\ddot{y} + \frac{3 \rho_l C_D}{4 \rho_v D} \dot{y}^2 = \frac{(\rho_l - \rho_v)}{\rho_v} g \quad \text{A2. 12}$$

$$y(t_0) = y_c |_{t=t_0} \quad \text{A2. 13}$$

$$\dot{y}(t_0) = \dot{y}_c |_{t=t_0} \quad \text{A2. 14}$$

The first term in the left hand side indicates the acceleration of the rising bubble, the second term in the left hand side are included to inspect the effect of drag force, and the right hand side brings up the importance of buoyancy force effect on rising bubble. Consequently, in equation 6 the drag coefficient of a bubble, time of departure, gravitational acceleration, position and densities of liquid and vapor phases are represented as C_D , t_0 , g , y , ρ_l and ρ_v , respectively. The drag coefficient values in the range of 0.14~1.22 were used in the analysis (according to the proposed values in correlations of Michaelides [195] and Ishii and Zuber [196], respectively).

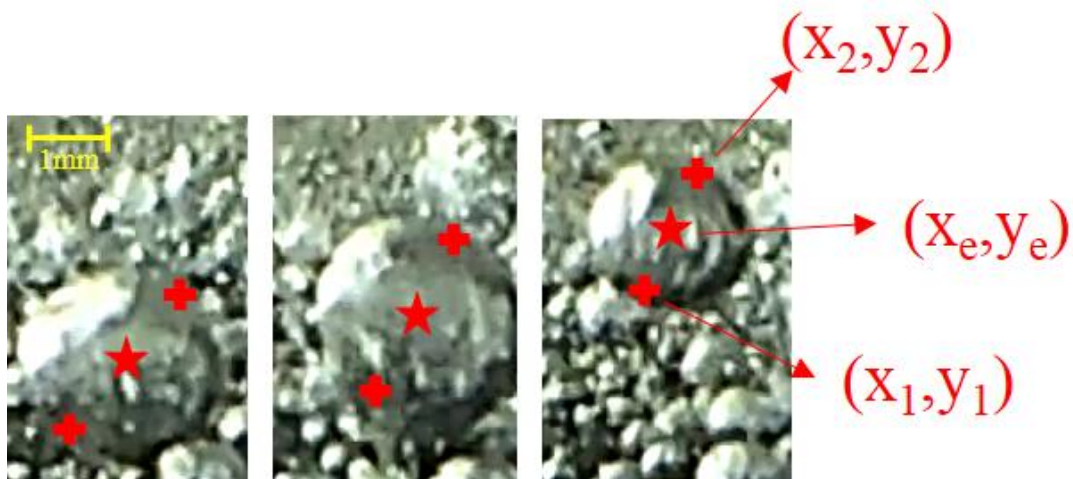


Figure A2- 2 Determination of bubble departure frequency and diameter

APPENDIX 3 - Publications

A3.1 Peer-reviewed articles

1. Motezakker, A. R., Sadaghiani, A. K., Çelik, S., Larsen, T., Villanueva, L. G., Koşar, A., (2019). Optimum Ratio of Hydrophobic to Hydrophilic Areas of Biphilic Surfaces in Thermal Fluid Systems Involving Boiling. *International Journal of Heat and Mass Transfer*, 135: p. 164-174.
2. Sadaghiani, A. K., Motezakker, A. R., Kasap, S., Kaya, I. I., & Koşar, A. (2018). Foamlike 3D graphene coatings for cooling systems involving phase change. *ACS Omega*, 3(3), 2804-2811.
3. Sadaghiani, A. K., & Koşar, A. (2018). Numerical investigations on the effect of fin shape and surface roughness on hydrothermal characteristics of slip flows in microchannels with pin fins. *International Journal of Thermal Sciences*, 124, 375-386.
4. Özdemir, M. R., Sadaghiani, A. K., Motezakker, A. R., Parapari, S. S., Park, H. S., Acar, H. Y., & Koşar, A. (2018). Experimental studies on ferrofluid pool boiling in the presence of external magnetic force. *Applied Thermal Engineering*, 139, 598-608.
5. Taheri, M. H., Mohammadpourfard, M., Sadaghiani, A. K., & Kosar, A. (2018). Wettability alterations and magnetic field effects on the nucleation of magnetic nanofluids: A molecular dynamics simulation. *Journal of Molecular Liquids*, 260, 209-220.
6. Ghorbani, M., Sadaghiani, A. K., Villanueva, L. G., & Koşar, A. (2018). Hydrodynamic cavitation in microfluidic devices with roughened surfaces. *Journal of Micromechanics and Microengineering*, 28(7), 075016.
7. Karimzadehkhoei, M., Shojaeian, M., Sadaghiani, A. K., Şendur, K., Mengüç, M. P., & Koşar, A. (2018). Entropy Generation Analysis of Laminar Flows of Water-Based

Nanofluids in Horizontal Minutubes under Constant Heat Flux Conditions. *Entropy*, 20(4), 242.

8. Ghorbani, M., Alcan, G., Sadaghiani, A. K., Mohammadi, A., Unel, M., Gozuacik, D., & Koşar, A. (2018). Characterization and pressure drop correlation for sprays under the effect of micro scale cavitation. *Experimental Thermal and Fluid Science*, 91, 89-102.

9. Sadaghiani, A. K., Saadi, N. S., Parapari, S. S., Karabacak, T., Keskinöz, M., & Koşar, A. (2017). Boiling heat transfer performance enhancement using micro and nano structured surfaces for high heat flux electronics cooling systems. *Applied Thermal Engineering*, 127, 484-498.

10. Motezakker, A. R., Sadaghiani, A. K., Akkoc, Y., Parapari, S. S., Gözüaçık, D., & Koşar, A. (2017). Surface modifications for phase change cooling applications via crenarchaeon *Sulfolobus solfataricus* P2 bio-coatings. *Scientific reports*, 7(1), 17891.

11. Sadaghiani, A. K., Motezakker, A. R., Özpınar, A. V., İnce, G. Ö., & Koşar, A. (2017). Pool boiling heat transfer characteristics of inclined pHEMA-coated surfaces. *Journal of Heat Transfer*, 139(11), 111501.

12. Sadaghiani, A. K., & Koşar, A. (2017). Experimental study on subcooled flow boiling in horizontal microtubes and effect of heated length. *Heat Transfer Engineering*, 38(3), 313-322.

13. Ghorbani, M., Sadaghiani, A. K., Yidiz, M., & Koşar, A. (2017). Experimental and numerical investigations on spray structure under the effect of cavitation phenomenon in a microchannel. *Journal of Mechanical Science and Technology*, 31(1), 235-247.

14. Sadaghiani, A. K., Yildiz, M., & Koşar, A. (2016). Numerical modeling of convective heat transfer of thermally developing nanofluid flows in a horizontal microtube. *International Journal of Thermal Sciences*, 109, 54-69.

15. Şişman, Y., Sadaghiani, A. K., Khedir, K. R., Brozak, M., Karabacak, T., & Koşar, A. (2016). Subcooled flow boiling over microstructured plates in rectangular minichannels. *Nanoscale and Microscale Thermophysical Engineering*, 20(3-4), 173-190.

16. Sadaghiani, A. K., & Koşar, A. (2016). Numerical and experimental investigation on the effects of diameter and length on high mass flux subcooled flow boiling in horizontal microtubes. *International Journal of Heat and Mass Transfer*, 92, 824-837.

A3.2 Conference proceedings and presentations

17. A.K. Sadaghiani, V.O. Kaya, M.I. Sevgen, O. Kutlu, and A. Koşar , "Surface modifications for refrigeration systems via crenarchaeon *Sulfolobus solfataricus* P2 bio-coatings" Gordon Research Conference on Micro and Nanoscale Phase Change Heat Transfer February 03-08, 2019, Lucca (Barga), Italy.
18. Sadaghiani, A.K., Motezakker, A.R., and Koşar, A., " Experimental Studies on Steam Condensation in Horizontal and Vertical Microtubes," 13th International Conference on Heat Transfer, Fluid Mechanics and Thermodynamics, HEFAT2017, Portoroz, Slovenia, July, 2017, 1570-340622.
19. Karimzadehkhoei, M., Sadaghiani, A.K., Sendur, K., Menguc, P., and Kosar, A., "Experimental Study on Heat Transfer of Multi-Walled Carbon Nanotubes/Water Nanofluids in Horizontal Microtubes," Micro/Nanoscale Heat & Mass Transfer International Conference, January, 2016, Biopolis, Singapore, MNHMT2016-6574.
20. Sadaghiani, A.K., Sisman, Y., Ozaydin-Ince, G., and Kosar, A., "An Experimental Study on Flow Boiling Characteristics of pHEMA Coated Surfaces in a Microchannel," Micro/Nanoscale Heat & Mass Transfer International Conference, January, 2016, Biopolis, Singapore, MNHMT2016-6573.
21. Sisman, Y., Sadaghiani, A.K., Khedir, K., Karabacak, T., and Kosar, A., "Nucleate Boiling Heat Transfer Enhancement Using Nanostructured Al-Alloy Plates," Micro/Nanoscale Heat & Mass Transfer International Conference, January, 2016, Biopolis, Singapore, MNHMT2016-6582.
22. Sadaghiani, A. K., Yalçın, S.E., and Koşar, A. "Experimental Studies on Hydro-Thermal Characteristics of High Mass Flux Subcooled Flow Boiling in Horizontal Microtubes", Ninth International Conference on BOILING AND CONDENSATION HEAT TRANSFER Boulder, Colorado, USA, April 26-29, 2015.

A3.3 Patents

1. WO2019004967, "Heat Exchanger with Enhanced Heat Transfer Surfaces", 14 April 2017.

2. PCT/TR 2017/21935, "Heat Exchanging Apparatus and Method", 26 December 2017.